Surface X-ray Diffraction Studies of Graphene on Ruthenium and Hexagonal Boron Nitride on PtRh-Alloy Surfaces

---

Dissertation

zur

Erlangung der naturwissenschaftlichen Doktorwürde

(Dr. sc. nat.)

vorgelegt der

Mathematisch-naturwissenschaftlichen Fakultät

der

Universität Zürich

von

Irakli Kalichava

aus

Georgien

Promotionskomitee

Prof. Dr. Philip R. Willmott (Vorsitz)

Prof. Dr. Jürg Osterwalder (Leitung der Dissertation)

Prof. Dr. Michael Altman

Zürich, 2014

ისევ ძირი ძველი ამის ყენებაში ეძებდნენ

დ. გურამიშვილი

To my family

This document was prepared using LaTeX2$_\varepsilon$ using Philip R. Willmott's customized version of the document class file `book.cls`, named `coolhab.cls`, and a customized bibliography style created using the `custom-bib` package.

Printed in Switzerland

Acknowledgments

This work is the result of a challenging journey, upon which many people have contributed and given their support. I would like to thank the following persons for their support and dedication throughout my entire studies.

First and foremost I would like to thank my thesis advisor Philip Willmott, for hiring me as his PhD student and for having given me the opportunity to perform research at the world-class research facility as excellent as the Paul Scherrer Institut. He guided me in his friendly way through my PhD and has made this work a pleasure.

My biggest thanks to Thomas Greber for his scientific input in this thesis. He was always enthusiastic providing inexhaustible hyperbolic ideas along the interesting discussions on the subject of nanomeshes. I thank his group members, students, Adrian Hemmi, Roland Stania and Carlo Bernard for providing the nanomesh samples and initiating interesting beamtimes. This work would not have been possible without their contribution.

I thank Mike Altman and Jürg Osterwalder for serving on the committee. Their support, feedbacks, comments and guidance were valuable through all these years.

I also thank to Marcella Iannuzzi because important results in this work are based on her DFT calculations. She not only provided the DFT models, but discussions with her were very fruitful and gave me detailed insights.

I wish to thank my group members Steven Leake and Stephan Pauli for helping in understanding the beamline operation, data analysis and structure fitting. Thanks are also due to my colleagues for a pleasant time and creating friendly atmosphere through all these years.

Experiments performed in this work greatly relied on our in-house engineer Dominik Meister and technician Michael Lange. I would like to thank them for their support and the enormous assistance. I would also like to acknowledge the help of Oliver Bunk.

My special thanks go to Hugo Keller and Zurab Guguchia for their friendly advice and moral support during my studies.

And finally, I would like to thank my family and friends for their encouraging words and support that helped me to to pursue these studies.

Abstract

sp^2 single layers of graphene and hexagonal boron nitride (h-BN) on transition metal substrates show many interesting properties not observed in the three-dimensional crystalline form. When these layers are grown on substrates with different lattice parameters, the lattice mismatch induces strain which with the surface-area effect impose the formation of superstructures. In general, the interaction of the sp^2 layer with the metal substrate involves both weak van der Waals forces and strong chemical bonds that can have a considerable effect, depending on the lattice mismatch and the type of metal. In some cases the lattice mismatch strain causes the buckling of the sp^2 layer and results in a periodically varying strength of the interaction with the substrate across the surface. Such structural changes can have a decisive influence on the electronic properties. Depending on the substrates, significant charge transfer and the site-specific orbital hybridization between the metal and the sp^2 layer may occur. These corrugated superstructures are both interesting from a fundamental point of view as well as for their potential in technological applications.

Surface X-ray diffraction (SXRD) offers powerful and non-destructive possibilities for the investigation for two-dimensional systems such as surface structures, interfaces and thin films. It is a straightforward process to determine the reconstruction and the superstructure size with picometer resolution. In SXRD, the full structure studies represent the main challenge, as one is confronted with the phase problem. Different phase-retrieval and structure-refinement approaches allow one to overcome this problem. This thesis describes SXRD structural studies of graphene and h-BN grown on ruthenium, rhodium, and platinum-rhodium alloy.

Graphene on ruthenium forms a corrugated 25-on-23 superstructure which was extensively studied by means of different techniques. In this work, in conjunction with density functional theory calculations (DFT), this system has been further elucidated and important structural parameters have been refined. SXRD simulations based on the present DFT structure were performed and compared to the experimental result. The simulated superstructure rods exhibit

all essential structural characteristics and are fairly consistent with experiment. The model has a goodness of fit better than that of previous models. Furthermore the DFT optmized model was refined using the parameterization procedure and its physical validity was successfully evaluated.

The *h*-BN grown on PtRh 50:50 alloy surface forms a typical commensurate nanomesh structure. In this work, SXRD was applied to this system and an 11-on-10 reconstruction was determined. The recorded crystal truncation rods for the bare PtRh were compared to those from *h*-BN/PtRh. This allowed the elucidation of the influence of the *h*-BN nanomesh on the near-surface structure of PtRh. It was found the *h*-BN nanomesh imposes compositional changes in the PtRh substrate. In addition to qualitative findings, semi-quantitative structure fitting was performed where the Rh-composition profile was obtained for the bare PtRh and *h*-BN/PtRh samples.

h-BN nanomeshes may exhibit modulation of the adsorption potential which allows template functionality to produce well-ordered arrays of various adatoms, molecules and atomic clusters. *h*-BN on Rh forms a well-ordered nanomesh structure and shows a strong modulation of the binding energy. In order to demonstrate a possible template functionality of this system, xenon crystals were grown on *h*-BN/Rh and several in-situ SXRD experiments were performed in the framework of this thesis.

Zusammenfassung

Monoatomar dicke sp^2 Schichten aus Graphen und hexagonalem Bornitrid auf Übergangsmetallsubstraten weisen viele interessante Eigenschaften auf, die nicht in der dreidimensionalen kristallinen Form beobachtet werden können. Wenn diese Schichten auf Substraten mit unterschiedlichen Gitterkonstanten wachsen, bewirkt die Gitterfehlanpassung eine Spannung, die die Bildung von Überstrukturen verursacht. Im Allgemeinen umfasst die Wechselwirkung der sp^2 Schicht mit dem Metallsubstrat sowohl schwache van-der-Waals-Kräfte, als auch starke chemische Bindungen, die eine beträchtliche Wirkung haben können, abhängig von der Gitterfehlanpassung und der Art des Metalls. In einigen Fällen ist die Gitterfehlanpassung, die die Spannung bewirkt, ein Knicken der sp^2-Schicht und führt zu einer periodisch variierenden Stärke der Wechselwirkung mit dem Substrat entlang der Oberfläche. Solche Strukturänderungen können einen entscheidenden Einfluss auf die elektronischen Eigenschaften haben. In Abhängigkeit von den Substraten, kann signifikanter Ladungstransfer und eine lokale Hybridisierung der Orbitale zwischen dem Metall und der sp^2-Schicht auftreten. Diese korrugierten Überstrukturen sind sowohl aus fundamentaler Sicht, als auch für ihr Potenzial in technischen Anwendungen interessant.

Oberflächenrntgenbeugung (SXRD) bietet leistungsstarke und zerstörungsfreie Möglichkeiten für die Untersuchung von zweidimensionalen Systeme wie Oberflächenstrukturen, Grenzflächen und dünnen Schichten. Es ist ein einfacher Prozess, um den Wiederaufbau und den Überbau der Größe auf Pikometer Genauigkeit zu bestimmen. In SXRD, sind die vollen Strukturuntersuchungen die zentrale Herausforderung wegen des Phasenproblems. Verschiedene Phase-Retrieval- und Struktur-Verfeinerungs Ansätze erlauben es, dieses Problem zu überwinden. Diese Arbeit beschreibt SXRD-Strukturuntersuchungen von Graphen und h-BN auf Ruthenium, Rhodium und Platin-Rhodium.

Graphen auf Ruthenium bilden einen korrugierte 25-auf-23 Struktur, die weitgehend durch verschiedene Techniken untersucht worden. In dieser Arbeit wurde dieses System in Verbindung

mit der Dichtefunktionaltheorie-Berechnungen (DFT) weiter aufgeklärt und wichtige Strukturparameter wurden verfeinert. SXRD-Simulationen wurden unter Verwendung der vorliegenden DFT-Struktur durchgeführt und mit experimentellen Ergebnissen verglichen. Die simulierten Überstrukturstangen zeigen alle wesentlichen Strukturmerkmale und sind mit dem Experiment ziemlich konsistent. Das Modell hat eine bessere Güte der Anpassung als die der Vorgängermodelle. Außerdem wurde das DFT-optimierte Modell mit dem Parametrisierungsverfahren verfeinert und seine physikalische Gültigkeit wurde erfolgreich ausgewertet.

Die *h*-BN/PtRh 50:50 Legierungsoberfläche bildet eine typische Nanomesh Struktur. In dieser Arbeit wurde SXRD dem System angelegt und ein 11-on-10-Rekonstruktion bestimmt. Die aufgezeichneten Daten des reinen PtRh wurden mit denen von *h*-BN/PtRh verglichen. Dies ermöglichte die Aufklärung des Einflusses des *h*-BN Nanomesh auf der oberflächennahen Struktur von PtRh. Es wurden im PtRh Substrat vom *h*-BN Nanomesh induzierte kompositorischen Veränderungen festgestellt. Neben qualitativen Ergebnisse wurde semi-quantitatives Struktur Fitting durchgeführt, bei dem die Rh-Zusammensetzung für das reine PtRh und *h*-BN/PtRh Proben Profil erhalten wurde.

h-BN Nanomesh kann durch Modulation des Absorptionspotential als Grundlage dienen, um gut geordneten Arrays von verschiedenen Adatome, Molekülen und Clustern Atom zu produzieren. *h*-BN auf Rh bildet eine gut geordnete Nanomeshstruktur und zeigt eine starke Modulation der Bindungsenergien. Um eine mögliche Vorlage für eine Funktion dieses Systems zu demonstrieren, wurden Xenon-Kristalle auf *h*-BN/Rh gewachsen und im Rahmen dieser Arbeit wurden mehrere in-situ-SXRD-Experimente durchgeführt.

Contents

List of Figures

List of Tables

Chapter 1

Introduction

1.1 Introduction

The physics of single atomic layers yields many interesting phenomena not observed in three-dimensional crystalline materials. Surface-area effects and quantum effects are dominant factors that greatly modify the bulk properties of crystalline matter as the thickness is reduced. When the crystal is grown on a substrate with a different lattice constant, there will be strain at the interface. If we consider a one-atom thick layer, the induced strain may significantly affect the physical properties. The atoms adopt a different structure than that of the bulk. Certain changes in electronic properties may also emerge.

Here, the basic concepts of the single sp^2 layers of graphene and hexagonal boron nitride (h-BN) on transition metal substrates are introduced. The structural details investigated by means of X-ray diffraction are presented later.

Graphene, a 2-dimensional crystalline allotrope of carbon is a very well known and studied material since its discovery in isolated form in 2007 [1]. Graphene is a one-atom thick layer of graphite and the basic structural block of many other carbon allotropes. Graphite consists of graphene sheets arranged in an ABAB sequence that are held by weak van der Waals forces [Figure 1.1 (a)]. In graphene, sp^2-bonded carbon atoms form a hexagonal lattice containing two atoms per unit cell. The hybridization of sp^2 orbitals of two neighbouring carbon atoms develops strong in-plane σ bonds. The latter give rise to occupied σ and empty anti-bonding σ^* bands. The electrons from p_z states of carbon are not involved in bonding within the graphene

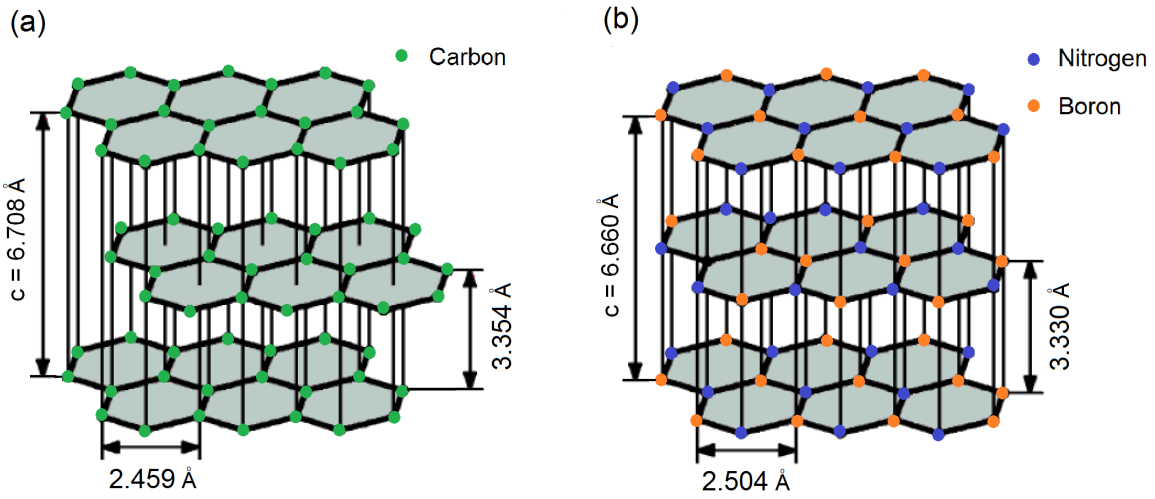

Figure 1.1: The structure of gaphite and bulk hexagonal boron nitride.

plane so they are delocalized and form π and π^* bands. These electrons contribute to the transport properties and therefore determine the Fermi level. Intrinsic graphene is a zero-gap semiconductor, in which the Fermi level can be tuned by doping. Due to its two-dimensional structure, many peculiar properties emerge, not found in conventional three-dimensional materials. The most pronounced feature is the fact that the electrons behave like relativistic massless particles [2, 3].

Single-layer hexagonal boron nitride (h-BN) has a honeycomb structure similar to graphene, but two different atoms, boron and nitrogen, constitute the unit cell. As a consequence of the different basis atoms which determine the band structure, the h-BN is a large-gap insulator. Analogous to graphene, in h-BN, alternate boron and nitrogen atoms are linked via strong covalent sp^2-hybridized orbitals and form a hexagonal structure. If many single h-BN layers are stacked together, the corresponding bulk structure would be known as hexagonal boron nitride, similar to graphite. It is thermally and chemically stable because of the strong B-N bond. However, the weak bonding between layers means that they can easily slide over each other and may provide lubrication applications.

The sp^2 single layers can be synthesized on a transition metal surface via chemical vapour deposition (CVD). At high temperatures, an atomically clean metal substrate surface acts as a catalyst which decomposes the specific precursor molecules from the gas phase [4]. In the

case of the graphene, precursor molecules like hydrocarbons react on the hot metal surface and subsequently hydrogen is released. The remaining dehydrogenated atoms diffuse on the surface and form a regular hexagonal lattice in a self-assembly process after gradual cooling. The surface loses its catalytic activity after one monolayer formation, hence the sticking coefficient of the precursor molecule becomes extremely small. The growth can thus be considered as self-limiting, as in atomic-layer deposition (ALD). This behaviour thus permits the growth of large-area highly crystalline single layers of graphene on various metal substrates [5, 6]. The single layers of *h*-BN on transition metal substrates are synthesized via the same CVD procedure but using the precursor borazine $(HBNH)_3$, or similar chemicals [7, 8].

The sp^2 single layers grown on transition metal substrates exhibit interesting physical properties. The interaction of the sp^2 layer with the metal surface involves not only weak van der Waals forces, but also strong chemical interactions that can have a considerable structural effect on both the sp^2 layer and the underlying substrate. Depending on the lattice mismatch between the sp^2 layer and the metal substrate, the sp^2 adlayer can be slightly strained while the original flat structure is maintained. On the other hand, if the lattice mismatch exceeds a certain critical value, the sp^2 adlayer atoms rearrange and adopt a new ordering, referred as a *surface reconstruction*. The lattice mismatch is given by

$$M = \frac{2\,(a_{ov} - a_{sub})}{(a_{ov} + a_{sub})}, \tag{1.1}$$

where a_{ov} is the in-plane lattice constant of the sp^2 overlayer and a_{sub} is the in-plane lattice constant of the substrate. The sign of M indicates whether the mismatch induces a compressive (+) or tensile (-) stress in the overlayer.

In some cases the lattice mismatch strain causes the overlayer to be buckled. In this case the interaction between the sp^2 layer and the metal is found to be strongly inhomogenous and modulated with the same periodicity as the resulting *superstructure*.

The bond energy between the atoms of the sp^2 layers and a metal surface gives rise to a *lock-in energy*, the energy that has to be paid when the overlayer is moved laterally across the substrate surface. The lock-in energy gain compared to the average adhesion energy determines whether the overlayer is corrugated (i.e. buckled) or flat (Figure 1.2). If the system has no lock-in energy then the resulting structure is an incommensurate flat structure, referred as moiré [9]. From the geometrical perspective, a moiré pattern represents a periodic pattern where one lattice is superposed on another with a different periodicity [Figure 1.2(c)]. It is important

to note that it is difficult to distinguish using scanning tunneling microscopy (STM) between a flat moiré and a corrugated superstructure, because it is difficult to differentiate between changes in local electron density and vertical shifts in atomic positions. Diffraction techniques such as low-energy electron diffraction (LEED) and surface X-ray diffraction (SXRD) help to resolve this problem.

Graphene on Ir(111) is a weakly interacting system where the graphene band gap is slightly opened by 0.2 eV [10]. The graphene layer is slightly compressed and forms an incommensurate (9.32×9.32) moiré pattern [11]. In the case of graphene on Ru(0001), the interaction is strong, due to significant hybridization of the p-orbitals of graphene with the d orbital of Rh(0001). The graphene forms a corrugated commensurate superstructure and the reconstruction is found to be 25-on-23 [12]. This system is the focus of Chapter 3.

In h-BN on Ni(111) the lattice mismatch is only 0.4 %. Such a small mismatch causes weak lateral compression and leads to (1×1) unit cells and atomically flat layers [13–15]. On the other hand the h-BN on Rh(111) forms a corrugated superstructure called as a *nanomesh* [7]. In this structure, (13×13) h-BN unit cells match (12×12) Rh units, leading to a compressive stress and a lattice mismatch of 0.86 % [16]. The h-BN-substrate registry has two distinct regions: *wires* and *pores*. The pores are strongly bound regions to the underlaying substrate, while the wires are weakly bound. From X-ray photoelectron spectroscopy studies it was found that these two regions possess distinct electronic structures, demonstrated by σ band splitting of BN.

The h-BN nanomesh grown on $Pt_{50}Rh_{50}(111)$ has shown intriguing features. Apart from the typical nanomesh structure, interestingly, it was found that h-BN induces lateral segregation on the topmost PtRh atomic layer whereby Rh atoms gather under the pores [17]. The results of an SXRD study on this system will be the subject of discussion in Chapter 4.

The graphene and h-BN superstructures assembled on certain substrates may exhibit strong modulation of the adsorption potential landscape across the surface. In this context, they are capable to accommodate various adatoms, molecules and nano-clusters on their surfaces, therefore providing the template functionality for a surface-supported bottom up approach. Nanotemplates based on h-BN nanomeshes have been intensively investigated in recent years [18, 19]. A model example is h-BN on Rh(111), where a significant adsorption potential gradient across the pore region was found [20]. This leads to site-specific binding energy and hence exploits trapping capabilities for different adatoms. STM studies performed on Xe-adatom des-

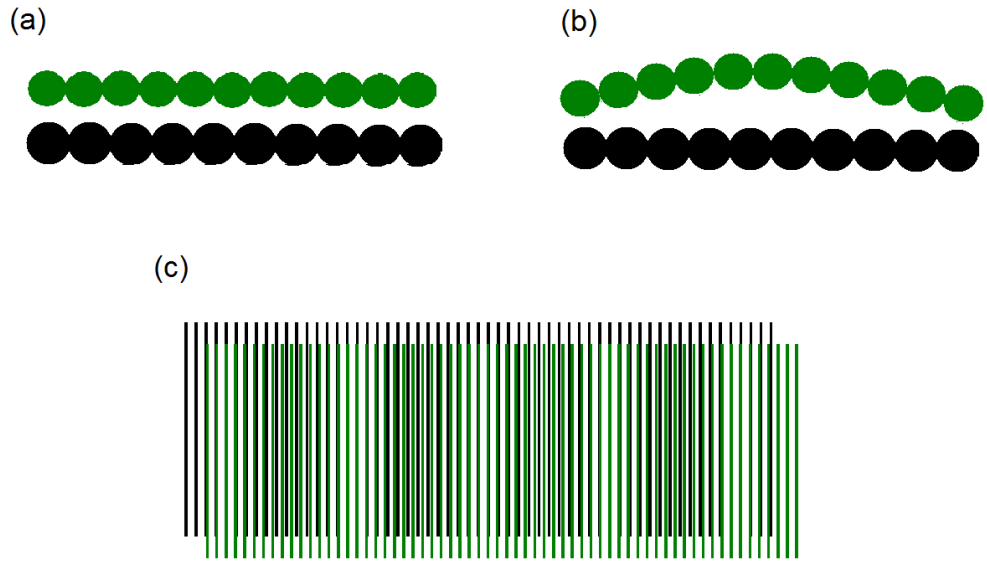

Figure 1.2: Schematic ilustration of a flat moiré (a) and a buckled (b) structure on the substrate. (c) The superposition of two regular patterns produces a moiré pattern.

orption from *h*-BN/Rh(111) have shown the Xe atoms cluster around the rim of the nanomesh, where the absorption potential is at a minimum [21].

Bibliography

[1] A. K. Geim and K. S. Novoselov: "The rise of graphene." *Nature materials* **6**(3), 183–191 (2007).

[2] A. C. Neto, F. Guinea, N. Peres, K. S. Novoselov, and A. K. Geim: "The electronic properties of graphene." *Reviews of modern physics* **81**(1), 109 (2009).

[3] K. S. Novoselov, Z. Jiang, Y. Zhang, S. V. Morozov, H. L. Stormer, U. Zeitler, J. C. Maan, G. S. Boebinger, P. Kim, and A. K. Geim: "Room-temperature quantum Hall effect in graphene." *Science* **315**(5817), 1379–1379 (2007).

[4] J. H. Park and T. Sudarshan: *Chemical vapor deposition*, volume 2. ASM International (2001).

[5] A. Reina, X. Jia, J. Ho, D. Nezich, H. Son, V. Bulovic, M. S. Dresselhaus, and J. Kong: "Large area, few-layer graphene films on arbitrary substrates by chemical vapor deposition." *Nano letters* **9**(1), 30–35 (2008).

[6] A. N. Obraztsov: "Chemical vapour deposition: making graphene on a large scale." *Nature nanotechnology* **4**(4), 212–213 (2009).

[7] M. Corso, W. Auwärter, M. Muntwiler, A. Tamai, T. Greber, and J. Osterwalder: "Boron nitride nanomesh." *Science* **303**(5655), 217–220 (2004).

[8] A. Goriachko, Y. He, M. Knapp, H. Over, M. Corso, T. Brugger, S. Berner, J. Osterwalder, and T. Greber: "Self-assembly of a hexagonal boron nitride nanomesh on Ru (0001)." *Langmuir* **23**(6), 2928–2931 (2007).

[9] K. Hermann: "Periodic overlayers and moiré patterns: theoretical studies of geometric properties." *Journal of Physics: Condensed Matter* **24**(31), 314210 (2012).

[10] I. Pletikosic, M. Kralj, P. Pervan, R. Brako, J. Coraux, A. N'diaye, C. Busse, and T. Michely: "Dirac cones and minigaps for graphene on Ir (111)." *arXiv preprint arXiv:0807.2770* (2008).

[11] J. Coraux, T. N. Plasa, C. Busse, T. Michely, *et al.*: "Structure of epitaxial graphene on Ir (111)." *New Journal of Physics* **10**(4), 043033 (2008).

[12] D. Martoccia, P. R. Willmott, T. Brugger, M. Björck, S. Günther, C. M. Schlepütz, A. Cervellino, S. A. Pauli, B. D. Patterson, S. Marchini, *et al.*: "Graphene on Ru (0001): a 25×25 supercell." *Physical review letters* **101**(12), 126102 (2008).

[13] M. N. Huda and L. Kleinman: "h-BN monolayer adsorption on the Ni (111) surface: A density functional study." *Physical Review B* **74**(7), 075418 (2006).

[14] W. Auwärter, T. Kreutz, T. Greber, and J. Osterwalder: "XPD and STM investigation of hexagonal boron nitride on Ni (111)." *Surface science* **429**(1), 229–236 (1999).

[15] T. Greber: "Graphene and boron nitride single layers." *arXiv preprint arXiv:0904.1520* (2009).

[16] O. Bunk, M. Corso, D. Martoccia, R. Herger, P. R. Willmott, B. D. Patterson, J. Osterwalder, J. F. van der Veen, and T. Greber: "Surface X-ray diffraction study of boron-nitride nanomesh in air." *Surface science* **601**(2), L7–L10 (2007).

[17] R. Stania: *Lateral Segregation in h-BN/PtRh(111)*. Master's thesis, Universität Zürich, Zurich (2012).

[18] S. Berner, M. Corso, R. Widmer, O. Groening, R. Laskowski, P. Blaha, K. Schwarz, A. Goriachko, H. Over, S. Gsell, *et al.*: "Boron nitride nanomesh: Functionality from a corrugated monolayer." *Angewandte Chemie international edition* **46**(27), 5115–5119 (2007).

[19] A. Goriachko, A. A. Zakharov, and H. Over: "Oxygen-etching of h-BN/Ru (0001) nanomesh on the nano-and mesoscopic scale." *The Journal of Physical Chemistry C* **112**(28), 10423–10427 (2008).

[20] H. Dil, J. Lobo-Checa, R. Laskowski, P. Blaha, S. Berner, J. Osterwalder, and T. Greber: "Surface trapping of atoms and molecules with dipole rings." *Science* **319**(5871), 1824–1826 (2008).

[21] R. Widmer, D. Passerone, T. Mattle, H. Sachdev, and O. Gröning: "Probing the selectivity of a nanostructured surface by xenon adsorption." *Nanoscale* **2**(4), 502–508 (2010).

Chapter 2

Surface X-ray diffraction

2.1 Introduction

X-radiation is a form of electromagnetic radiation with a wavelength in the range of 0.1 Å to 100 Å. X-radiation was accidentally discovered by the German physicist Wilhelm Röntgen in 1896. When he was working with a cathode-ray tube, he realised that new "unknown light" was being emitted from his device. The most intriguing feature of this radiation was its capability of passing through solid objects and leaving their shadows on a photographic film. Later he demonstrated that these "unknown" rays could be used to image internal components of the human body. He produced an image of his wife's hand with a ring on her finger. Since this mysterious "unknown" radiation was not observed before, he named it "X-rays". Within a few decades, X-ray technology quickly developed and emerged in many fields ranging from medical application to materials research.

After the discovery of X-rays, von Laue with his two technicians, Walter Friedrich and Paul Knipping, successfully demonstrated diffraction of X-rays by crystals for the first time. In this experiment, X-ray diffraction pattern of a copper sulphite crystal was recorded. A photographic plate showed bright spots arranged in a pattern of intersecting circles [1, 2]. Furthermore, he developed a law that describes conditions for incident waves to be diffracted by a crystal lattice. He was awarded the Nobel Prize in Physics in 1914 for his discovery of the diffraction of X-rays by crystals.

William Lawrence Bragg and his father William Henry Bragg made significant contribu-

tions in X-ray crystallography. Implementing and analysing Laue diagrams, they determined the crystal structure of table salt and diamond [3–7]. Here they also provided the famous Bragg's law, the reduced mathematical form of the Laue diffraction conditions. They shared the 1915 Nobel Prize in Physics. After the pioneering work of Von Laue's and Bragg's, X-ray diffraction developed rapidly and became one of the most notable analytical techniques for materials investigation and characterisation. Application areas include condensed matter, nano-structured materials, biological systems and soft matter.

In addition to single-crystal and powder diffraction, X-ray diffraction has become a valuable tool for studying surfaces [8, 9]. In laboratory-based X-ray machines, the obtained diffraction signal from a volume of 2-dimensional region of a sample surface which is probed by incoming X-ray beam is very weak. This limitation is mainly due to the lack of enough flux on the sample. Thanks to dedicated synchrotron storage rings providing well-collimated, tunable, high-flux X-radiation, investigation of various surfaces became viable. Surface X-ray diffraction (SXRD) has been developed as one of the most powerful and non-destructive techniques solving surface structures, studying thin films and interfaces. Application of SXRD was first time demonstrated on the GaAs-Al interface [10] and the Ge(001) reconstructed surface [11].

In this chapter, an introduction to the theory of X-ray diffraction will be given. First, a brief description of X-ray scattering on atoms will be provided, then bulk diffraction will be discussed covering Bragg's law and the Laue conditions. Essential concepts of surface diffraction will be introduced and explained as well. More practical aspects of SXRD measurement, data treatment and analysis will be covered in the final sections.

2.2 Basic theory

2.2.1 Crystal lattice and reciprocal lattice

A crystal lattice is a laterally periodic and regular arrangement of atoms in three-dimensions. The geometry and the translational symmetry of the repeat units is classified by the so-called *Bravais lattice*. The Bravais lattice is generated by the three unit vectors $\mathbf{a}$, $\mathbf{b}$, and $\mathbf{c}$ so that each lattice point is defined by a vector $\mathbf{R}$

$$\mathbf{R} = n_1\mathbf{a} + n_2\mathbf{b} + n_3\mathbf{c}, \tag{2.1}$$

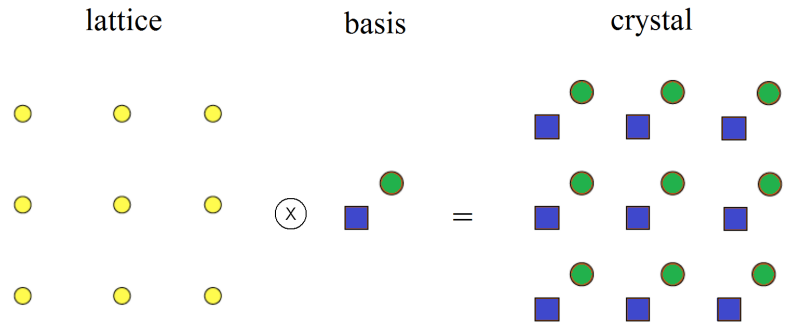

Figure 2.1: A two-dimensional crystal lattice consisting of basis atoms attached at each Bravais lattice point.

where n_1, n_2 and n_3 are integers.

The crystal structure is made up of the group of atoms, the basis, positioned at each and every Bravais lattice point (see Figure 2.1). The lattice parameter vectors **a**, **b** and **c** enclose a volume which encapsulates the basis.

To describe diffraction from crystals it is helpful to introduce the concept of the *reciprocal lattice*. Similar to the Bravais lattice, any site in reciprocal lattice is given by:

$$\mathbf{G_{hkl}} = h\mathbf{a}^* + k\mathbf{b}^* + l\mathbf{c}^*, \tag{2.2}$$

here h,k, and l are integers, known as the *Miller indices*. The reciprocal-space base vectors $\mathbf{a}^*$, $\mathbf{b}^*$ and $\mathbf{c}^*$ are related to the real lattice via the following expressions:

$$\mathbf{a}^* = 2\pi \frac{\mathbf{b} \times \mathbf{c}}{\mathbf{a} \cdot (\mathbf{b} \times \mathbf{c})}, \tag{2.3}$$

$$\mathbf{b}^* = 2\pi \frac{\mathbf{c} \times \mathbf{a}}{\mathbf{b} \cdot (\mathbf{c} \times \mathbf{a})},$$

$$\mathbf{c}^* = 2\pi \frac{\mathbf{a} \times \mathbf{b}}{\mathbf{c} \cdot (\mathbf{a} \times \mathbf{b})}.$$

The vector of the reciprocal lattice $\mathbf{G_{hkl}}$ can be related to a particular crystal plane (hkl) of the crystal lattice:

$$G_{hkl} = \frac{2\pi}{d_{hkl}}, \tag{2.4}$$

where d_{hkl} is the interplanar distance of the (hkl)-planes. Note that the vector $\mathbf{G_{hkl}}$ is normal

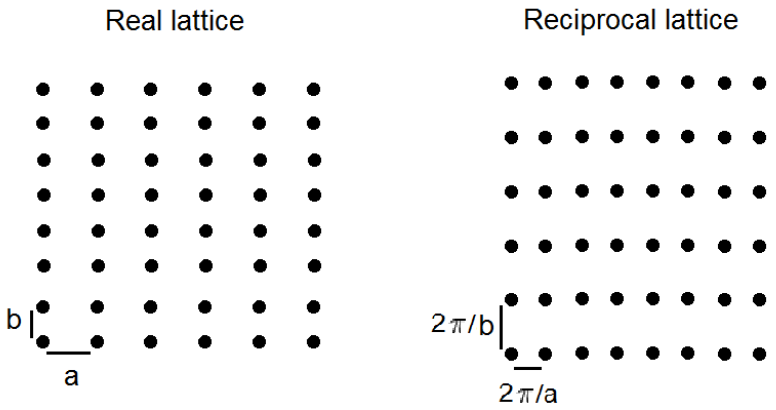

Figure 2.2: The real (left) and the reciprocal (right) lattice for a two-dimensional crystal.

to the (hkl) plane and it introduces the concept that diffraction from a set of planes can be described in terms of a diffraction vector in reciprocal space. The Fourier transform of the real lattice is the reciprocal lattice (Figure 2.2).

2.2.2 Convolution theorem

As we have already said, the crystal structure consists of a basis attached to each lattice point. Mathematically, it can be described as a *convolution* of the Bravais lattice by the basis. The convolution is a mathematical operation, the integral over all space of one function $f(x)$ times another function at $g(u-x)$ where integration is taken over the variable x

$$C(u) = \int f(x)g(u-x)dx = f(x) \otimes g(x). \tag{2.5}$$

The convolution operation is commutative so it does not matter which function is taken first.

The *convolution theorem* states that the Fourier-transform of the product of two functions, $f(x)$ and $g(x)$, is equal to the convolution of the Fourier transform of function $f(x)$ with the Fourier transform of function $g(x)$, that is

$$FT\big[f(x) \cdot g(x)\big] = FT\big[f(x)\big] \otimes FT\big[g(x)\big]. \tag{2.6}$$

This also works the other way round:

$$FT\big[f(x) \otimes g(x)\big] = FT\big[f(x)\big] \cdot FT\big[g(x)\big]. \tag{2.7}$$

2.2.3 The interaction of X-rays with matter

The interaction of X-rays with matter consists of three main phenomena (see Figure 2.3): photoabsorption, Compton scattering, and Thomson scattering. The cross-section and the strength of these effects depend on the energy of the incoming X-ray beam and the elemental composition of the material. In the soft X-ray regime below 5 keV, photoabsorption is the dominant interaction where an absorbed photon transfers all its energy to the bound electron of an atom, thereby ionising it and a photoelectron is produced. At very high energies, Compton effect, an inelastic process, is predominant. Unlike photoabsorption, only part of the energy and momentum of the photon is transferred to an electron. This results a recoiled (scattered) photon with an increased wavelength. Thomson scattering is an elastic-scattering process, where the photon wavelength remains the same after scattering.

2.2.4 Principles of elastic X-ray scattering

The simplest example of Thomson scattering is electromagnetic wave scattering by a free electron. In this process, an oscillating electric component of an incoming radiation acts on an electron and forces it to oscillate with the same frequency. As a result, the oscillating electron re-radiates the electromagnetic wave, and is called *dipole* radiation. The strength of dipole radiation is not isotropic in space, it has its maximum in a direction perpendicular to the electron oscillation axis [Figure 2.4(b)].

The strength of the scattering process is mathematically described by the so-called scattering cross section σ. For Thomson scattering this is given by

$$\sigma_T \;=\; \frac{8\pi}{3} \cdot \left[\frac{1}{4\pi\epsilon_0}\frac{q^2}{mc^2}\right]^2, \tag{2.8}$$

where m and q are the mass and charge of a particle [12]. From Equation 2.8, it is evident that the scattering strength is proportional to the fourth power of the charge and inversely proportional to the square of the mass. Since nucleons are 2000 times heavier then electrons, their scattering strength is negligible. Therefore one may approximate that scattering by an

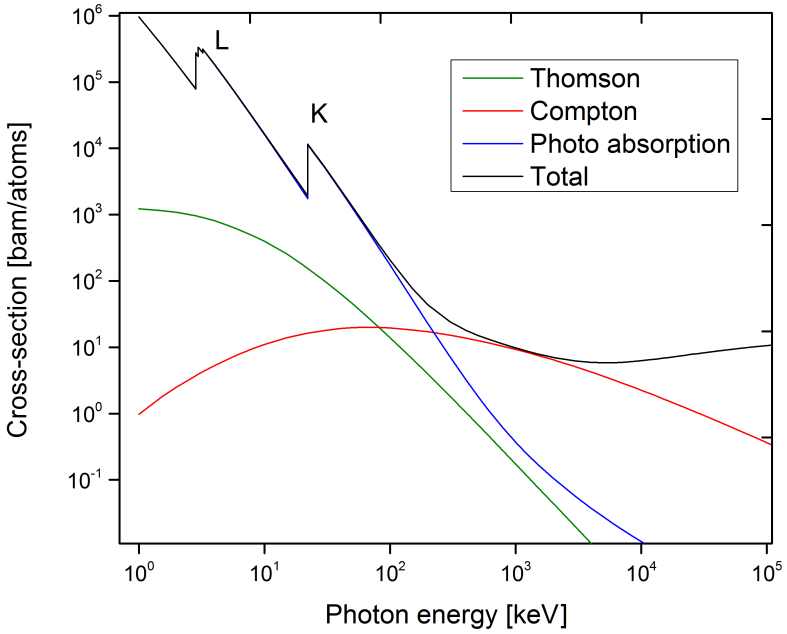

Figure 2.3: The cross-sections for various processes involved in the interaction between X-rays and matter is shown for the example of Ru. Thomson scattering and photoabsorption are dominant processes in the lower energy-range. The $K-$ and $L-$edges of Ru are visible.

atom is due only to its electrons.

In fact, electromagnetic radiation interaction with matter is very complex. All the involved processes are interrelated and can be described by *Fermi's golden rule* which is based on quantum-mechanical principles. For the further description of the elastic X-ray scattering (i.e, Thomson scattering), the classical electrodynamics picture is fairly acceptable. Thomson scattering can be generalised for atoms consisting of many electrons and extended to an arbitrary electron-density distribution such as the basis of a crystalline structure.

In classical optics, the scattering and interference of X-rays propagating through a medium can be described by the Huygens-Fresnel principle. When the X-rays traverse matter, the electrons within the medium re-emit X-rays and act as a source of secondary waves. The resulting amplitude distribution can be calculated as the interference pattern of all those secondary waves. Diffraction can be quantitatively described by so-called *kinematical approximation*

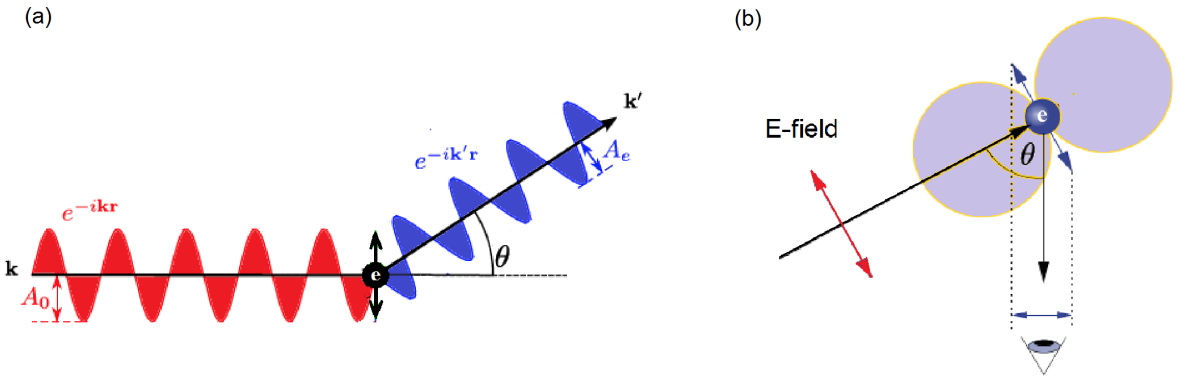

Figure 2.4: Illustration of Thomson scattering: (a) The incident electromagnetic wave with the amplitude A_0 scatters on a free electron. The scattered wave has an amplitude A_e which is proportional to the amplitude of the incident wave A_0 projected into the direction of $\mathbf{k}'$. (b) The angular distribution of the emitted dipole radiation.

which assumes that multiple-scattering effects are too small and that the loss of intensity by scattering is therefore negligible.

2.2.5 X-ray scattering by atoms

When an X-ray beam encounters an atom, the scattered-wave amplitude is simply the vectorial sum of the waves scattered by its electron cloud. Therefore the resulting scattered amplitude depends on the relative phase of the individual scattered waves. If the scattering is in the forward direction ($\theta = 0$), the scattered waves are all in phase and the scattering amplitude is Z times that scattered from a single electron. On the other hand, at some angle θ, the total scattering amplitude will be less than Z due to partial interference. In fact the atom does not act as a point charge because the electrons are physically distributed around the nucleus, described by a charge-density function.

In order to determine the total scattering intensity of an atom, first let us consider an X-ray beam scattered by a free electron in more detail. An incoming plane wave $A_0 \cdot e^{-i\mathbf{kr}}$ with an amplitude A_0 which propagates along the wave vector $\mathbf{k}$ is scattered by an electron located at

position $\mathbf{r}$. The mathematical description for Thomson scattering is given by [12]

$$A_e \cdot e^{-i\mathbf{k}'\mathbf{r}} = A_0 \cdot e^{-i\mathbf{k}\mathbf{r}} \cdot \frac{1}{4\pi\epsilon_0}\frac{e^2}{mc^2} \cdot \frac{1}{R} \cdot p, \tag{2.9}$$

where A_e and $\mathbf{k}'$ is the amplitude and the wavevector of the scattered wave observed at a distance R, and p is a polarisation factor [12]. Equation 2.9 can be rewritten in compact form and further can be solved for A_e:

$$A_e = A_0 \cdot \frac{r_e}{R} \cdot p \cdot e^{-i\mathbf{k}\mathbf{r}} \cdot e^{i\mathbf{k}'\mathbf{r}} = A_0 \cdot \frac{r_e}{R} \cdot p \cdot e^{i(\mathbf{k}'-\mathbf{k})\mathbf{r}} \tag{2.10}$$

$$= A_0 \cdot \frac{r_e}{R} \cdot p \cdot e^{i\mathbf{q}\mathbf{r}}, \tag{2.11}$$

where $\frac{1}{4\pi\epsilon_0}\frac{e^2}{mc^2} = r_e$ is the so-called *Thomson scattering length*. Here we introduce the scattering vector $\mathbf{q} \equiv \mathbf{k}' - \mathbf{k}$ with a magnitude

$$q = \frac{4\pi}{\lambda}\sin\theta, \tag{2.12}$$

where θ is the angle between the $\mathbf{k}$ and $\mathbf{k}'$ vectors.

If we now consider N point charges distributed at positions r_j, then the total scattering amplitude is the coherent sum of all scattered waves (for $R \gg r_i$):

$$A_{\text{tot}} = A_0 \cdot \frac{r_e}{R} \cdot p \cdot \sum_{j=1}^{N} e^{i\mathbf{q}(\mathbf{r}+\mathbf{r}_j)} = A_0 \cdot \frac{r_e}{R} \cdot p \cdot e^{i\mathbf{q}\mathbf{r}} \cdot \sum_{j=1}^{N} e^{i\mathbf{q}\mathbf{r}_j}. \tag{2.13}$$

The electrons in an atom are localized around the nucleus and form a continuous charge distribution with the charge density function $\rho(\mathbf{r}')$. The distribution is assumed to be spherically symmetric, and thus the discrete sum is replaced by an integral over the volume of the atom

$$A_a = A_0 \cdot \frac{r_e}{R} \cdot p \cdot \int_{\text{atom}} e^{i\mathbf{q}(\mathbf{r}+\mathbf{r}')} \cdot \rho_a(\mathbf{r}')\, d^3\mathbf{r}' = A_0 \cdot \frac{r_e}{R} \cdot p \cdot e^{i\mathbf{q}\mathbf{r}} \cdot \underbrace{\int_{\text{atom}} e^{i\mathbf{q}\mathbf{r}'} \cdot \rho_a(\mathbf{r}')\, d^3\mathbf{r}'}_{\equiv f_a(\mathbf{q})}$$

$$= A_0 \cdot \frac{r_e}{R} \cdot p \cdot e^{i\mathbf{q}\mathbf{r}} \cdot f_a(\mathbf{q}), \tag{2.14}$$

The quantity $f_a(\mathbf{q})$ is called the *atomic form factor*. It measures the "strength" of scattered wave amplitude with respect to that from a single electron. As seen from this expression, its value is equal to the Fourier transform of the total electron density $\rho(\mathbf{r}')$. In the case of scattering in the forward direction ($2\theta = 0$), $f_a(\mathbf{q} = 0) = Z$ where Z is the total number of electrons. In any other direction, the scattered waves are partially out of phase and $f_a(\mathbf{q})$ is reduced accordingly.

It is important to note that the atomic form factor is a complex quantity. It has additional terms for the energy related dispersion and absorption corrections. When the photon energy is far away from the absorption edges of the atom, these terms can be neglected. Calculated values of $f_a(\mathbf{q})$ for various atoms and various values of $\sin\theta/\lambda$ can be found in the *International Tables of Crystallography* [13].

2.3 Bulk diffraction

2.3.1 Scattering from an ideal crystal

In a crystalline solid, the constituent atoms are arranged in a regular periodic manner. The scattered X-rays interfere with each other and produce a diffraction pattern. In order to calculate the scattering amplitude from the basis within a unit cell the scattered amplitudes of all the atoms within the unit cell must be vectorially added. The total scattered amplitude is thus the discrete sum over all N atoms and it is calculated by

$$\begin{aligned} A_{uc} &= A_0 \cdot \frac{r_e}{R} \cdot p \cdot \sum_{j=1}^{N} f_j(\mathbf{q}) \cdot e^{i\mathbf{q}(\mathbf{r}+\mathbf{r}_j)} = A_0 \cdot \frac{r_e}{R} \cdot p \cdot e^{i\mathbf{qr}} \cdot \underbrace{\sum_{j=1}^{N} f_j(\mathbf{q}) \cdot e^{i\mathbf{q}\cdot\mathbf{r}_j}}_{\equiv F(\mathbf{q})} \\ &= A_0 \cdot \frac{r_e}{R} \cdot p \cdot e^{i\mathbf{qr}} \cdot F(\mathbf{q}), \end{aligned} \tag{2.15}$$

where $F(\mathbf{q})$ is the so-called *structure factor*. It contains all the information about the arrangement of atoms and their atomic form factors within the unit cell.

Consider an ideal bulk crystal consisting of N_1, N_2, and N_3 unit cells in the three directions of the unit vectors. The scattering amplitude for the entire crystal will be

$$\begin{aligned} A_c &= A_0 \cdot \frac{r_e}{R} \cdot p \cdot e^{i\mathbf{qr}} \cdot F(\mathbf{q}) \cdot \underbrace{\sum_{j_1=0}^{N_1-1} \sum_{j_2=0}^{N_2-1} \sum_{j_3=0}^{N_3-1} e^{i\mathbf{q}\cdot(j_1\mathbf{a}+j_2\mathbf{b}+j_3\mathbf{c})}}_{\text{lattice sum}} \\ &= A_0 \cdot \frac{r_e}{R} \cdot p \cdot e^{i\mathbf{qr}} \cdot F(\mathbf{q}) \cdot \sum_{j_1=0}^{N_1-1} e^{i\mathbf{q}\cdot(j_1\cdot\mathbf{a})} \cdot \sum_{j_2=0}^{N_2-1} e^{i\mathbf{q}\cdot(j_2\cdot\mathbf{b})} \cdot \sum_{j_3=0}^{N_3-1} e^{i\mathbf{q}\cdot(j_3\cdot\mathbf{c})}. \end{aligned} \tag{2.16}$$

The first term $F(\mathbf{q})$ is the unit-cell structure factor (see Equation 2.15). The second term is

the *lattice sum*. Each of the sums over j_i can be expressed as geometrical series:

$$\sum_{j_1=0}^{N_1-1} e^{i\mathbf{q}\cdot(j_1\cdot\mathbf{a})} = \frac{\sin(\frac{1}{2}N_1 q_x a)}{\sin(\frac{1}{2}q_x a)} \cdot e^{iq_x a\cdot(N_1-1)/2}, \tag{2.17}$$

$$\sum_{j_2=0}^{N_2-1} e^{i\mathbf{q}\cdot(j_2\cdot\mathbf{b})} = \frac{\sin(\frac{1}{2}N_2 q_y b)}{\sin(\frac{1}{2}q_y b)} \cdot e^{iq_x a\cdot(N_2-1)/2},$$

$$\sum_{j_3=0}^{N_3-1} e^{i\mathbf{q}\cdot(j_3\cdot\mathbf{c})} = \frac{\sin(\frac{1}{2}N_3 q_z c)}{\sin(\frac{1}{2}q_z c)} \cdot e^{iq_x a\cdot(N_3-1)/2}.$$

By substituting the above equations into Equation 2.16 we obtain

$$\begin{aligned} A_c &= A_0 \cdot \frac{r_e}{R} \cdot p \cdot F(\mathbf{q}) \cdot e^{i\mathbf{qr}} \cdot \frac{\sin(\frac{1}{2}N_1 q_x a)}{\sin(\frac{1}{2}q_x a)} \cdot e^{iq_x a\cdot(N_1-1)/2} \cdot \\ &\quad \frac{\sin(\frac{1}{2}N_2 q_y b)}{\sin(\frac{1}{2}q_y b)} \cdot e^{iq_y b\cdot(N_2-1)/2} \cdot \frac{\sin(\frac{1}{2}N_3 q_z c)}{\sin(\frac{1}{2}q_z c)} \cdot e^{iq_z c\cdot(N_3-1)/2}. \end{aligned} \tag{2.18}$$

In this derivation it was assumed that in the ideal crystal, the atoms are strictly static. In a real situation atoms within the unit cell undergo thermal motions and vibrate around their equilibrium positions, causing the scattered X-ray waves to be attenuated. The parameter which describes this thermal effect is called the *Debye-Waller factor* (DWF). It depends on the scattering vector $\mathbf{q}$. Mathematically DWF is expressed as

$$\text{DWF} = \langle \exp(i\mathbf{q}\cdot\mathbf{u}) \rangle^2$$

where $\mathbf{u}$ is the displacement of a scattering center. If we assume that $\mathbf{u}$ is isotropic then we obtain

$$\text{DWF} = \exp\left(-q^2\langle u^2\rangle/3\right),$$

whereby here q, u are the absolute values, not the vector quantities. $\langle u^2\rangle$ is the mean squared displacement.

2.3.2 Scattering intensity

The scattering amplitude is a complex number which has both magnitude and phase. In experiments, only the intensity is measured, which is proportional to the squared modulus of the amplitude. This situation leads to the so-called *phase problem*, which will be discussed in

the next section. For the measurable intensity we obtain

$$I_c(\mathbf{q}) \quad = |A(\mathbf{q})|^2 = \quad I_0 \cdot \frac{r_e^2}{R^2} \cdot p^2 \cdot |F(\mathbf{q})|^2 \cdot \frac{\sin^2(\frac{1}{2}N_1 q_x a)}{\sin^2(\frac{1}{2}q_x a)} \cdot \frac{\sin^2(\frac{1}{2}N_2 q_y b)}{\sin^2(\frac{1}{2}q_y b)} \cdot \frac{\sin^2(\frac{1}{2}N_3 q_z c)}{\sin^2(\frac{1}{2}q_z c)},$$

where $I_0 = A_0^2$ is the intensity of the incoming wave.

It is important to mention that all these derivations are based on kinematical diffraction theory, in which it is assumed that the X-ray beams are elastically scattered only once and the intensity remains the same for all successive atomic planes. These assumptions significantly simplify quantitative analysis of diffraction data and the determination of atomic structures. On the other hand, the low-energy electron diffraction (LEED) technique requires the application of *dynamical diffraction theory*. The incoming electron beam strongly interacts with the sample and therefore multiple scattering occurs. Hence to calculate or analyze the spot-intensities more complex calculations are required [14].

2.3.3 Laue conditions

Diffraction maxima from crystalline material occur for certain values of $\mathbf{q}$. It can be seen from Equation 2.18 that the product of sine-squared terms have peak whenever the following conditions are simultaneously fulfilled:

$$\frac{1}{2}q_x a = \pi h, \qquad \frac{1}{2}q_y b = \pi k, \qquad \frac{1}{2}q_z c = \pi l, \tag{2.19}$$

where h, k and l are integers. The scattered wave has diffraction maxima when the scattering vector $\mathbf{q}$ is equal to a reciprocal lattice vector $\mathbf{G} = h\mathbf{a}^* + k\mathbf{b}^* + l\mathbf{c}^*$. These are the three *Laue conditions* for the incident X-ray waves to be diffracted by a 3-dimensional crystalline solid. The diffraction pattern represents the reciprocal lattice points (hkl) and constitute an array of δ-functions for N_1, N_2, $N_3 \to \infty$. The relative intensity of the $I(hkl)$ spots depends on the atomic form factors and positions of atoms making up the unit cell.

The Laue conditions can be understood in terms of a simple geometric construction in reciprocal space called the *Ewald Sphere* [15]. Consider an incoming wave with wavevector $|\mathbf{k_{in}}| = \frac{2\pi}{\lambda}$. Since the scattering is elastic, the diffracted wave with wavevector $\mathbf{k_{out}}$ must sit on the surface of a sphere of radius $\frac{2\pi}{\lambda}$. This is the Ewald sphere. We already know that diffraction occurs when the condition $\mathbf{k_f} - \mathbf{k_i} = \mathbf{G}$ is fulfilled. Therefore from the construction we can conclude that the particular (hkl) reflection will be observed whenever it lies on the surface of the Ewald sphere (Figure 2.5).

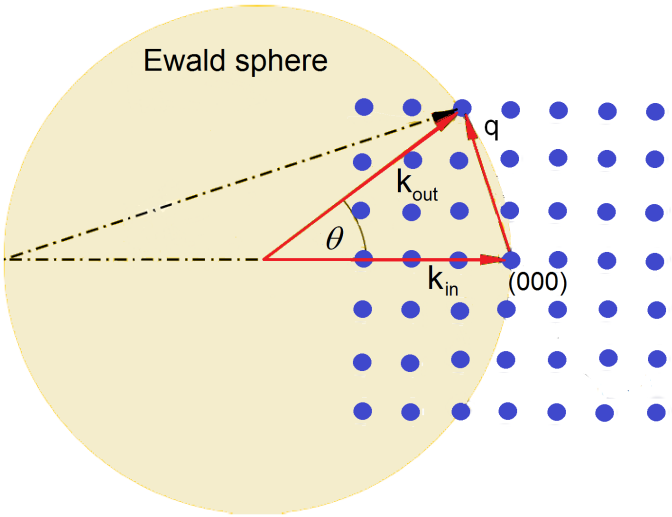

Figure 2.5: The Ewald sphere.

2.3.4 Bragg's law

The famous Bragg's law is the simple description of the diffraction condition and represents a reduced mathematical form of the Laue conditions. When the X-ray beam impinges on a crystal, it experiences successive reflections by the crystallographic planes separated by the interplanar distance d_{hkl} (see Figure 2.6). Constructive interference occurs when the optical path difference between scattered waves from successive atomic planes is an integer number of wavelengths. From the geometrical illustration the path difference is $2d\sin\theta$, where θ is the incidence angle. Hence Bragg's law is written as

$$n\lambda = 2d\sin\theta \tag{2.20}$$

Bragg's equation thus determines the d-spacing between the lattice planes that produce the Bragg peaks. Since there are different (hkl) planes in the crystal, each of them will produce diffraction peaks at the corresponding angle and the d_{hkl} spacing can be obtained. The scattering vector lies perpendicular to the scattering planes.

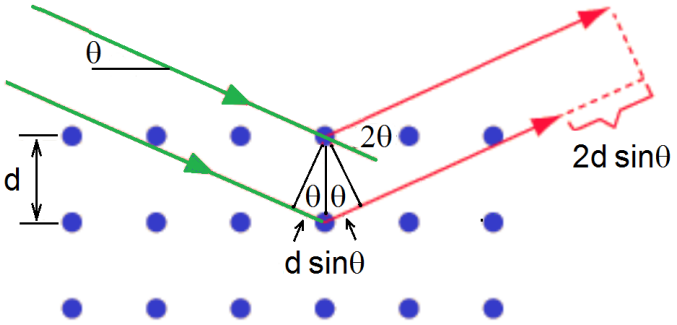

Figure 2.6: Schematic representation of Bragg's law. Monochromatic X-ray beams are incident upon the crystal at an angle θ and scattered by the atomic planes. Constructive interference will occur when the reflected waves are in phase, i.e., the pathlength ($2d\sin\theta$) is equal to an integer multiple of the wavelength λ.

2.3.5 Argand diagram

It has already been mentioned that the structure factor (i.e. scattering amplitude) is a complex quantity and so it can be graphically represented on a complex plane, known as an *Argand diagram* (Figure 2.7). The concept of the Argand diagram allows a geometric interpretation of the interference phenomenon where the individual structure factors are represented as vectors and also provides a graphical description of the phase problem. Such an approach helps to understand why some reflections are strong while others are weak or even not seen (i.e., *systematic absences*) (see Figure 2.8).

In some type of crystals the positions of atoms are such that the scattered waves from the individual atoms cancel each other, and as consequence no Bragg reflection is observed even when the Bragg condition is satisfied. For example, for the face centered cubic lattice, any reflection (hkl) in which there is a mixture of odd and even integers will be forbidden.

2.3.6 Phase problem

In order to reconstruct the real-space electron density map in the unit cell, the inverse Fourier transform of the diffraction pattern has to be performed. For this purpose we need to know both the magnitude and phase of each complex structure factor. Unfortunately in an X-ray diffraction experiment only the diffraction signal intensity is measured i.e., the absolute square

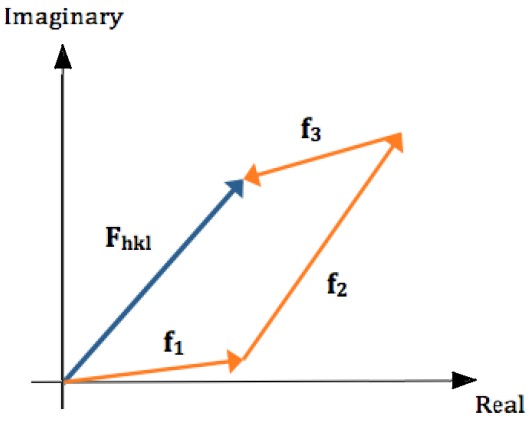

Figure 2.7: The structure factors geometrically represented in the complex plane. The total structure factor $\mathbf{F_{hkl}}$ is the vector sum of all individual atomic form factors $\mathbf{f_1}$, $\mathbf{f_2}$ and $\mathbf{f_3}$

of the structure factor. Therefore we lose the information about the phase in our measurement - this gives rise to the well-known *phase problem*.

Figure 2.8 shows the Argand diagram of a hypothetical unit cell and demonstrates the phase problem graphically. As it is seen, for a given set of atoms within a unit cell, there are multiple possible phase relationships between these atoms that produces the same intensity $I_{hkl} = A^2$. In other words the structure factor may lie on a circle of a radius of $\sqrt{I_{hkl}}$, but the phases of individual scatterers remain uknown. To overcome the phase problem there are various *phase retrieval* methods developed exploiting computation algorithms and multiwavelength X-ray diffraction techniques [16–19].

2.4 Surface diffraction

2.4.1 Crystal truncation rods

In the previous section where bulk diffraction was explained, we considered an ideal bulk crystal as an infinite repetition of unit cells in all three crystallographic directions. Let us consider a surface of an infinitely extended crystal truncated by an 2-dimensional plane. The crystal's periodicity remains intact in the in-plane directions, but the out-of-plane periodicity is broken. Consequently our crystal contains a stack of unit cells from $-\infty$ to 0 in the vertical direction.

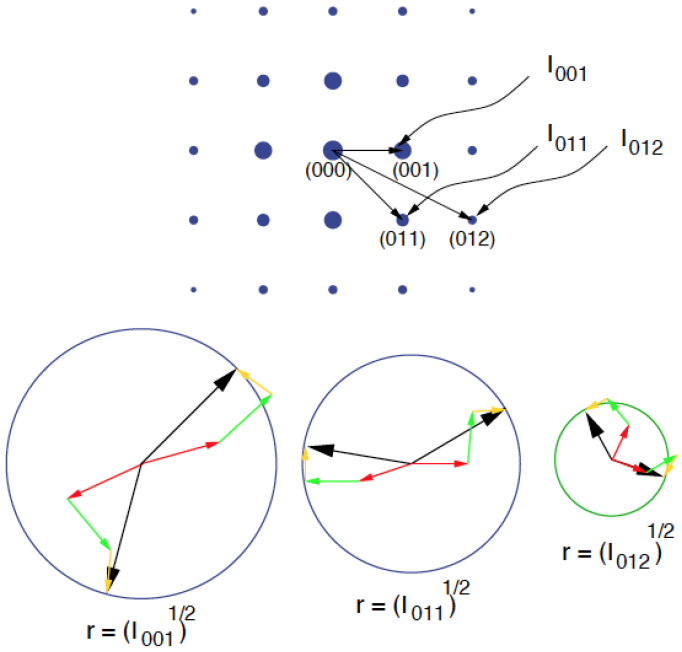

Figure 2.8: Pictorial illustration of the phase problem. Different position within the unit cell result in different phase relationships between the constituent atoms of a unit cell, but can produce the same scattering intensity. Courtesy of [20]

We can use the same approach formulated in Equation 2.15 but now perform a semi-infinite summation in the out-of-plane direction. The summations along other two in-plane directions are untouched. Therefore the scattering amplitude turns into

$$A_s = A_0 \cdot \frac{r_e}{R} \cdot p \cdot e^{i\mathbf{qr}} \cdot F(\mathbf{q}) \cdot \sum_{j_1=0}^{N_1-1} e^{i\mathbf{q}\cdot(j_1\cdot\mathbf{a})} \cdot \sum_{j_2=0}^{N_2-1} e^{i\mathbf{q}\cdot(j_2\cdot\mathbf{b})} \cdot \sum_{j_3=-\infty}^{0} e^{j_3\cdot i\mathbf{qc}} \cdot e^{-\beta}. \quad (2.21)$$

here the new absorption term $e^{-\beta}$ is introduced. The intensity is obtained by squaring the scattering amplitude:

$$I_s(\mathbf{q}) = I_0 \cdot \frac{r_e^2}{R^2} \cdot p^2 \cdot |F(\mathbf{q})|^2 \cdot \frac{\sin^2(\frac{1}{2}N_1 q_x a)}{\sin^2(\frac{1}{2}q_x a)} \cdot \frac{\sin^2(\frac{1}{2}N_2 q_y b)}{\sin^2(\frac{1}{2}q_y b)} \cdot \frac{1}{1-e^{i\mathbf{qc}-\beta}} \cdot \frac{1}{1-e^{-i\mathbf{qc}-\beta}} \quad (2.22)$$

The last two terms for the case of $\beta \to 0$ yeld

$$\frac{1}{1-e^{i\mathbf{qc}-\beta}} \cdot \frac{1}{1-e^{-i\mathbf{qc}-\beta}} = \frac{1}{4\sin^2(\frac{1}{2}\mathbf{qc})}. \quad (2.23)$$

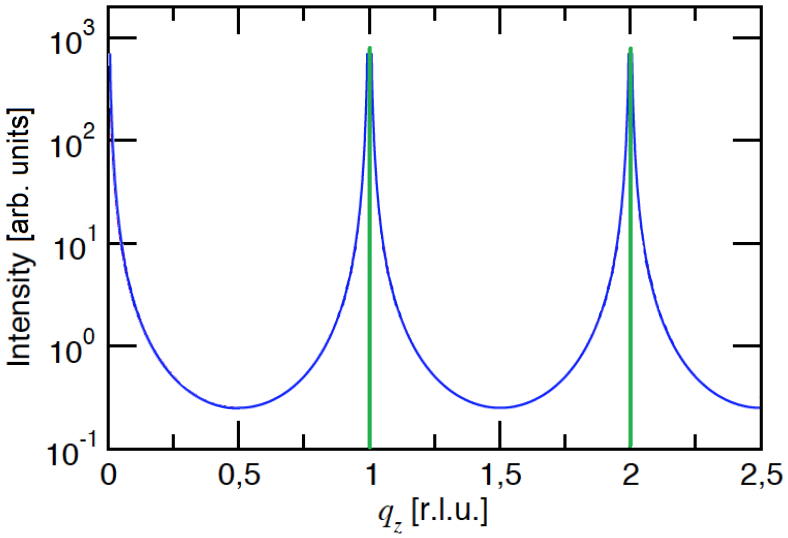

Figure 2.9: A plot of $\frac{1}{4\pi sin^2(\pi l)}$ function (blue line) showing the intensity distribution along a CTR for a perfect surface. As seen, the intensity changes continuously which is due to a tail to each bulk peak. Bulk Bragg peaks are shown in green.

By putting this back into Equation 2.22 we obtain

$$I_s(\mathbf{q}) = I_0 \cdot \frac{r_e^2}{R^2} \cdot p^2 \cdot |F(\mathbf{q})|^2 \cdot \frac{\sin^2(\frac{1}{2}N_1 q_x a)}{\sin^2(\frac{1}{2}q_x a)} \cdot \frac{\sin^2(\frac{1}{2}N_2 q_y b)}{\sin^2(\frac{1}{2}q_y b)} \cdot \underbrace{\frac{1}{4\sin^2(\frac{1}{2}q_z c))}}_{|F_{CTR}(\mathbf{q})|^2}. \tag{2.24}$$

here $\mathbf{qc} = q_z c$ for an orthogonal lattice. The detailed derivation can be found in Ref. [8]. From this equation the intensity distribution along the q_x and q_y directions gives Bragg peaks like in bulk diffraction. However the intensity along q_z is not a δ-function anymore. The last term $\frac{1}{4\sin^2(\frac{1}{2}q_z c))}$ has an intensity tail to each Bragg peak along q_z (Figure 2.9). In other words there is the continuous intensity variation in between successive Bragg peaks along the direction of the surface normal. Such an intensity distribution forms a set of streaks called the *crystal truncation rods* (CTRs).

The origin of CTRs can be understood from the simple perspective using the convolution theorem (see Section 2.2.2). In real space, the crystal surface can be produced by the product of function f describing an infinite lattice and a step function g applying truncation. In order to obtain the structure factor of such a truncated crystal we have to perform the Fourier transform on the product $f(x)g(x)$ (see Figure 2.10). Using the convolution theorem (Equation 2.6) we

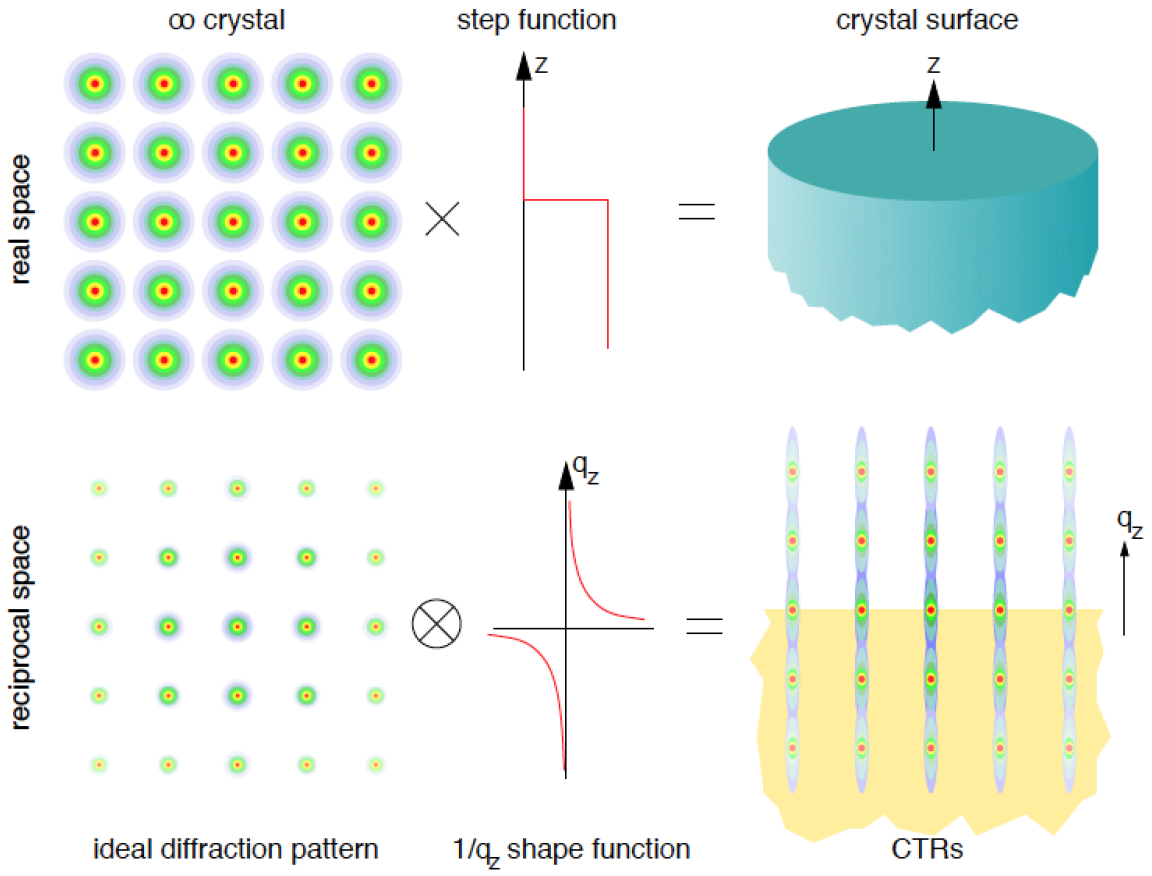

Figure 2.10: A pictorial explanation of the origin of the crystal truncation rods using the convolution theorem (Courtesy of [21]).

obtain

$$FT\big[f(x)\cdot g(x)\big] = FT\big[f(x)\big] \otimes FT\big[g(x)\big]. \tag{2.25}$$

The Fourier transform of the step function has $1/q_z$ relationship whereas the Fourier transform of the crystal lattice is an ideal diffraction pattern. The convolution of these functions produces a continuous signal between the Bragg peaks along q_z.

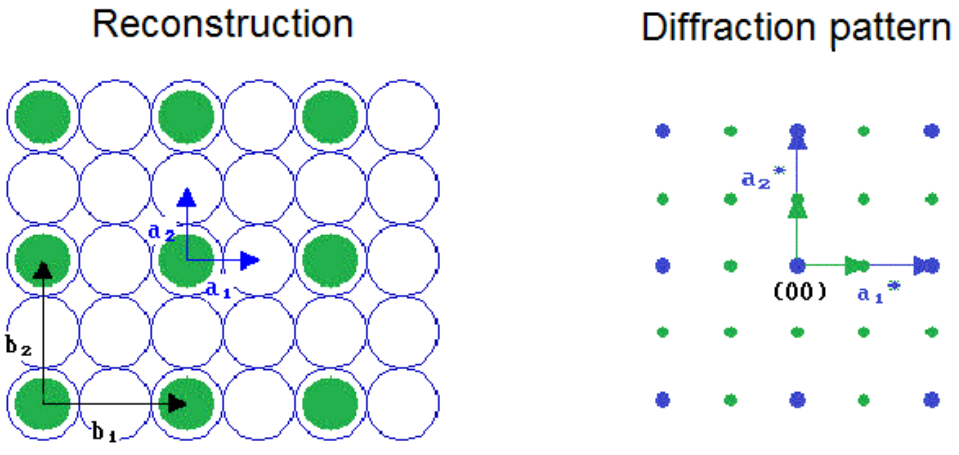

Figure 2.11: Ilustration of (2×2) reconstructed surface (left) and the resulted diffraction pattern (right).

2.4.2 Superstructure rods

Atoms located in the bulk region of a crystal experience the equal forces exerted by all the other surrounding atoms and therefore maintain a regular periodic order. However atoms at the crystal surface experience a different bonding environment that breaks the periodicity. The latter causes the atoms from the near surface region to rearrange in order to achieve a lower overall energy. Such a rearrangement is referred to as a relaxation or reconstruction. The resulting surface region has a different structure than that of the bulk. If we consider X-ray diffraction, apart from the "regular" Bragg peaks in a diffraction pattern, there will be rods associated with the surface structures. These extra rods are called the *superstructure rods* (SSRs). Let us consider the diffraction pattern of the reconstructed surface. Assume that the surface structure is $m \times n$ times larger than the bulk structure, then there will be superstructure spots separated by $2\pi/ma$ and $2\pi/nb$ where a and b are the in-plane lattice constants of the bulk crystal (see Figure 2.11). Similar to CTRs, the surface structure generates SSRs. However SSRs do not exhibit Bragg maxima (which are bulk phenomena) and have intensities comparable to those of the weakest part of the CTRs.

2.5 SXRD measurements

Typically surface X-ray diffraction measurements are performed at small incidence angles α with respect to the sample surface. The value of α can be above or below the critical angle and the choice depends on the experiment and the sample of investigation. For example for high surface sensitivity, α has to be close or below the critical angle. This limits the scattering originating from the bulk of the sample and reduces the diffuse scattering background as well. On the other hand when studying buried interfaces, it is crucial that X-rays can penetrate deep enough into the sample.

Data collection at the surface X-ray diffraction station of the Materials Science beamline at the Swiss Light Source, Paul Scherrer Institut, is completely automatised. The software SPEC calculates all the motor positions for the specified (hkl) positions and further sends a set of commands to the diffractometer control unit. The detector exposure time and filters transmission are dynamically adjusted during data acquisition, depending on the signal intensity. Before the actual SXRD measurements, the diffractometer motors have to be aligned and zeroed and also the sample surface has to be aligned with respect to the diffractometer centre. This involves very precise adjustments of the hexapod motors while monitoring the specularly reflected X-ray beam from the sample surface seen on the detector.

2.5.1 Reciprocal space scans

To record integrated intensities in reciprocal space we need to position both the sample and the detector such that the elastic diffraction condition is fulfilled. In this case a particular (hkl) point has to lie on the Ewald sphere and the recorded signal on the detector is given by the intersection with the Ewald sphere (see Figure 2.12). In the SXRD experiment the intensity maximum given in Equation 2.19 cannot be measured directly. The diffraction conditions on the sample are not absolutely perfect. In general crystals have mosaicity where different parts of the crystal are not exactly parallel, the incoming beam is never perfectly parallel and so has divergence. All these factors make the observable diffraction peak broader. Measurement of this signal is achieved via integration of the intensity distribution.

2D-detectors have revolutionised X-ray diffraction techniques and provide accurate and fast operation for data acquisition [21–23]. There are different methods of data recording using 2D-detectors and we briefly describe them in the following sections.

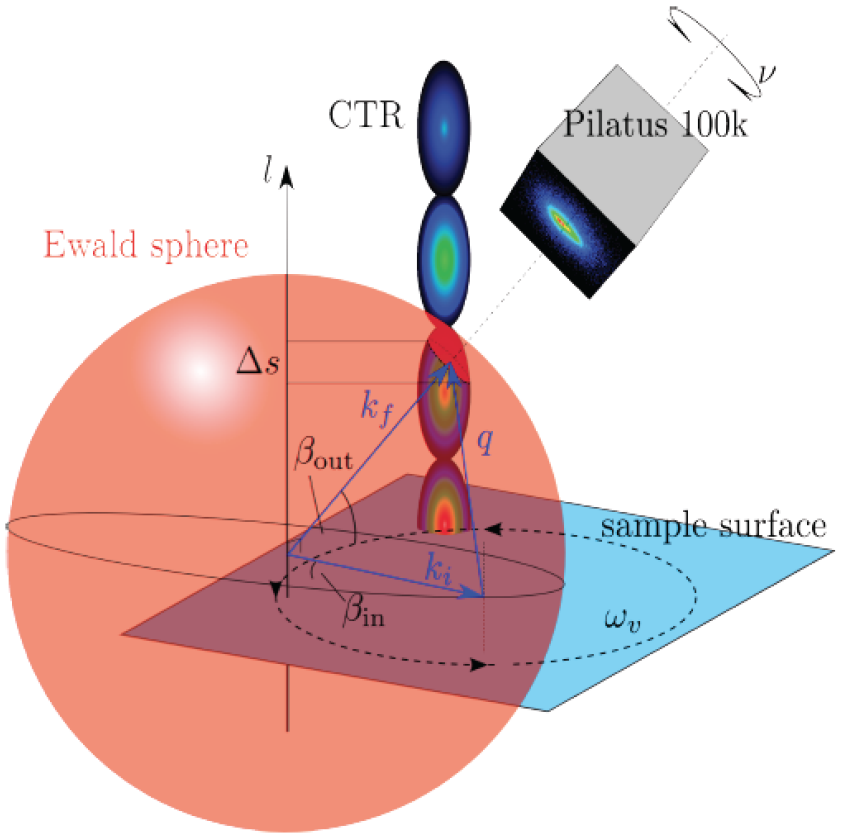

Figure 2.12: Illustration of the experimental geometry demonstrating a typical SXRD measurement with a PILATUS 100k detector. Courtesy of [24]

2.5.2 Rocking scans

In SXRD experiments CTRs and SSRs can be recorded using so-called *rocking scan*. In this procedure a position on a rod is chosen by orienting the sample as well as putting a detector at an appropriate angular position. Then the sample is rotated between positive and negative values around its surface normal (ω_v-axis). Consequently, the intersection point of the rod with the Ewald sphere moves either up or down. During the sample rotation, the detector position is fixed. This procedure is repeated around as many points on the rod as possible. The integrated intensity of each rocking scan is extracted and the intensity of the measured rod as function of l is obtained. In contrast to a point detector where the rocking scan is taken for each l-value, a 2D-detector allows the acquisition of multiple rocking curves from one

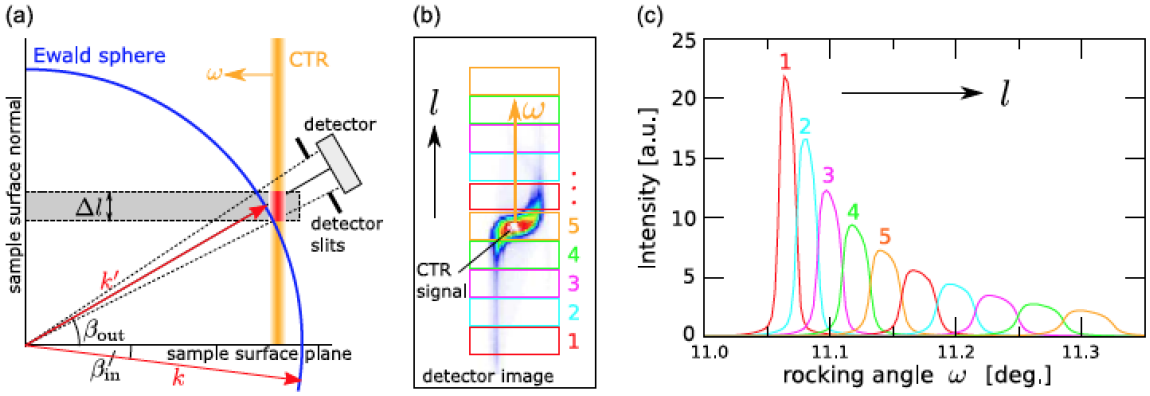

Figure 2.13: Graphical explanation of the rocking scan. (b) An array of region of interests (ROI) are defined on the area detector. While performing one single ω-scan the signal moves on the detector such a way that is passes all these ROIs. The integrated intensity is integrated inside of each ROI and the multiple rocking curve is produced (c). Courtesy of [25]

rocking scan. This is done in the following manner: On an area of the 2D-detector, an array of regions of interest (ROIs) is defined using software [Figure 2.13(b)]. Subsequently from a single rocking scan, the signal passes through several ROIs, producing a series of corresponding rocking curves [Figure 2.13(b)] [23].

2.5.3 Stationary mode

Instead of taking rocking scans, the structure factor along the l-direction can be also recorded in the *stationary mode*. The CTR intersection with the Ewald sphere at a certain l-value is captured in a single image. It is achieved using a 2D-detector with widely open slits. The whole CTR is recorded in one single l-scan, and the total acquisition time is therefore significantly reduced. However, the stationary mode has limitations. When the CTR intercepts with the Ewald sphere, the captured signal has a range of l-values, denoted by s, depending on where the Ewald sphere cuts the CTR (Figure 2.14), and is expressed as

$$s \propto \frac{1}{\sin(\beta_{out})}. \tag{2.26}$$

The stationary mode is applicable when s is smaller than the desired resolution Δl along the l-direction, defining a minimum outgoing angle β_{out}. The minimum outgoing angle limits the

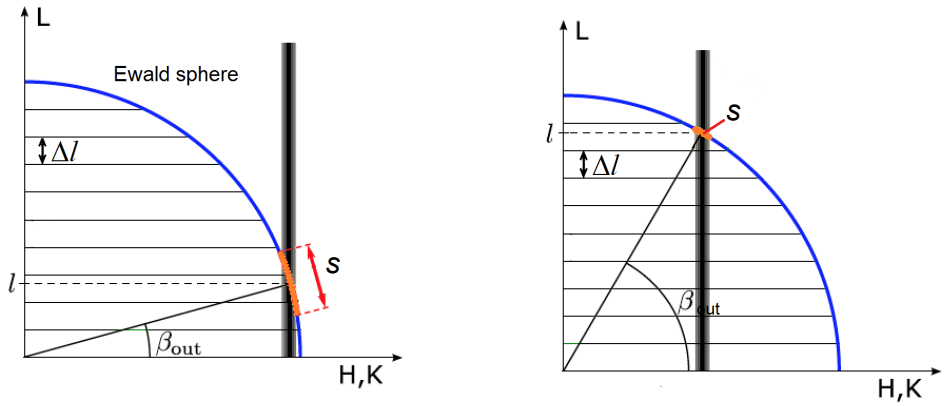

Figure 2.14: Because of the finite width of a CTR, its intersect (s) with the Ewald sphere depends on β_{out}. At very low l, s may exceed the desired resolution Δl.

lowest accessible l range respectively. For a given resolution Δl, the lowest value β_{out} is defined through

$$\tan \beta_{out} \geq \frac{2\Delta Q_{FWHM}}{b^* \Delta l} \tag{2.27}$$

where ΔQ_{FWHM} is the the full-width at half-maximum of the CTR in the in-plane direction and b^* is the in-plane reciprocal lattice vector.

2.5.4 In-plane scans

The in-plane lattice constant and size of superstructures are obtained via measuring diffraction intensities from the lattice planes normal to the surface of a sample. This is done using so-called in-plane scans along the reciprocal space directions h or k.

2.5.5 Data Extraction and correction

The PILATUS 100k photon-counting detector records images for each consecutive exposure of a scan. The acquired image represents the 2-dimensional array of pixels. The pixel values are the number of recorded counts. Further analysis of the images is the most critical and challenging task. In order to extract the integrated intensity, first a reasonable signal region of interest is defined and then the background signal is fit and substracted (Figure 2.15) In some

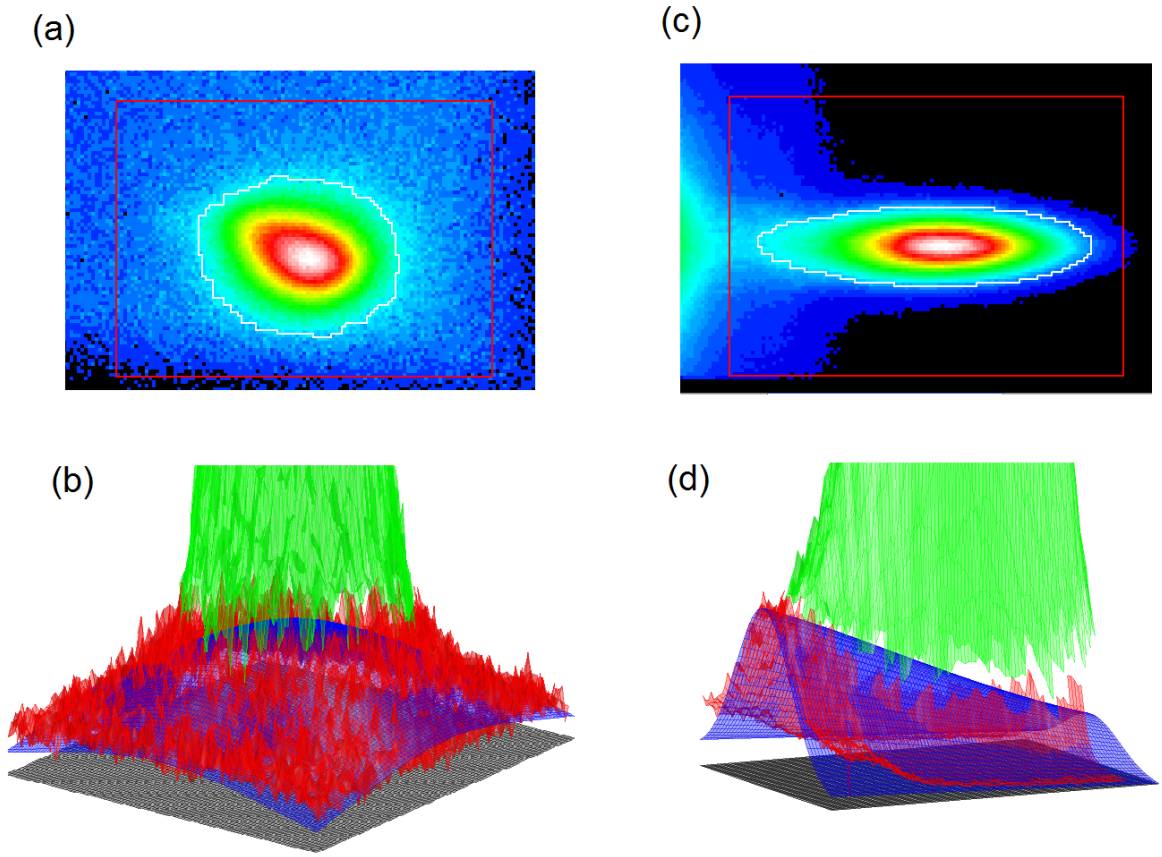

Figure 2.15: Examples of the signal extractions: The top row shows the detector images with the signal (white) and the background (red) region of interests. The background fits are shown in the bottom row with signal (green), measured background (red) and fitted background (blue). (a)(00l) CTR of PtRh(111) crystal far away from a Bragg peak at $l = 3.5$ and corresponding background fit (b) using a 2D Gauss function. (c) The same CTR but close to the Bragg peak at $l = 2.9$. The gradient component on top of the diffuse background comes from the Bragg peak and is fit using a 2D Gaus + linear function (d).

cases it is difficult to discriminate the real signal and the background across the image. The extraction procedure is done using dedicated software available at the MS beamline [25].

After extraction of intensities from the detector images, the necessary correction factors have to be applied. Depending on the scan, experimental setup, and the sample geometry, the intensity-correction routine involves the following correction factors. More detailed descriptions

can be found in [21, 25]:

Flat field correction The counting efficiencies for all pixels of the PILATUS detector are not exactly the same. Before the actual measurement, the response of each pixel has to be calibrated. This is achieved using the flat-field correction procedure. The detector is illuminated with homogenous radiation and a sufficiently large number of images are recorded. Then taking statistics from each image, the individual pixel sensitivity is corrected and the flat-field image is produced. Any raw image can be corrected according the flat-field image.

Polarization factor The polarization correction factor accounts the polarization content of the X-ray beam. It depends on the detector angles parallel (γ) and perpendicular (δ) to the polarization plane as follow [25]

$$C_P = \frac{1}{P} = \left[p_h(1-\cos^2\delta\sin^2\gamma) + (1-p_h)(1-\sin^2\delta)\right]^{-1}. \tag{2.28}$$

here p_h is the polarization in the horizontal plane which is about 98 % for the MS beamline at 12 keV.

Rod interception and Lorentz factor The crystal truncation rod has a finite width and so its interception with the Ewald sphere depends on the outgoing angle (β_{out}). This situation is shown in Figure 2.14. The integrated signal must therefore be corrected for the amount of the vertical component Δl of the CTR that is recorded. The latter gives rise to a correction which is called the *rod interception factor* expressed as:

$$C_I = \sin(\beta_{out}) \tag{2.29}$$

When recording the diffractopn data, different reciprocal lattice points traverse the Ewald sphere at different speeds depending the distance from their position to the rotation axis. The special *Lorentz factor* corrects the length of time spent by different reflections in the diffraction condition taking into account the geometrical configuration of an experiment. For the ω-scan where the detector is stationary, the Lorentz correction takes the simple form

$$C_L = \frac{1}{\sin(2\theta)} \tag{2.30}$$

Active area The integrated intensity has to be normalized with respect to the total incident flux over the sample surface. This is achieved by introducing an *active area correction factor*.

In some cases this factor is not constant. For example, whilst measuring the specular CTR, the X-ray beam footprint across the sample surface varies with incoming angle (β_{in}). It also may change depending on the sample shape.

2.6 Experimental setup

2.6.1 The Materials Science beamline

The Material Science beamline at the Swiss Light Source has been designed to perform diffraction experiments and hosts two stations dedicated for Surface diffraction (SD) and powder diffraction. The beamline has an insertion device which produces hard X-rays over an energy range of 5-40 keV. A detailed description of the beamline can be found elsewhere [26].

The beamline layout is shown in Figure 2.16. The so-called "front end" of the beamline consists of beam-defining aperture, the soft X-ray window and beam-defining slits. The X-ray diamond window filters out incoming radiation for energies below 5 keV. The beamline primary optics consist of a double-crystal monochromator (DCM) and two focusing mirrors. After beam-defining slits the beam hits the Si DCM and gets monocromatized by (111)-reflection. In addition to redirecting the beam in the horizontal direction, the second DCM-crystal is responsible for horizontal focusing, while the two focusing mirrors provide vertical focusing and define the height of the beam.

2.6.2 The diffractometer

The surface X-ray diffraction endstation is equipped with a (2+3) circle Newport diffractometer (Figure 2.17). The sample motion has azimuthal and polar degrees of freedom. The detector arm has three degrees of freedom: in-plane (γ), out-of-plane (δ) and around the detector (ν). The diffractometer can operate either in vertical or horizontal mode depending on the requirements of the experiment. In the vertical mode, motors α, ω_v, δ, γ and ν are used, while for the horizontal mode, motors ϕ, ω_h, γ, δ, and ν are used. The normal to the diffractometer base plane can be adjusted (i.e., a whole platform tilt) using three vertical linear motors Y_1, Y_2 and Y_3. The hexapod where the sample is mounted has 3 translational and three rotational degrees of freedom. The diffractometer motors are controlled via the software environment SPEC.

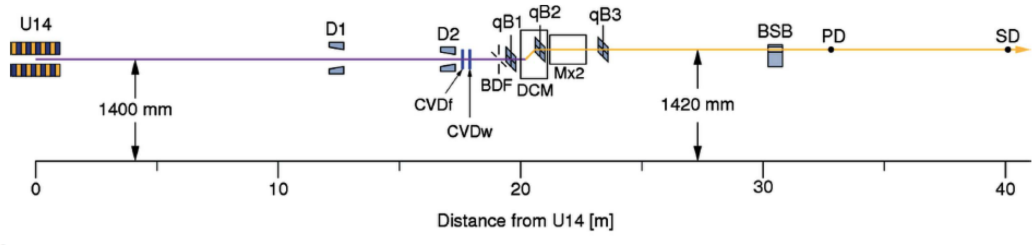

Figure 2.16: The Material Science Beamline (MS), SLS. A strong X-ray beam is produced when electrons in a storage ring travel through the U14 undulator insertion device. Then the photon beam passes through the so-called front end. The beam-defining apertures (D_1, D_2) remove the outer part of the radiation cone. The soft X-ray window (CVDf, CVDw) made of diamond acts as filter which suppresses photon energies below 5 keV. The beam-defining slits (BDF) reduce the divergence of the X-ray beam. In the optics, a double-crystal monochromator (DCM) performs energy selection by changing the Bragg angle and also provides horizontal collimation of the beam. Vertical focusing is achieved using two separate X-ray mirrors. After the X-ray beam has passed all the beamline elements, it hits the sample and the diffraction signals are recorded with the 2D PILATUS 100k detector. Courtesy of [26]

2.6.3 The PILATUS 100k detector

The SD endstation uses a PILATUS 100k single photon counting area detector developed at the Paul Scherrer Institut. It has an active area consisting of $487 \times 195 = 94965$ pixels with each pixel size of (172×172) μm^2. In the present setup the detector is mounted 1116 mm away from the diffractometer center and so the total angular acceptance of the whole area is of $(4.285 \times 1.716)^{\circ}$. The PILATUS detector consists of a hybrid array of single silicon sensors combined with a metal oxide semiconductor (CMOS) chip. This technology provides single-photon counting capabilities without readout noise. Each pixel has a high dynamic range (2^{20}). The PILATUS functionality allows one to set a low-energy threshold for pixels in order to suppress fluorescence background coming from the sample. The readout time is approximately 5 ms, allowing a frame rate up to 200 Hz. In addition, the detector exposure can be synchronized with an external trigger. In general, the advantage of area detectors compared to point detectors is recording the entire image with the diffraction signal and surrounding background. The images can be monitored during the scan and the reasonable region of interest can be adjusted whenever it is needed.

The PILATUS 100k offers fast counting rates for continuous readout, high dynamic range

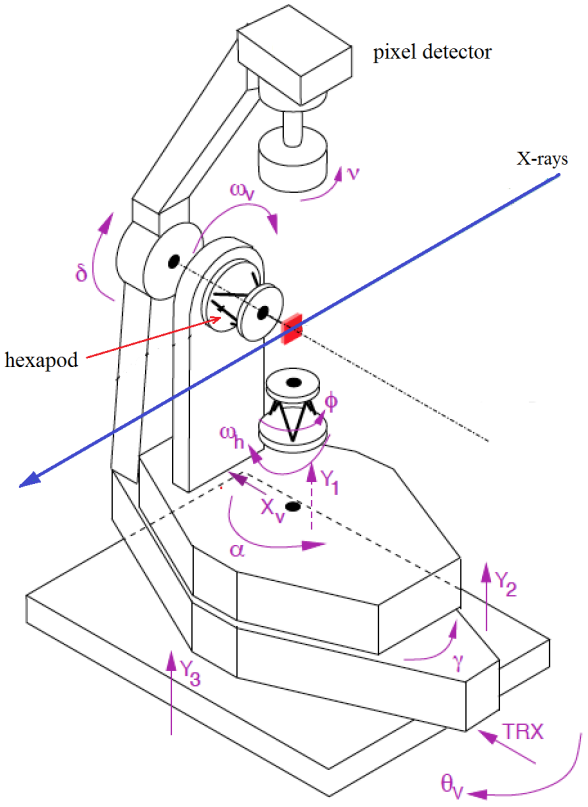

Figure 2.17: Schematic figure of the (2+3)-circle diffractometer of the Surface Diffraction station of the Material Science beamline at the SLS. All detector and sample motors are shown.

for large variations of signal intensities and zero dark noise. The combination of these features are important for modern X-ray diffraction experiments. Further details about the PILATUS detectors can be found in the literature [27, 28].

2.6.4 Environmental chambers

Most X-ray diffraction studies on atomically clean surfaces requires a contamination-free environment for the duration of the experiment. For this reason high-quality samples can only be maintained in ultrahigh vacuum conditions (UHV). Exposure of an atomically clean surface to oxygen, water and other contaminants influences the structure of the surface. In this case the surface can undergo either chemisorption or physisorption depending on adsorbate composition. Chemisorption often causes the formation of chemical bonds between the surface

and contaminants, resulting in more severe structural changes than physisorption. To avoid all of these contamination-related effects, the well-prepared clean samples have to be kept under UHV conditions.

The samples presented in this thesis, single layers of epitaxial graphene and hexagonal boron nitride are sensitive to contaminants. The sample preparation and pre-characterization were performed at the ESCA lab at the physics institute at the University of Zürich. Further transfer of samples to the MS beamline without breaking vacuum is performed using a special transportable UHV-baby chamber [Figure 2.18(a)][24]. It is equipped with a hemispherical beryllium dome suitable for in-situ SXRD-measurements. A battery-powered ion pump allows one to maintain UHV conditions during transport. The sample-holder mechanism accommodates standard Swiss Stub sample holders and allows one to heat the sample via resistive or filament heating. The whole chamber can be directly mounted onto the hexapod.

For the low-temperature SXRD experiments there is a UHV cryostat available at the MS beamline [Figure 2.18(b)]. It has a hemispherical Be-dome similar to the baby chamber. The lowest achievable temperature is currently 13 K. The sample movements (rotation and fine adjustments) are decoupled from the vacuum vessel using bellows and a ferrofluid rotary feedthrough, thereby providing safe mechanical flexibility. The copper braids connect the sample holder to the Janis ST continuous He-flow cryostat. Also it can be heated to 500K. This UHV cryostat has been extensively used in in-situ experiments on Xe deposition on hexagonal boron nitride nanomeshes.

2.7 SXRD on surface structures

Surface X-ray diffraction is a non-destructive technique for studying surface structures, reconstructions and even one-atom thick layers grown on different substrates. In this section, we demonstrate how SXRD is applied to studying the surface structures. Let us consider the case of an overlying structure of boron grown on a rhodium substrate. For simplicity we discuss the one-dimensional example shown in Figure 2.19. First we start with a non-reconstructed structure. 10 unit cells of the adlayer structure are accommodated on 10 u.c.s of the substrate. In reciprocal space, there will be a crystal truncation rod of the substrate and relatively weak Bragg-rod associated with the lattice periodicity of the adlayer. These two rods sit at the same position $h = 1 = 10/10$. If we now consider the structure where 11 u.c.s are located on 10 u.c.s

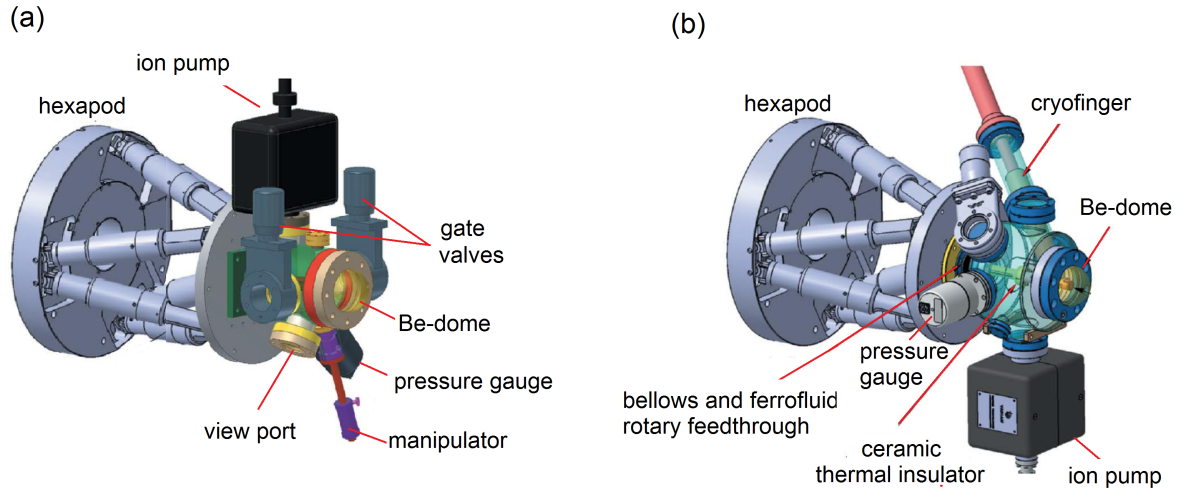

Figure 2.18: (a) Schematic drawing of chambers available at the SD station. (a) The UHV-baby chamber for experiments requiring UHV-conditions. It is equipped with an X-ray transparent beryllium dome with an inner radius of 31.5 mm and a thickness of 0.4 mm. The samples are transferred via a DN40CF flange from another UHV-chamber while maintaining vacuum. A small manipulator is used to fix the Swiss stub sample holder within the chamber and to attach a heater contact. A battery supply of 2 $\times$12 V provides power to an ion pump for more than 20 hours. (b) UHV-cryostat chamber for low-temperature experiments as low as 13K. It is equipped with similar Be-dome. The sample movements are decoupled from the vacuum vessels using bellows and a ferrofluid rotary feedthrough. The sample mount is made from copper. A ceramic spacer thermally isolates the sample mount from the rest of the chamber. A Janis ST-4001 UHV continuous-flow cryostat is connected to the sample holder via copper braids. An ion pump ensures vacuum in the mid 10^{-10} mbar range. From ref. [26]

of the substrate (11-on-10), in addition to the substrate CTR, the superstructure rod (SSR) of the adlayer is visible at $h = 11/10$.

Sometimes the lattice mismatch of an adlayer with the substrate is such that it imposes a superstructure (i.e. supercell) formation which manifests itself through additional signal components in the recorded data set. We now consider the same 11-on-10 model but with a corrugated adlayer. Here the translational symmetry is maintained as the periodicity of the corrugated adlayer is the same as that of the 10 underlaying substrate atoms. Consequently, the superstructure size is 10 times larger than the substrate unit cell and therefore all the rods

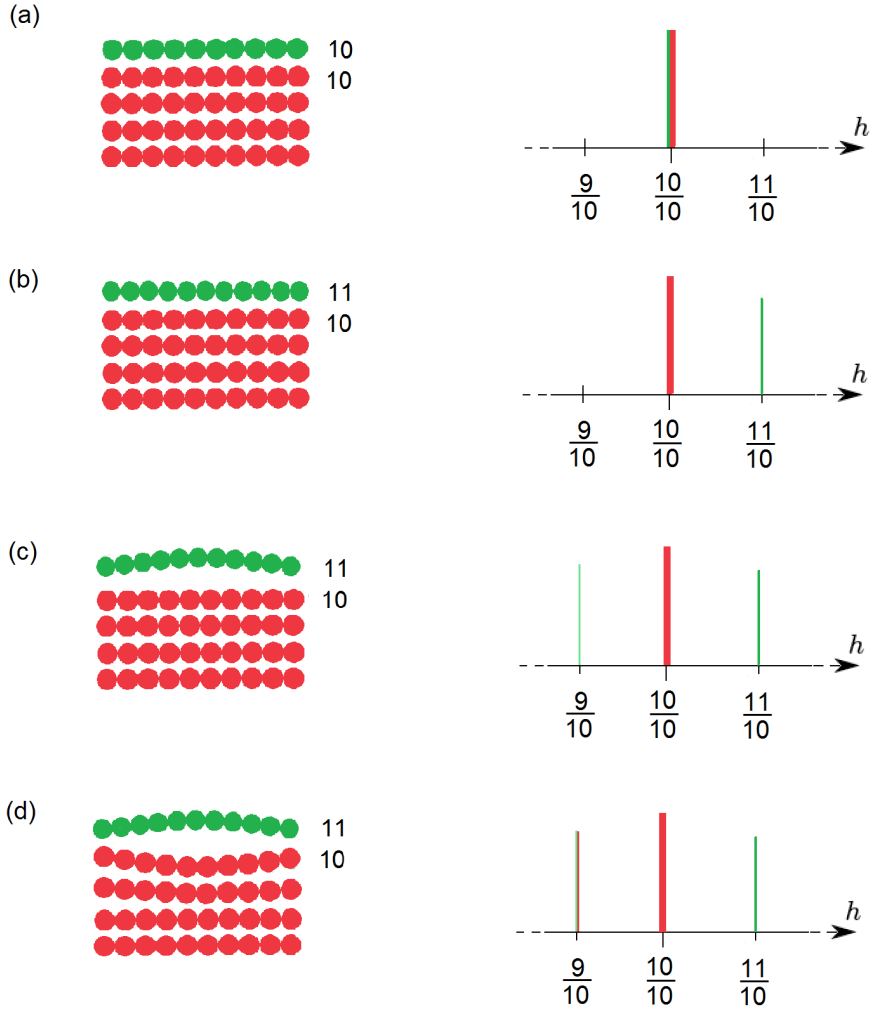

Figure 2.19: A schematic example of the surface structures (left) and corresponding in-plane scan (right): (a) 10-on-10 structure. (b) flat commensurate 11-on-10 reconstruction. (c) 11-on-10 structure with the corrugated adlayer. (d) 11-on-10 structure with the corrugated adlayer and substrate.

having $h = 1/10$ Fourier-components are raised. It is very common that the strained overlayer induces buckling on the substrate down to several atomic layers. In this case all $h = 1/10$-rods appear to be enhanced because there are more scatterers involved in the substrate supercells. In SXRD, superstructures are easily detected by in-plane scans (see 2.5.4). Usually a high resolution scan is preferred near the first Bragg peak of the substrate at fixed l value. Using this method, an 11-on-10 reconstruction of hexagonal boron nitride on PtRh alloy was successfully

established (see Chapter 4).

Bibliography

[1] W. Friedrich, P. Knipping, and M. Laue: "Interferenzerscheinungen bei Röntgenstrahlen." *Annalen der Physik* **346**(10), 971–988 (1913).

[2] M. von Laue: "Concerning the detection of X-ray interferences." *Nobel lecture* (1915).

[3] W. H. Bragg and W. L. Bragg: "The structure of the diamond." *Nature* **91**, 557 (1913).

[4] W. L. Bragg, R. W. James, and C. H. Bosanquet: "XXIX. The intensity of reflexion of X-rays by rock-salt." *The London, Edinburgh, and Dublin Philosophical Magazine and Journal of Science* **41**(243), 309–337 (1921).

[5] W. L. Bragg, R. W. James, and C. H. Bosanquet: "I. The intensity of reflexion of X-rays by rock-salt.Part II." *The London, Edinburgh, and Dublin Philosophical Magazine and Journal of Science* **42**(247), 1–17 (1921).

[6] W. L. Bragg: "The structure of some crystals as indicated by their diffraction of X-rays." *Proceedings of the Royal Society of London. Series A* **89**(610), 248–277 (1913).

[7] M. F. Perutz: "How W.L Bragg invented X-ray analysis." *Acta Crystallographica Section A: Foundations of Crystallography* **46**(8), 633–643 (1990).

[8] I. K. Robinson and D. Tweet: "Surface x-ray diffraction." *Reports on Progress in Physics* **55**(5), 599 (1992).

[9] R. Feidenhans'l: "Surface structure determination by X-ray diffraction." *Surface Science Reports* **10**(3), 105–188 (1989).

[10] W. C. Marra, P. Eisenberger, and A. Y. Cho: "X-ray total-external-reflection–Bragg diffraction: A structural study of the GaAs-Al interface." *Journal of Applied Physics* **50**(11), 6927–6933 (1979).

[11] P. Eisenberger and W. C. Marra: "X-ray diffraction study of the Ge (001) reconstructed surface." *Physical Review Letters* **46**(16), 1081 (1981).

[12] J. D. Jackson: *Classical electrodynamics, 3rd Edition* (1998).

[13] U. Shmueli, T. Hahn, E. Prince, and A. J. C. Wilson: *International Tables for Crystallography, Mathematical, Physical and Chemical Tables*, volume C. Springer (2004).

[14] E. G. McRae: "Self-consistent multiple-scattering approach to the interpretation of low-energy electron diffraction." *Surface Science* **8**(1), 14–34 (1967).

[15] P. P. Ewald: *Kristalle und Röntgenstrahlen*, volume 6. Julius Springer (1923).

[16] H. Hauptman: "Phasing methods for protein crystallography." *Current opinion in structural biology* **7**(5), 672–680 (1997).

[17] G. Taylor: "The phase problem." *Acta Crystallographica Section D: Biological Crystallography* **59**(11), 1881–1890 (2003).

[18] S. E. Ealick: "Advances in multiple wavelength anomalous diffraction crystallography." *Current opinion in chemical biology* **4**(5), 495–499 (2000).

[19] A. L. Patterson: "A Fourier series method for the determination of the components of interatomic distances in crystals." *Physical Review* **46**(5), 372 (1934).

[20] P. R. Willmott: *An introduction to synchrotron radiation: Techniques and applications*. John Wiley & Sons (2011).

[21] C. M. Schlepütz, R. Herger, P. R. Willmott, B. D. Patterson, O. Bunk, C. H. Bronnimann, B. Henrich, G. Hulsen, and E. F. Eikenberry: "Improved data acquisition in grazing-incidence X-ray scattering experiments using a pixel detector." *Acta Crystallographica Section A: Foundations of Crystallography* **61**(4), 418–425 (2005).

[22] P. R. Willmott, C. M. Schlepütz, R. Herger, B. D. Patterson, O. Bunk, C. H. Brönnimann, B. Henrich, G. Hülsen, and E. F. Eikenberry: "Technical Reports: A Single-photon Counting Pixel Detector for Surface Diffraction Experiments." *Synchrotron Radiation News* **18**(2), 16–22 (2005).

[23] S. J. Leake, M. L. Reinle-Schmitt, I. Kalichava, S. A. Pauli, and P. R. Willmott: "Cluster method for analysing surface X-ray diffraction data sets using area detectors." *Journal of Applied Crystallography* **47**(1), 207–214 (2014).

[24] D. Martoccia: *Structural Studies of h-BN and Graphene Single-Layers on Transition- Metal Surfaces*. Ph.D. thesis, Universität Zürich, Zurich (2009).

[25] C. M. Schlepütz: *Systematic Structure Investigation of YBCO Thin Films with Direct Methods and Surface X-ray Diffraction*. Ph.D. thesis, Universität Zürich, Zurich (2009).

[26] P. R. Willmott, D. Meister, S. J. Leake, M. Lange, A. Bergamaschi, M. Boge, M. Calvi, C. Cancellieri, N. Casati, A. Cervellino, *et al.*: "The Materials Science beamline upgrade at the Swiss Light Source." *J. Synch. Rad.* **20**(5), 667–682 (2013).

[27] C. H. Broennimann, E. F. Eikenberry, B. Henrich, R. Horisberger, G. Huelsen, E. Pohl, B. Schmitt, C. Schulze-Briese, M. Suzuki, T. Tomizaki, *et al.*: "The PILATUS 1M detector." *Journal of synchrotron radiation* **13**(2), 120–130 (2006).

[28] A. Bergamaschi, C. Broennimann, E. F. Eikenberry, B. Henrich, M. Kobas, P. Kraft, and B. Schmitt: "Experience and results from the 6 megapixel PILATUS system." In *Proc. 16th International Workshop on Vertex detectors* (2007).

Chapter 3

Surface X-ray diffraction study of graphene on Ru(0001)

3.1 Introduction

This chapter describes experiments performed by Surface X-ray diffraction (SXRD) on the graphene on Ru(0001) system. A detailed summary of results based on density functional theory (DFT), scanning tunneling microscopy (STM) and SXRD is provided: The DFT optimized models of graphene/Ru(0001) superstructures are introduced and their essential structural characteristics described. Secondly, STM studies on the graphene/Ru(0001) supercell are presented, where two different and distinct hill species in the corrugation are observed. Finally, a comparison and evaluation of the DFT structure using the SXRD data, analyzed using different parameterization strategies are discussed in detail. An important goal in this last part is to estimate the graphene peak-to-peak corrugation height and its associated confidence interval, the topic of Section 3.5.

3.1.1 Previous studies on graphene/Ru(0001)

In this section, an overview of previous structural studies on graphene/Ru(0001)(g/Ru) using low energy electron diffraction (LEED) and SXRD techniques is given. Although several investigations were carried on this system [1–4], it was unclear until the work of Martoccia *et al.* [5]

what exact registry exists between graphene and the Ru substrate. Early studies suggested a reconstruction in which (12×12) unit cells of graphene sit on (11×11) unit cells of ruthenium [6, 7] (henceforth referred to as "12-on-11"), while an 11-on-10 structure was also reported [8]. Considering an in-plane bulk lattice constant of graphene (2.4612 Å) and ruthenium (2.706 Å), the former structure would have an in-plane tensile strain of 0.78%, while the latter would be compressively strained by only 0.05% [9]. Conventional LEED precludes a resolution accurate enough to resolve the positions (1.100 and 1.0909 in-plane reciprocal lattice units) of the first-order diffraction spots associated with these superstructures as they lie within less than 0.01 reciprocal lattice units of one another. Only surface X-ray diffraction allows unambiguous identification of the real reconstruction signal. On the other hand the supercell structure determination in real space from STM imaging is insufficiently reliable because of ambiguities between real differences in height and differences in the local density of states near the Fermi level. For example, from the Fourier transform of a STM resolved image an 11-on-10 structure was elucidated [8]. In this work, the importance of electronic states has been demonstrated from the fact that the apparent corrugation of the graphene structure varied with the tunneling voltage, ranging from 0.1 nm (at a sample voltage of -1 V) to 0.02 nm (at +1 V). The graphene superstructure surface exhibits charge inhomogenities in the charge distribution. The observed corrugation is larger at the hills because of charge accumulation which is manifested in occupied electronic states. It becomes smaller at the lower part of the hills since relatively less occupied electronic states are presented [10]. The first SXRD investigation of g/Ru performed by Martoccia *et al.* [5] revealed unambiguously that the reconstruction is in fact surprisingly large, in which 25×25 graphene unit cells lie commensurately on 23×23 unit cells of Ru. The graphene layer has an in-plane tensile strain of 1.15 %. Figure 3.1(b) – (d) shows high-resolution in-plane scans along the k direction of reciprocal space, demonstrating the 25-on-23 reconstruction. The 25/23 signal in itself only provides the graphene lattice periodicity. It indicates that the graphene superstructure constitute a (25×25) superlattice with respect to the C lattice. The presence of the 21/23 signal, however, indicates a true commensurate 25-on-23 superstructure. The possible positions where 13-on-12 and 12-on-11 reconstruction diffraction signals would lie are also indicated. The out-of-plane scans of the 21/23 and 25/23 superstructure rods (SSRs) are shown in Figure 3.1(e). These rods fluctuate significantly in their intensities, with characteristic widths (of the order of 0.2 out-of-plane reciprocal lattice units, r.l.u.) that indicate that not only graphene, but also the underlying Ru substrate, is significantly corrugated and perturbed from its bulk structure down to several

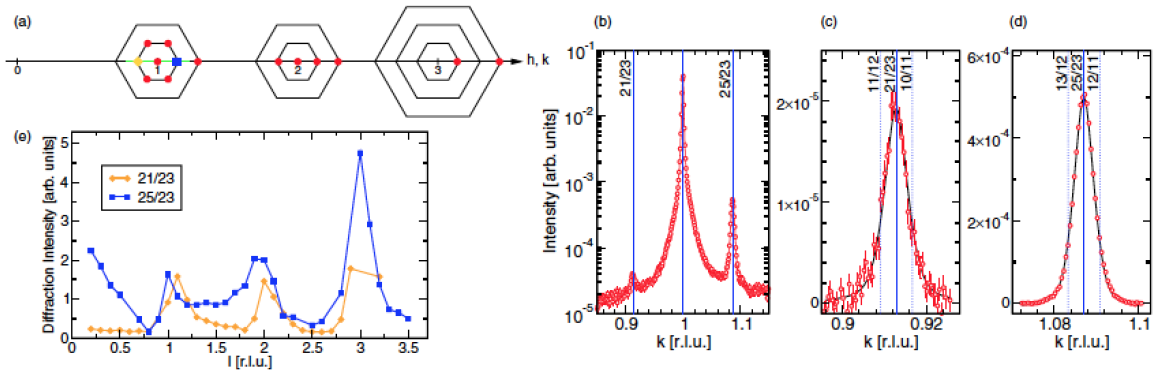

Figure 3.1: Summary of the diffraction data for the graphene/Ru(0001) system. (a) Schematic reciprocal space map showing where data were recorded. The red circular dots indicate points recorded in plane at $l = 0.4$ r.l.u. The in-plane scan along the k-direction in the neighborhood of the (01) CTR of Ru at $l = 0.4$ r.l.u. shown in (b) is indicated by the green (gray) line. The positions of the superstructure rods shown in (e) are indicated by the orange diamond and blue square. (c),(d) High-resolution scans across the superstructure signals of g/Ru, demonstrating the high reliability and accuracy of the discovered 25-on-23 reconstruction. The data were fitted to a pseudo-Voigt profile (solid black curves), while the positions where 13-on-12 and 12-on-11 reconstruction diffraction signals would lie (dotted lines) are also shown. Reprinted figures with permission from [5]. Copyright 2008 by the American Physical Society.

atomic layers.

It is important to note that from the SXRD and the STM data it was concluded that the graphene supercell must consist of four translationally inequivalent subcells, whereby 2×2 corrugation periods are found within a supercell. Consequently all superstructure peaks located at $p/23$, where p is an even integer, are systematically absent. An early STM image of the graphene supercell is shown in Figure 3.2 [5]. These subcells have hill structure and are an important subject of discussion in the following sections.

A very simple simulation of the 25-on-23 reconstruction data yielded fairly robust parameters for the maximum corrugation amplitude in the top layer of Ru of 0.2 Å, and an exponential decay constant of this corrugation into the Ru-bulk crystal of 3.4 atomic layers. The graphene corrugation amplitude and the minimum graphene-Ru distance were fixed values determined by early DFT calculations [1]. Despite the simplicity of the model where quantitative agreement was achieved, the authors recognized that the model required full structural fitting including the graphene corrugation and the graphene-Ru distance parameters [5]. Subsequently, a more

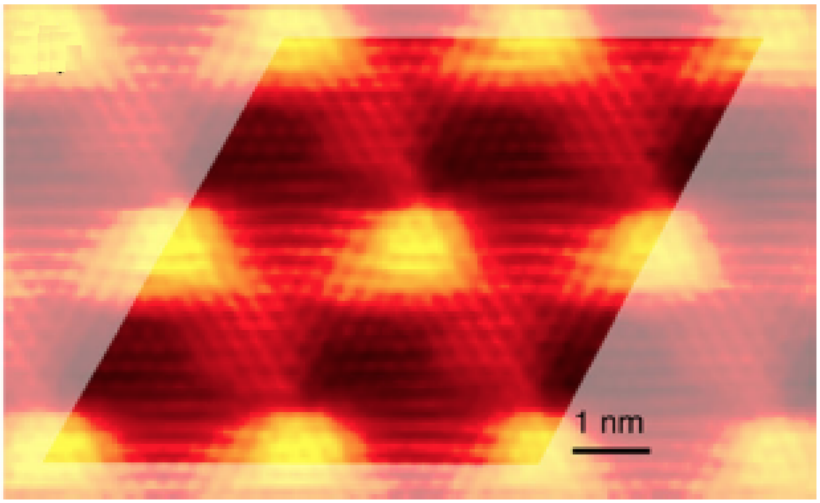

Figure 3.2: An STM image of graphene on Ru(0001), highlighting the supercell containing four subcells. Reprinted figure with permission from [5]. Copyright 2008 by the American Physical Society.

complete structure fitting to the SXRD data was performed [11]. The fitting model was based on parameterization of the atomic coordinates by describing them in terms of a 2D Fourier series expansion. Only the even (second and fourth) Fourier components were considered, as the structure contains 2×2 corrugation periods. The Ru layers mirrored the corrugation of the graphene, and their corrugation amplitude was allowed to damp exponentially. The shortest graphene-Ru distance was fixed to a value determined by DFT calculations [1]. The full structure fitting yielded the graphene and the first layer of ruthenium corrugations amplitudes of 0.82 Å and 0.24 Å respectively. The physical validity of the model was tested by calculating the graphene layer elastic (Keating) energy. The best model was allowed to adopt a $p3$ symmetry where the elastic energy per supercell was 9.4 eV. In contrast, the model based on the same Fourier expansion parametrization but limited to the $p3m1$ symmetry produced higher values. Relaxation to allow $p3$ symmetry favored a twisting motion of carbon atoms on the hills of the corrugation. The in-plane movements up to 0.25 Å were observed at the steepest flanks of the hills. Such arrangement of carbon atoms emerged naturally and led formation of chiral domains [11]. It is important to mention that presented chiral enantiomers should be rotated clockwise and counterclockwise. Since the Ru(0001) surface may have the two possible terminations of the *hcp* stacking, an average signal over the four possible configurations of enantiomer and termination is observed. Taking into account the large SXRD beam size across the sample surface and the consequent signal averaging effect, it is not possible to observe chirality in the

symmetry of the diffraction peak intensities. Measurements of high-spatial-resolution diffraction intensities made with the low-energy electron microscopy (LEED) and the micro-LEED (μLEED) showed no evidence of chirality [12]. Unlike to SXRD, the μLEED allowed to resolve signal spatially from a single configuration of chiral enantiomer and surface termination. The corresponding diffraction information was acquired from the sample region with a diameter of 250 nm within a single surface termination. From the μLEED it was observed that the entire ensemble of the graphene satellite diffraction spots is rotated around Ru each diffraction spot. It was concluded that the small-angle graphene lattice rotation occurs which is the assumed reason for energy minimization.

A quantitative structural evaluation on g/Ru using Fourier-series expanded displacement fields by LEED originally was performed by Moritz *et al.* [13], from which a graphene corrugation height of 1.5 Å was reported. In contrast to the LEED and SXRD studies, helium-atom scattering techniques applied to this system found a substantially smaller corrugation amplitude for graphene of only 0.15 Å [14]. First-principles calculations predicted the graphene corrugation in the range 1.5-1.7 Å [1, 15, 16]. In these calculations, the effect of dispersive forces between the graphene overlayer and the Ru substrate was not included. This issue will be addressed in the following section.

3.2 Density functional theory calculations on graphene/Ru(0001)

Density functional theory (DFT) calculations are numerical quantum mechanical modeling methods of many-body systems. DFT calculations on graphene on metal substrates are a challenging task because they handle a large structure with consequently large computational demands. In addition, the description for dispersive forces and charge-transfer processes causes difficulties in using DFT, as is the case for modeling a carbon overlayer interaction with an underlying Ru-substrate [17, 18]. The major problem lies in describing the van der Waals interaction between the graphene overlayer and a metal substrate. These issues may adversely affect the accuracy of the graphene peak-to-peak corrugation value and the graphene-substrate minimum distance. For instance, the graphene corrugation reduces by 25 % with respect to DFT calculations without van der Waals interaction corrections [18]. Thus, although DFT is likely to generate a model that is close to reality, detailed atomic positions on a sub-Angstrom- or picometer-scale are precluded.

Following the SXRD studies of Martoccia *et al.*, in which the 25×25 graphene reconstruction was discovered, Iannuzzi *et al.* performed a large-scale DFT optimization on 25-on-23 g/Ru down to a depth of six Ru layers. The DFT results revealed an intriguing topography of the graphene layer (Figure 3.4): Four inequivalent subunits emerge, comprised of four hill structures which were coined "moirons" [19]. Three of these (labeled Ω because of their motif) are symmetrically equivalent through 120° rotations, but the fourth (labeled *Y*) has a quite distinct structure, in which the four highest C-atoms form a Y-structure. The heights of these hills are essentially identical and have a peak-to-peak corrugation height of 1.16 Å. The structure has four areas in (*fcc*, *hcp*) registry where the C-Ru interaction strength is different (Figure 3.3). When C pairs occupy (top, *fcc*) and (top, *hcp*) sites the graphene layer is close to the Ru substrate and C-C bonds are stretched. In such a configuration, analysis of the electronic structure showed that the effective chemical bonding takes place via hybridization between the π-orbitals of graphene and the *d*-band of the Ru substrate. There is a significant charge transfer into the carbon anti-bonding p_z orbitals, which thus favors the observed local expansion (i.e., a weakening of the σ in-plane bonds) of the graphene lattice. On the other hand, if the registry is (*fcc*, *hcp*), the interactions are much weaker and dominated by the weak dispersive van der Waals forces, which permit out-of-plane strain relaxation, leading to the formation of protrusions (hills). It is unsurprising that the underlying metal substrate layers are also corrugated by this periodic variation in graphene-ruthenium bonding strength, as shown in Figure 3.4(b). The graphene superstructure imposes vertical strain fields in the substrate and promotes the substrate layer buckling. The ruthenium layer peak-to-peak corrugation amplitude decays from 0.17 Å in the top layer to 0.03 Å in the lowest layer allowed to vary from the bulk structure. The graphene strain (Keating) energy of this model was calculated to be 6.5 eV, significantly lower than that obtained from the model of Martoccia *et al.* of 9.3 eV [11].

Other DFT optimizations performed on simpler 12-on-11, 11-on-10 and 13-on-12 models also indicate the presence of distinct *Y*-Ω hill structures (see Figure 3.5). The 12-on-11 and 11-on-10 favour *Y*-hills, while the 13-on-12 has an Ω-hill. The 12-on-11 model turned out to be more stable in terms of adsorption energy per C atom. The 25-on-23 model cannot be reproduced as a 2×2 replica of the 12-on-11 model.

An important feature to the emerging model from the 25-on-23 DFT calculations is that the initial $p3m1$ symmetry of the structure of the starting model was preserved with high fidelity, although this constrain was not imposed in the DFT optimization. Surprisingly the

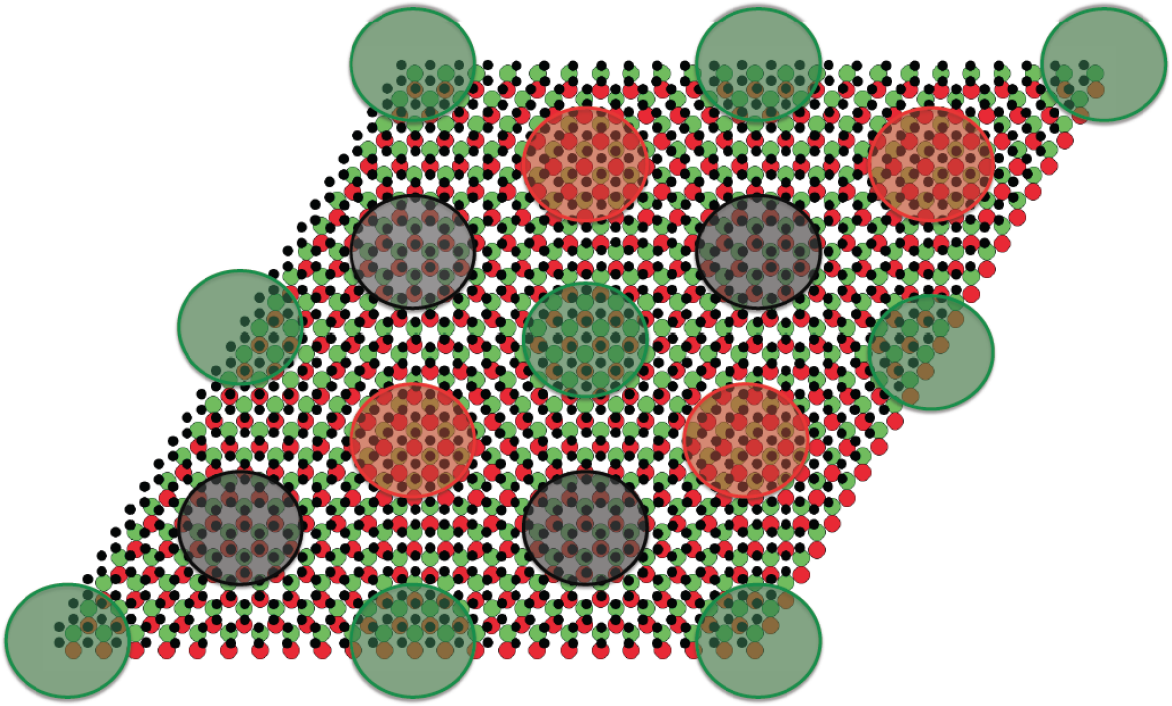

Figure 3.3: Graphene (black) on ruthenium (red - first layer, green - second layer). Three different registries are highlighted: the red is the (fcc, hcp) region, the shaded gray is the (top, hcp), and the green is the (top, fcc).

small superstructures break $p3$ symmetry in addition to the mirror symmetry. For that reason different domains have to be incoherently added for the total structure factor calculation in the SXRD simulation.

In the following, it is shown that the finding from the DFT optimization are in line with experimental observations using SXRD and STM. The structure of the 25-on-23 DFT optimized model therefore represents a promising *ansatz* for the structure evaluation and refinement procedure from SXRD data.

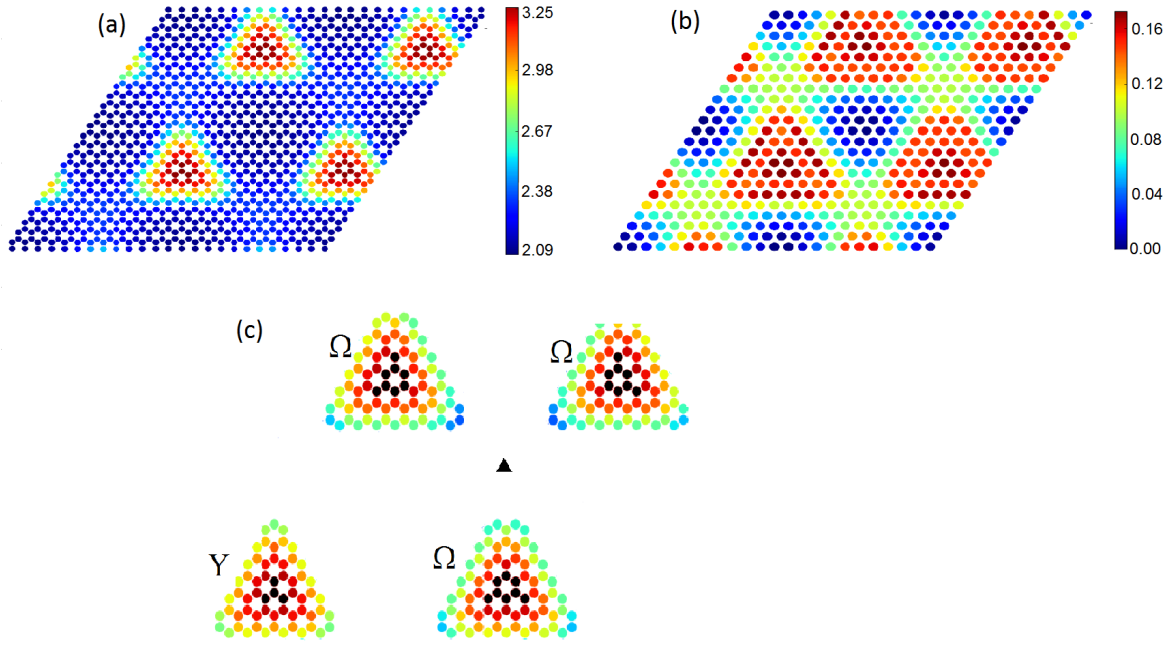

Figure 3.4: The DFT optimized structure of 25 × 25 carbon unit cells on 23 × 23 unit cells of Ru. The height modulation is indicated by the color range from blue (low) to red (high) (a) Map of the 25 × 25 graphene superstructure. The height of the C-atoms over the average of the topmost Ru-layer vary from about 2.09 Å (blue) to 3.25 Å (red). This implies a corrugation height of 1.16 Å. (b) Corresponding map of the first Ru layer. (c) Details of the four hills in the unit cell of the superstructure - one Y and three Ω hills are highlighted. A triangle inset indicates the threefold rotation axis.

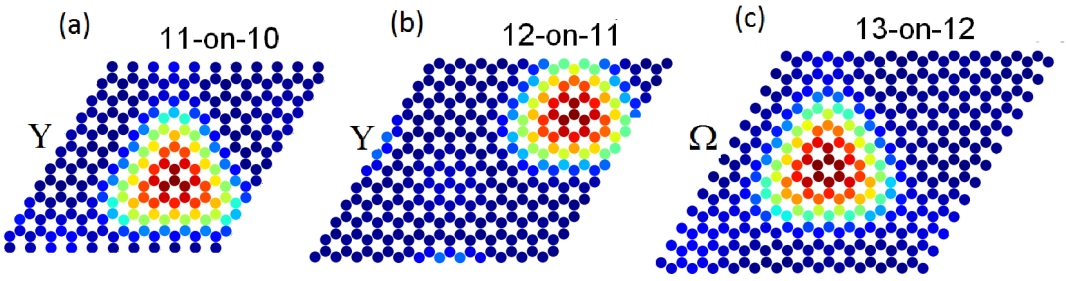

Figure 3.5: The DFT optimized structures of graphene on Ru(0001) for smaller 1×1 hill superstructures. The height modulation is given by the color code from blue (low) to red (high) (a) An 11-on-10 structure with Y-hill. (b) 12-on-11 structure with Y-hill. (c) 13-on-12 structure with Ω-hill.

3.3 Scanning Tunneling Microscopy on graphene/Ru(0001)

As mentioned above, the STM data support the DFT predictions regarding the distinct hill structures seen in the 25×25 graphene supercell. In this section, the detailed findings from large-area scanning tunneling microscopy are briefly presented and discussed. These STM studies were performed by L. Zhou and G. Zhang from the Intitute of Physics, Beijing with collaboration of T. Greber, University of Zürich.

Figure 3.6 shows the atomically-resolved STM topography of g/Ru, covering an area across several protrusions (hills). A more detailed inspection of these protrusions confirms the presence of distinct Y- and Ω-coordinated hills. Two-dimensional Gaussian fitting to the STM topographs was implemented to determine the peak position of a hill. The centre of gravity of the hill enclosed by a disc with a radius of 1.7 Å centered at the peak-position was calculated. Subsequent analysis of the data from 10 hills reveals that STM is capable of discriminating between two types of hills, with different shifts of their centers of gravity compared to the the Gaussian fit. For the Y-hills, there is no or only a small shift, while a significant shift is observed for the Ω-hills [Figure 3.6(b)]. These finding are in perfect agreement with the DFT model. The detailed magnified images for the Y- and Ω-hills are shown in Figures 3.6(c) and (d).

It is important to mention that the entire carbon lattice can be rotated away from the substrate high-symmetry directions. For instance, previous STM studies indicated the graphene lattice rotation of 0.5 ± 0.05^{o} [14]. Also the entire moiré pattern is rotated by 5 ± 0.5^{o} with respect to the Ru substrate. In the work discussed in this setion, on the same preparation, it was observed that there are regions where the carbon lattice rotation occurs by 5 degrees with respect to the hills, but there are also regions without a rotation center, with in-line registry, consistent with the 25-on-23 DFT model.

In conclusion, STM data have confirmed the physical validity of the findings from the DFT optimized model that the g/Ru 25-on-23 structure contains two differently coordinated hill species. It is noted, however, that the graphene superstructure can adapt sensitively to the preparation conditions and the epitaxial growth conditions are not fully controllable. This is reflected in the fact that the carbon lattice can exhibit either rotated or non-rotated domains with respect to the underlying ruthenium substrate. Lithium-atom adsorption tests simulated by DFT calculations have indicated that there is little or no selective adsorption behaviour

between Y- and Ω-hill. In other words, their adsorption energy differences are so small (in the meV range) that the two types of hills are not chemically distinguishable, and that therefore one would not expect selective adsorption for larger atomic clusters and molecules, due to their sizes.

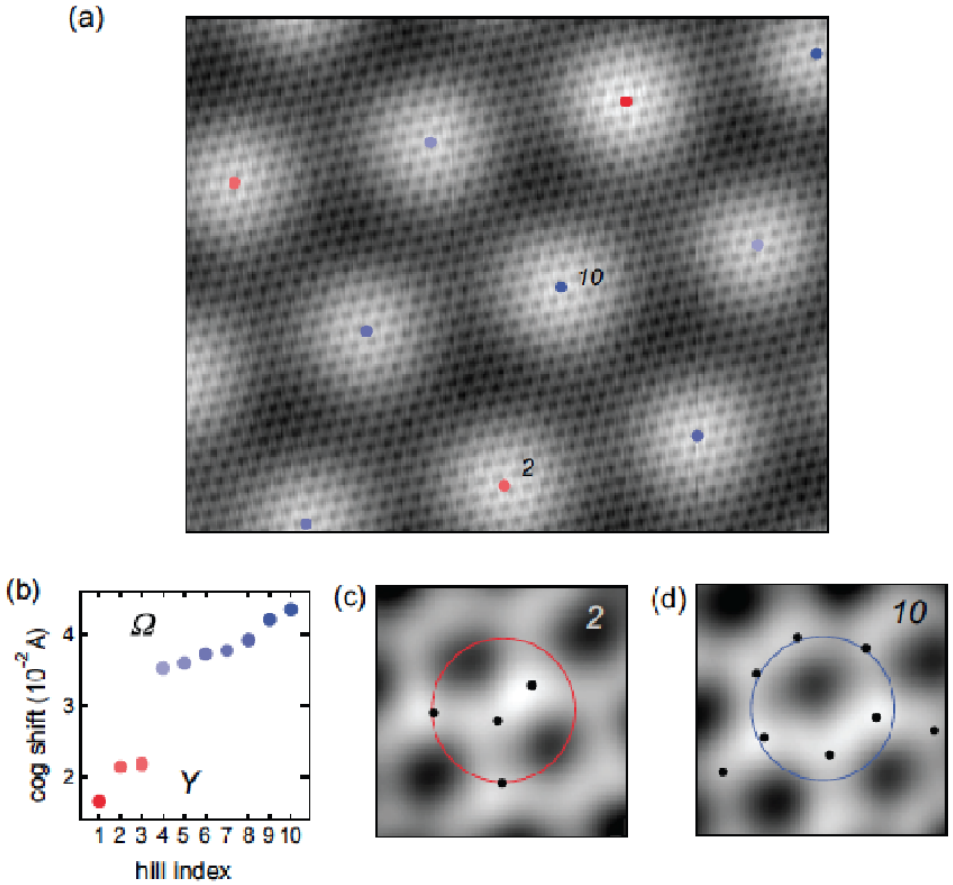

Figure 3.6: Scanning tunneling microscopy data. (a) A large-area image of monolayer graphene on Ru(0001). The apparent corrugation is about 0.6 Å and the average height is set to zero. The center positions of the hills are marked blue and red, indicating respectively large and small shifts of the center of gravity (COG). The COGs are determined within 3.4-Å disks on the centers of the hills, and their shifts are the deviations from those centers. (b) Shifts of the COG. Two distinct groups Y and Ω can be distinguished. (c) and (d) Smoothed zoom-ins of the two hill types. The red and the blue rings are the perimeters of the disks used for the COG determinations. Hill 2 is a representative quasitetrahedral Y arrangement of the four topmost carbon atoms (dots), while Hill 10 is the Ω-arrangement of the eight topmost carbon atoms (dots). Reprinted figures with permission from [20]. Copyright 2013 by the American Physical Society.

3.4 SXRD simulation of the DFT model on graphene/Ru(0001)

As mentioned above, the DFT method lacks a complete description of the graphene–ruthenium interactions. Therefore, the DFT structure of graphene on Ru(0001) may deviate from reality by an unknown degree. In order to evaluate the validity of the optimized DFT model and investigate how close its atomic structure is to physical reality, SXRD simulations on it were performed and compared to the experimental data. To this end, more diffraction data were extracted from the beamtime on graphene/Ru(0001) described in [5, 11] and the original data reanalyzed in order to obtain a larger set of reliable structure factors. Figure 3.7 shows schematically which parts of reciprocal space were recorded and analyzed. Independent extraction of the SXRD data and comparison of symmetry-equivalent data provided a confidence level for the structure factors of better than 5 %.

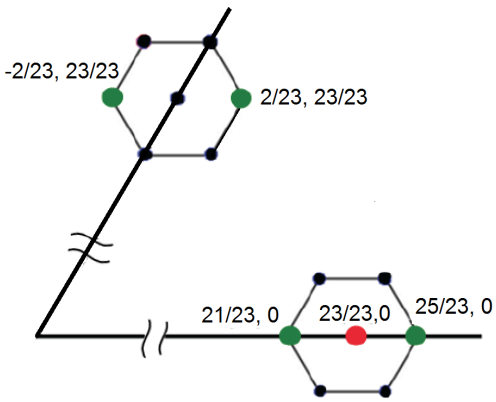

Figure 3.7: Recorded SXRD data, including four superstructure rods (green) and one crystal truncation rod (red).

SXRD simulations were performed using the genetic-algorithm GenX program [21] and the atomic coordinates were imported from the DFT optimized slab. Since the 25-on-23 model preserves $p3m1$ symmetry where the mirror symmetry is maintained, two domains have to be added incoherently, as the domain symmetry is rotated by 180° when one passes from one terrace of the Ru-substrate to another, which is only one atomic layer, i.e., half a unit cell lower or higher. Thus the total structure factor is given by

$$|F_{tot}| = |F_{h,k,l}|^2 + |F_{-h,-k,l}|^2. \tag{3.1}$$

For the Debye-Waller-factor (DWF) parameters, one global value from [9] was used:

$$\text{DWF} \quad = \quad \exp(-q^2\langle u^2\rangle/3), \tag{3.2}$$

where q is the corresponding scattering vector and $\langle u^2\rangle$ the mean squared displacement with a value of 0.0191 Å^2 [9]. The effect of setting the same DWF parameters for C and Ru has only secondary effects on the outcome.

A goodness of fit used for the comparison of the model with the data is defined as:

$$R \quad = \quad \frac{\Sigma_i|\log(Y_i) - \log(S_i)|}{(N-1)}, \tag{3.3}$$

where Y_i are the experimental scattering intensities, S_i corresponding simulated data, and N is the number of data points.

Four simulated superstructure rods (SSR) and one crystal truncation rod (CTR) are shown in Figure 3.8 (blue solid lines). Here only a single global intensity scaling factor was fitted. The simulated rods are fairly consistent with the experiment. From the experimental data it was concluded that the signal-intensity modulation indicates that the ruthenium layers are physically corrugated [5] down to a significant depth. Moreover, extrapolation of the $(21/23, 0)$-rod intensity to l=0 indicated that it has nonzero intensity, which is proof of in-plane movements of the atoms within the supercell. These important characteristics appear to be in a good agreement with the DFT optimized model. The model has a goodness of fit (R-factor) of 12.6 %. The earlier structural model of Martoccia *et al.,* based on an *ansatz* with Fourier-series expanded displacement fields, produced a best R-factor of 14.3 % after extensive fitting using 21 parameters [11].

In order to make a meaningful comparison of the goodnesses of fit, the R-factor of Martoccias's optimized structure was recalculated using the newer and more complete experimental data, fitting only with a global intensity scaling factor. The calculated R-factor is 18.6 %, significantly higher than that associated with the unmodified DFT model. The corresponding superstructure rods are shown for comparison in Figure 3.8 (red solid lines). A consistent feature of the DFT-simulations in Figure 3.8 is that the width of the features are larger than those of the experimental data. This indicates that, while by far the largest DFT model reported in the literature to date, the six layers of Ru considered are still insufficient to fully describe the decay of corrugation in the substrate. It remains a moot point whether DFT calculations to

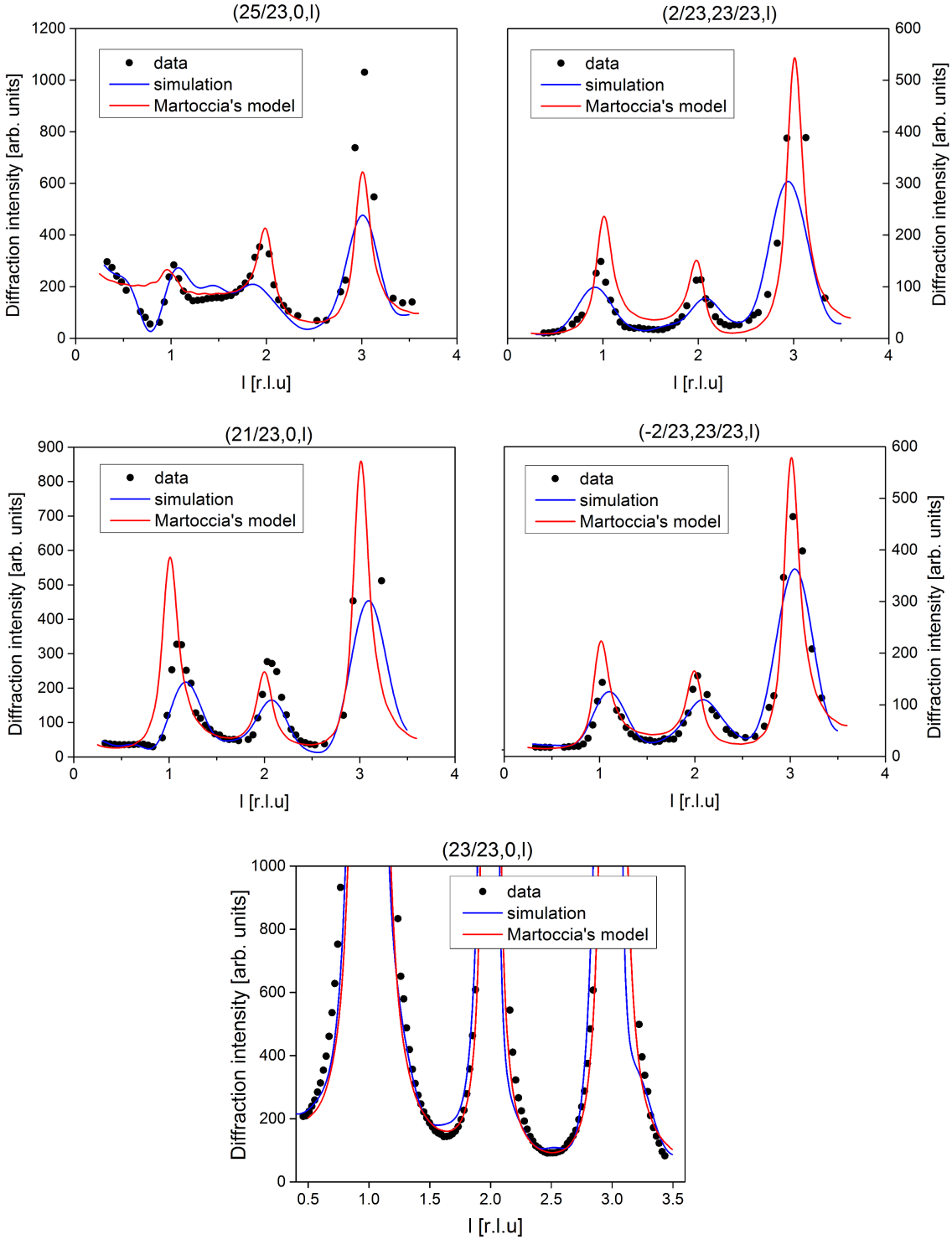

Figure 3.8: Measured SSR data (black dots) in comparison to the results obtained from SXRD simulations (blue solid lines) and the model developed by Martoccia *et al.* [11].

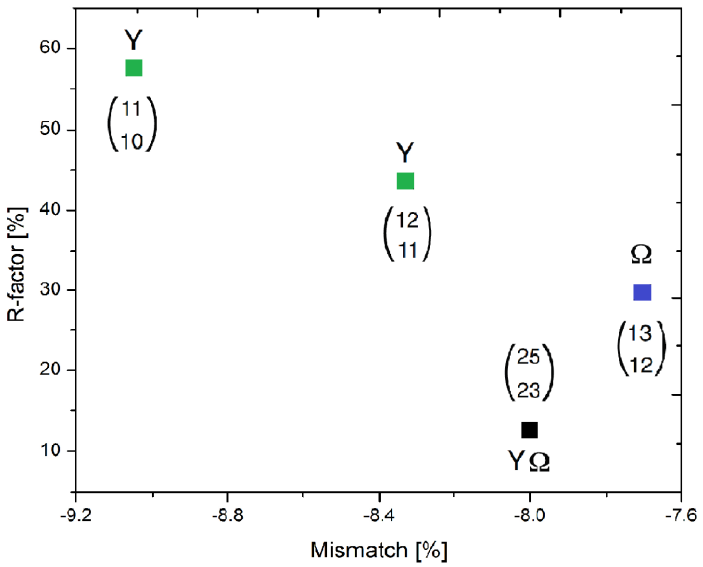

Figure 3.9: R-factors of different DFT models versus mismatch between the graphene and the substrate [20].

still greater substrate depths makes any physical sense, however.

R-factor calculations for the small DFT superstructures with 4 layers of ruthenium shown in Figure 3.5 were also performed and the result is plotted in Figure 3.9. Compared to 25-on-23 model, the R-factor values are significantly higher.

It is essential to assess the DFT optimized model taking the structural parameters including the adsorption energy, the distortion energy and the Keating energy. The adsorption energy is the total energy of the g/Ru model minus the energies of free- standing graphene and of the Ru substrate. The distortion energy is calculated as the the total energy difference between the free- standing graphene lattice and the free-standing graphene superstructure lattice obtained from the DFT optimization. As mentioned previously, the Keating energy is the elastic energy stored in the graphene lattice. All of these structural parameters evaluated for different DFT models are summarized in Figure 3.10

unit cell	Ru layers	corrugation (Å)	hill type	distortion energy (meV/C)	adsorption energy (eV/C)	Keating energy (meV/C)
11 on 10	4	1.27	Y	13	0.21	7.3
12 on 11	4	1.17	Y	17	0.22	5.9
25 on 23	4	1.17	$1Y$ and 3Ω	22	0.24	5.5
13 on 12	4	1.11	Ω	30	0.23	7.6
25 on 23	6	1.16	$1Y$ and 3Ω	21	0.24	5.2

Figure 3.10: The Structural parameters of different unit cells of g/Ru(0001) system obtained from DFT optimization. Reprinted figure with permission from [20]. Copyright 2013 by the American Physical Society.

3.5 SXRD refinement of the DFT model on graphene/Ru(0001)

In this section, we focus on the structural refinement procedure adopted to improve upon the 25-on-23 DFT model to better fit the experimental data. A parameterized modification method for the DFT structure was introduced and applied to fit the model to experiment. The ultimate goal was to evaluate the model quantitatively using the SXRD experimental data.

In general, the number of parameters involved in the fitting model can be large. This is especially true if the positions and Debye-Waller factors of individual atoms are handled separately. Besides the hugely time-consuming calculations, the model would be massively overfit and would inevitably be trapped in local minima. In the case of the (25×25)C/(23×23)Ru superstructure, it is thus quite impossible to fit individual atomic positions because of the very large numbers of atoms involved. Therefore, the only reasonable approach is to adopt a rational parameterization of the entire structure which links the individual atomic coordinates in a physically reasonable manner. Thus the initial effort was to find an appropriate parameterization approach which will reduce the number of parameters (i.e., limit the parameter space) to a reasonable value and produce a reasonable output. Once the model is parameterized, the final effort is to fit it to the experimental dataset and find the *global minimum*. The output from the best fit provides quantitative information revealing structural details such as interplanar distance, buckling, vertical displacement of atomic layers, etc.

Since the starting model for refinement is the optimized DFT structure, there need be fewer fitting parameters than in the model of Martoccia *et al.*, in which 21 parameters were involved [11]. Nonetheless, even with the initial DFT model, which we can assume to be close to physical reality, it is not immediately straightforward to define an appropriate parameterization strategy without making certain assumptions. In the following, the out-of-plane and in-plane displacements of the atomic coordinates are adjusted between a flat layer of perfect graphene plus a bulk-like ruthenium substrate, and the corrugated DFT model, using a single parameter w. Mathematically, for each graphene atom, the coordinates are defined by

$$\begin{aligned} x &= x_{\text{flat}} + (x_{\text{DFT}} - x_{\text{flat}})\omega, \\ y &= y_{\text{flat}} + (y_{\text{DFT}} - y_{\text{flat}})\omega, \\ z &= z_{\text{flat}} + (z_{\text{DFT}} - z_{\text{flat}})\omega, \end{aligned} \tag{3.4}$$

where ω is a linear strain parameter. ω=1 thus corresponds to the DFT coordinates and w=0 to flat graphene. The same approach is also applied to all the ruthenium substrate layers. A further simplification was made, whereby a common w factor was used for both graphene and ruthenium, as it was assumed that the strain in the graphene is proportional to the strain in the substrate. In addition to the linear strain parameter, a parameter D was applied, which varies the C-Ru bond distance by shifting the entire graphene layer in the out-of-plane direction from its initial position. Thus, apart from global scaling parameters, only two structure refinement parameters were needed for the full refinement scenario.

Fitting the model to the experimental data was performed by the genetic-algorithm optimization program GenX [21]. First, we fit the Ru topmost layer vertical position relative to the underlying Ru-layers using the CTR data alone, as this is mostly sensitive to small changes in the interplanar spacing of the topmost two Ru-atomic layers and almost entirely insensitive to the graphene structure. The CTR fit yielded an interplanar distance of 2.089 Å, which should be compared to a bulk value of 2.141 Å, and agrees excellently with the work of Baddorf *et al.* [22]. Subsequently the complete structure optimization was carried out several times to check for reliability. The best fit obtained has an R-factor of 12.2 %. The resulting value of $\omega = 1.07$ implies a graphene corrugation amplitude of 1.24 Å, while that of the top Ru-layer is 0.19 Å. The graphene layer is shifted towards the Ru substrate by 0.11 Å, and the average C-Ru vertical distance is 2.282 Å. The fits of the four superstructure rods and the CTR are shown in Figure 3.11.

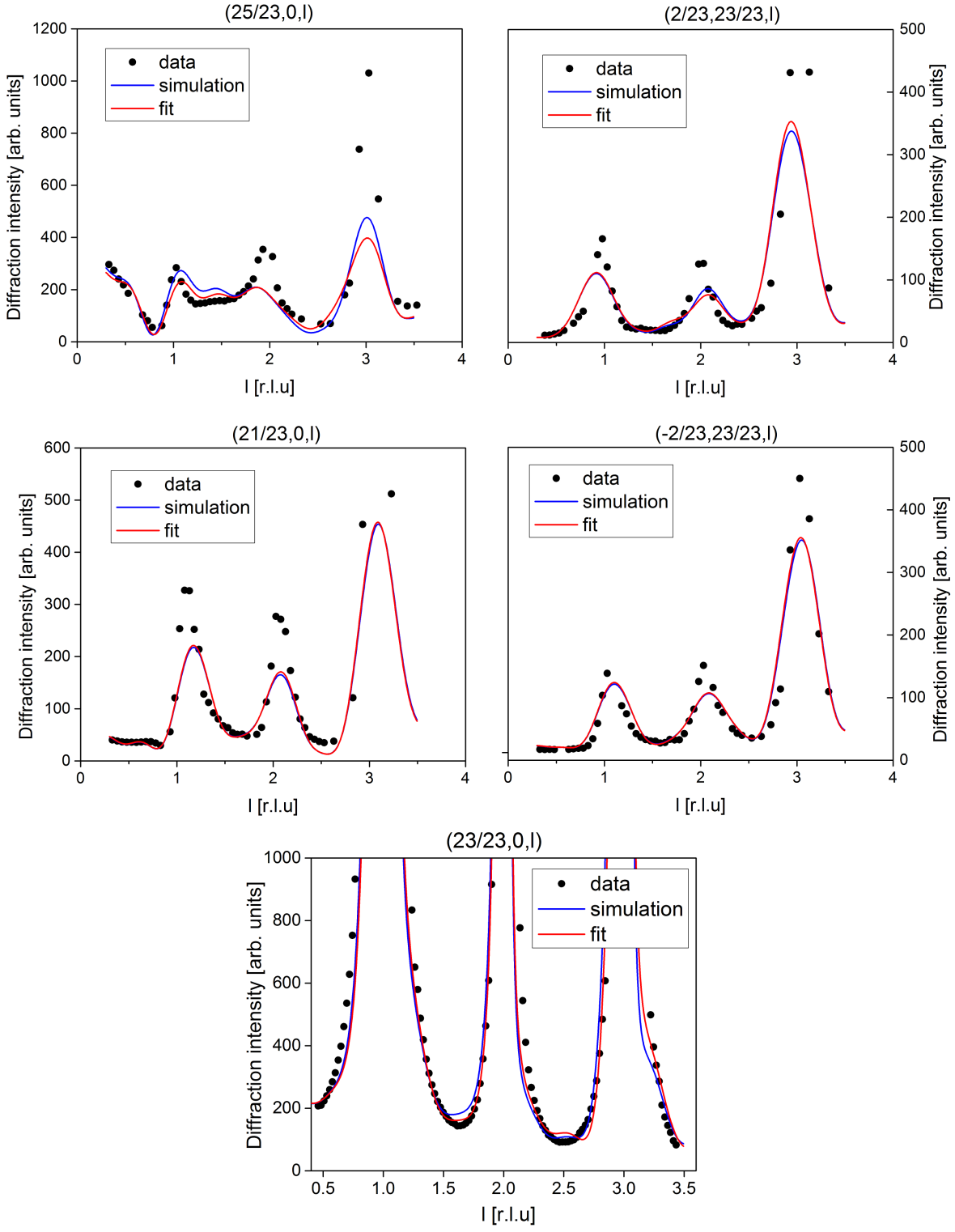

Figure 3.11: Comparison of four superstructure rods and the CTR obtained from the original DFT structure (blue solid line), after fitting this model (red solid lines), and the experimental data (black dots).

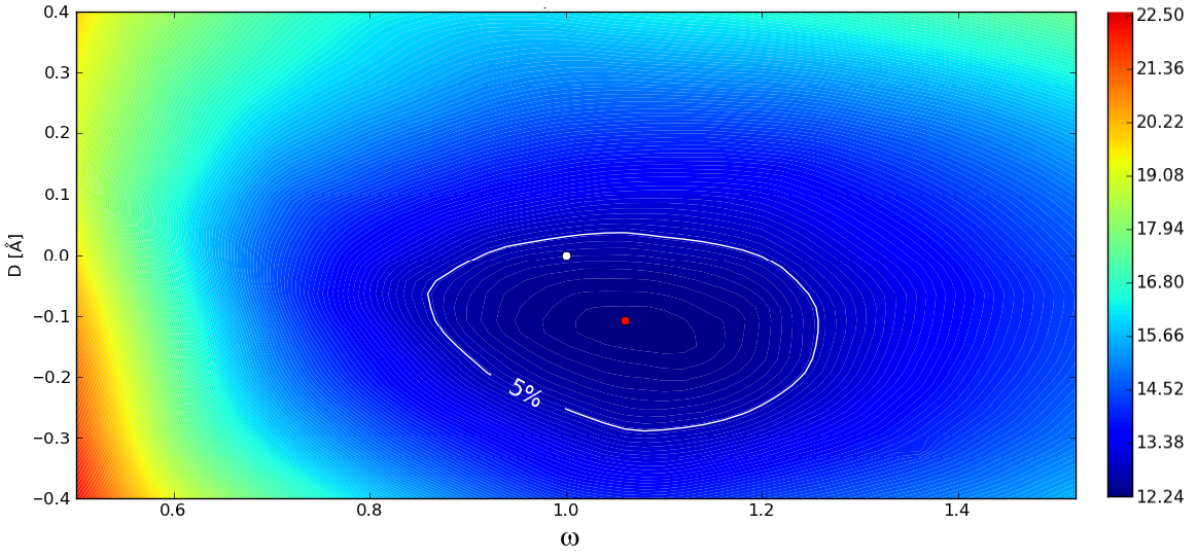

Figure 3.12: Two-parameter R-factor map for the fit parameters D and ω. The blue valley corresponds to lower values of R-factor, red to higher values. The red dot indicates the R-factor minimum. The white dot indicates the R-factor obtained directly from the DFT model without refinement.

In order to demonstrate the sensitivity of the fitting parameters to the SXRD data, a two-dimensional R-factor map was generated, shown in Figure 3.12. The R-factor minimum (red dot) is located very close to the R-factor (white dot) obtained directly from the DFT model without refinement.

From the R-factor landscape it is clear that SXRD is more sensitive to D than to ω. To check the validity of the model refinement with D and ω parameters, we introduced R-factor confidence interval which is 5 % of its present value. In other words, the 1.05 R_{min} contour line is considered to be a acceptable range for parameters that are consistent with the SXRD data. The R-factor of the DFT model lies in this confidence interval. Therefore, from the structure refinement we concluded that the DFT model of the 25-on-23 structure agrees with the SXRD experiment.

3.6 Probing the SXRD data sensitivity to the graphene structure

X-ray scattering amplitudes are proportional to the electron density, which in turn is related to the atomic number Z, while the diffraction signal scales with the square of the amplitude. Z for carbon (6) is significantly lower than that for Ru (44). Because each two-atom graphene unit cell is $(23/25)^2$ times smaller in area than the one-atom atomic unit cells of Ru, the electron density of graphene is approximately $(25/23)^2 \times 2 \times 6/44 \approx 0.32$ that of each Ru-layer. In addition, several Ru-layers deviate from bulk coordinates and thus contribute to the SSR signal. Hence it is obvious that the relative graphene-layer contribution to the total diffraction signal will be weak, while it can be expected that the Ru substrate corrugation will strongly affect the R-factor when varying ω in the fitting routine. This is reflected by the relatively long valley in the direction parallel to the ω-axis in Figure 3.12.

To elucidate the impact of the graphene corrugation on the SSR signal, they were simulated for different values of graphene corrugation. The corresponding result is shown in Figure 3.13. Unsurprisingly, the most graphene-sensitive rod is the $(25/23, 0)$-rod, as it corresponds to the primary Bragg rod of the carbon lattice. Certain l-ranges appear to be particularly affected. The other three SSRs are far less sensitive to graphene, but remain strongly sensitive to the Ru-substrate structure. To understand how the ω parameter affects the R-factor quantitatively, the ω parameter for the graphene corrugation alone was allowed to vary. Subsequently the variation of the R-factor was also generated for the Ru-substrate alone. Figure 3.14 shows these curves. As is evident from this figure, the graphene R-factor curve is significantly wider than that for Ru.

3.7 Conclusions

In this chapter we have described the structure of graphene on Ru(0001). We applied SXRD to evaluate the physical validity of the DFT optimized model. For that purpose we used a simple parameterization procedure and fit the model to the SXRD data. Tests of changes in the goodness of fit with the parameters acting only on either the graphene layer or on the ruthenium substrate demonstrate on the one hand the robustness of the extracted values for the ruthenium corrugation amplitude and decay depth, and on the other, the relative insensitivity of the SXRD data to the graphene structure. The work presented in this chapter has been

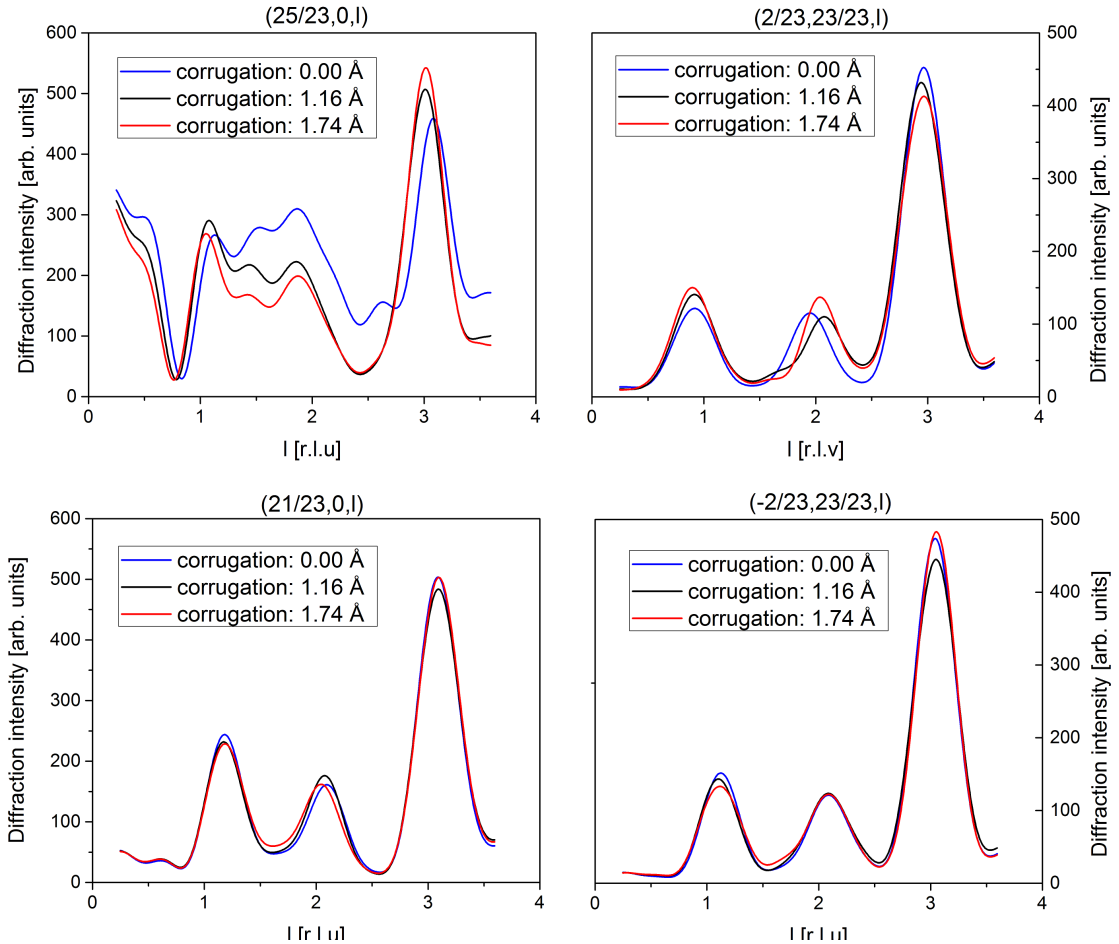

Figure 3.13: Simulated superstructure rods for different graphene-corrugation values.

published in [20].

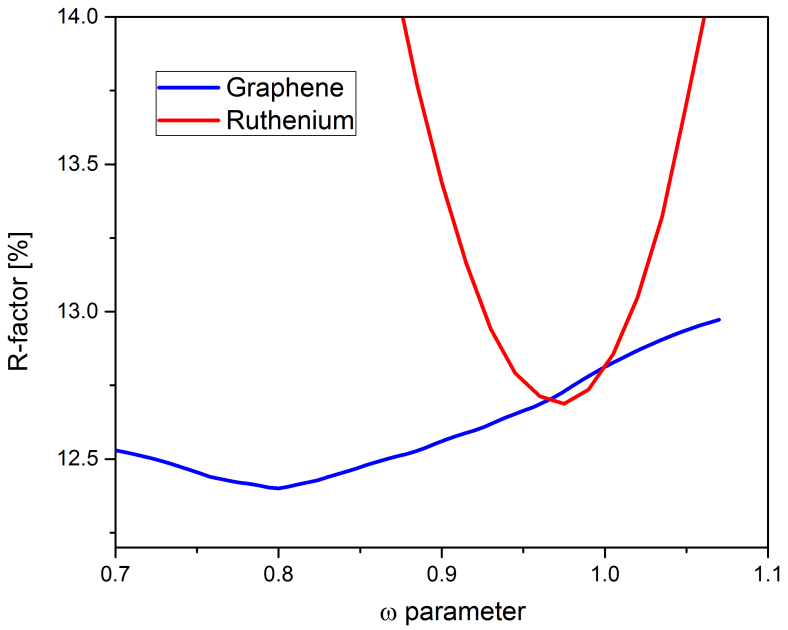

Figure 3.14: The variation of the R-factor on ω only acting on graphene (blue) and ruthenium (red). D is fixed with the value of the DFT model. Note also that while the narrow R-factor minimum for ruthenium lies very close to the DFT model (1.0), that for the graphene curve is at a much lower value and the error margin (i.e., the width of the curve) is correspondingly larger.

Bibliography

[1] B. Wang, M. L. Bocquet, S. Marchini, S. Günther, and J. Wintterlin: "Chemical origin of a graphene moiré overlayer on Ru (0001)." *Phys. Chem. Chem Phys.* **10**(24), 3530–3534 (2008).

[2] P. Yi, S. Dong-Xia, and G. Hong-Jun: "Formation of graphene on Ru (0001) surface." *Chin.Phys. Lett* **16**(11), 3151 (2007).

[3] P. W. Sutter, J.-I. Flege, and E. A. Sutter: "Epitaxial graphene on ruthenium." *Nature Mat.* **7**(5), 406–411 (2008).

[4] A. B. Preobrajenski, M. L. Ng, A. S. Vinogradov, and N. Mårtensson: "Controlling graphene corrugation on lattice-mismatched substrates." *Phys. Rev. B* **78**(7), 073401 (2008).

[5] D. Martoccia, P. R. Willmott, T. Brugger, M. Björck, S. Günther, C. M. Schlepütz, A. Cervellino, S. A. Pauli, B. D. Patterson, S. Marchini, *et al.*: "Graphene on Ru (0001): a 25×25 supercell." *Physical review letters* **101**(12), 126102 (2008).

[6] S. Marchini, S. Günther, and J. Wintterlin: "Scanning tunneling microscopy of graphene on Ru (0001)." *Phy. Rev. B* **76**(7), 075429 (2007).

[7] Y. Pan, H. Zhang, D. Shi, J. Sun, S. Du, F. Liu, and H. J. Gao: "Highly Ordered, Millimeter-Scale, Continuous, Single-Crystalline Graphene Monolayer Formed on Ru (0001)." *Advanced Materials* **21**(27), 2777–2780 (2009).

[8] A. L. V. De Parga, F. Calleja, B. C. G. Borca, M. Passeggi Jr, J. Hinarejos, F. Guinea, and R. Miranda: "Periodically rippled graphene: growth and spatially resolved electronic structure." *Phys. Rev. Lett.* **100**(5), 056807 (2008).

[9] D. Martoccia: *Structural Studies of h-BN and Graphene Single-Layers on Transition- Metal Surfaces*. Ph.D. thesis, Universität Zürich, Zurich (2009).

[10] A. L. V. De Parga, F. Calleja, B. C. G. Borca, M. Passeggi Jr, J. Hinarejos, F. Guinea, and R. Miranda: *Reply Phys. Rev. Lett* **101**, 099704 (2008).

[11] D. Martoccia, M. Björck, C. M. Schlepütz, T. Brugger, S. A. Pauli, B. D. Patterson, T. Greber, and P. R. Willmott: "Graphene on Ru (0001): a corrugated and chiral structure." *New J. Phys.* **12**(4), 043028 (2010).

[12] K. Man and M. Altman: "Small-angle lattice rotations in graphene on Ru (0001)." *Physical Review B* **84**(23), 235415 (2011).

[13] W. Moritz, B. Wang, M. L. Bocquet, T. Brugger, T. Greber, J. Wintterlin, and S. Günther: "Structure determination of the coincidence phase of graphene on Ru (0001)." *Phys. Rev. Lett.* **104**(13), 136102 (2010).

[14] B. Borca, S. Barja, M. Garnica, M. Minniti, A. Politano, J. M. Rodriguez-García, J. J. Hinarejos, D. Farías, A. L. V. de Parga, and R. Miranda: "Electronic and geometric corrugation of periodically rippled, self-nanostructured graphene epitaxially grown on Ru (0001)." *New J. Phys* **12**(9), 093018 (2010).

[15] B. Wang, M. Bocquet, S. Günther, and J. Wintterlin: "Comment on Periodically Rippled Graphene: Growth and Spatially Resolved Electronic Structure." *Physical review letters* **101**(9), 099703 (2008).

[16] D.-e. Jiang, M.-H. Du, and S. Dai: "First principles study of the graphene/Ru (0001) interface." *The Journal of chemical physics* **130**(7), 074705 (2009).

[17] P. A. Khomyakov, G. Giovannetti, P. C. Rusu, G. Brocks, J. Van den Brink, and P. J. Kelly: "First-principles study of the interaction and charge transfer between graphene and metals." *Phys. Rev. B* **79**(19), 195425 (2009).

[18] D. Stradi, S. Barja, C. Díaz, M. Garnica, B. Borca, J. Hinarejos, D. Sánchez-Portal, M. Alcamí, A. Arnau, A. V. de Parga, *et al.*: "Role of dispersion forces in the structure of graphene monolayers on Ru surfaces." *Physical review letters* **106**(18), 186102 (2011).

[19] K. Hermann: "Periodic overlayers and moiré patterns: theoretical studies of geometric properties." *Journal of Physics: Condensed Matter* **24**(31), 314210 (2012).

[20] M. Iannuzzi, I. Kalichava, H. Ma, S. J. Leake, H. Zhou, G. Li, Y. Zhang, O. Bunk, H. Gao, J. Hutter, *et al.*: "Moiré beatings in graphene on Ru (0001)." *Phys. Rev. B* **88**(12), 125433 (2013).

[21] M. Bjorck and G. Andersson: "GenX: an extensible X-ray reflectivity refinement program utilizing differential evolution." *J. Appl. Crystallogr.* **40**(6), 1174–1178 (2007).

[22] A. P. Baddorf, V. Jahns, D. M. Zehner, H. Zajonz, and D. Gibbs: "Relaxation and thermal expansion of Ru (0001) between 300 and 1870 K and the influence of hydrogen." *Surf. Sci.* **498**(1), 74–82 (2002).

Chapter 4

Structural study of boron-nitride nanomesh on PtRh(111)

4.1 Introduction

Single layers of hexagonal boron nitride (h-BN) grown on transition metals have been investigated on various substrates over the past years [1–4]. This chapter addresses surface x-ray diffraction (SXRD) studies on h-BN grown on a PtRh alloy.

The composition of the surface of PtRh alloys may differ from that of the bulk, due to segregation effects, which are known to differ significantly, according to how the surface is treated and/or exposed to adsorbates [5]. Moreover, the surface may also exhibit different chemical order and distinct structural domains can be formed [6]. For PtRh with a bulk composition of 25:75, vertical segregation in the top layers was reported [7]. In the case of the $Pt_{25}Rh_{75}(111)$ surface, the room-temperature Pt-concentration was found to increase with the annealing temperature and became saturated at 900° C with a Pt concentration of 70 %. The scanning tunneling microscopy images with chemical contrast revealed short chains of atoms of the same species [7].

A single layer of h-BN was synthesized for the first time on $Pt_{50}Rh_{50}(111)$ [8]. The h-BN overlayer forms a typical well-ordered nanomesh structure with pores and wires. The preparation consists of thermal decomposition of borazine on the heated substrate. The h-BN/PtRh(111) system was investigated by means of scanning tunneling microscopy (STM),

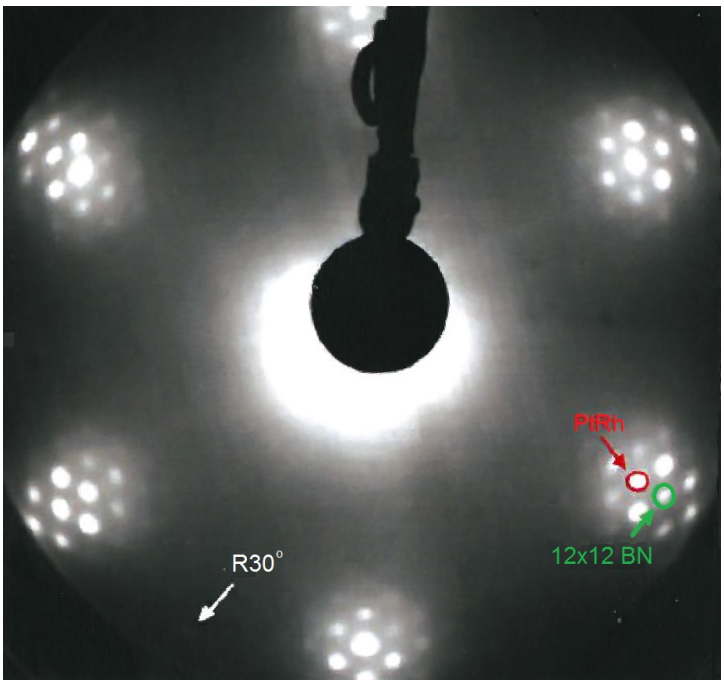

Figure 4.1: LEED pattern of h-BN/PtRh(111). Satellite spots can be clearly seen around the main PtRh-peaks. Courtesy of [8].

photoelectron spectroscopy, and low energy electron diffraction (LEED). From the LEED and STM data it was thought that the reconstruction was (12×12) BN unit cells (u.c.) on (11×11) PtRh u.c., and that the supercell size is 30.02 Å. Results based on X-ray photoelectron spectroscopy and photoelectron diffraction indicated that the substrate composition is changed by the deposition of h-BN, driven by lateral and vertical segregation during the h-BN growth. Figure 4.2(a) shows qualitative visualization of the Rh vertical segregation model. It was also proposed that the h-BN nanomesh induces lateral segregation on the topmost PtRh atomic layer, whereby rhodium atoms gather under the pores and platinum atoms concentrate under the wires, leading to rhodium-island formation [Figure 4.2(b)].

4.2 Surface X-ray diffraction studies on h-BN/PtRh(111)

High-resolution SXRD experiments were performed on h-BN/PtRh(111) in order to precisely measure the superstructure size. SXRD allows the accurate determination of the lattice constants of surface structures with picometer resolution. The experiment was performed at the

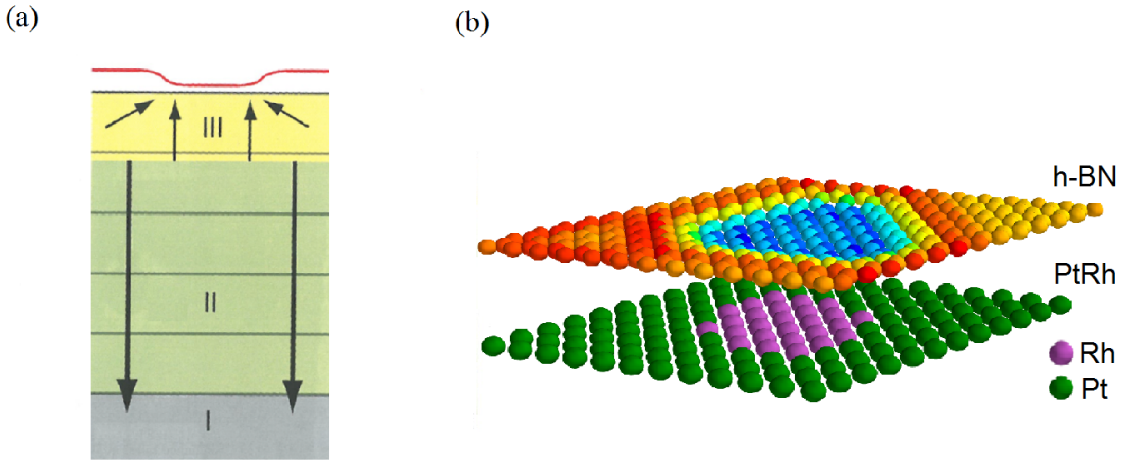

Figure 4.2: Supposed segregation model of h-BN/PtRh(111). (a) The model consisting three major zones: Zone I represents the bulk of the crystal with a ratio 50:50 rhodium:platinum. Zone II describes the layers two to five. A decrease of rhodium concentration is observed because of vertical segregation which descends rhodium atoms towards the bulk. No lateral segregation is observed in this zone. Zone III consists of the top layer. It shows vertical and lateral segregation (Courtesy of [8]). (b) Lateral segregation beneath the top layer of PtRh forming a Rh island.

Materials Science beamline, Swiss Light Source [9]. The samples were prepared *ex-situ* in the ESCA lab at the University of Zürich. Details of the preparation procedures are described in [8]. The resulting superstructure was inspected *in-situ* by LEED (Figure 4.1), which showed clear hexagonally arranged satellite spots around the PtRh Bragg rods, demonstrating a well-ordered superstructure.

Freshly prepared, high-quality samples were transferred to the beamline for SXRD studies under UHV condition (10^{-9} mbar) using the special minichamber equipped with a hemispherical Be-dome (the so-called "baby-chamber"). The photon-beam energy was set to 10 keV. For the acquisition of the superstructure signal, the incident angle was set to 0.39 °, close to the critical angle for total external reflection, in order to obtain enhanced surface sensitivity. The surface coordinate system used was $a = b = a_{\text{bulk}}/\sqrt{2} = 2.729$ Å, and $c = a_{\text{bulk}} \cdot \sqrt{3} = 6.686$ Å. Here $a_{\text{bulk}} = 3.859$ Å is the bulk lattice constant of PtRh 50:50.

A high-resolution in-plane scan along the h-direction is shown in Figure 4.3. In addition to

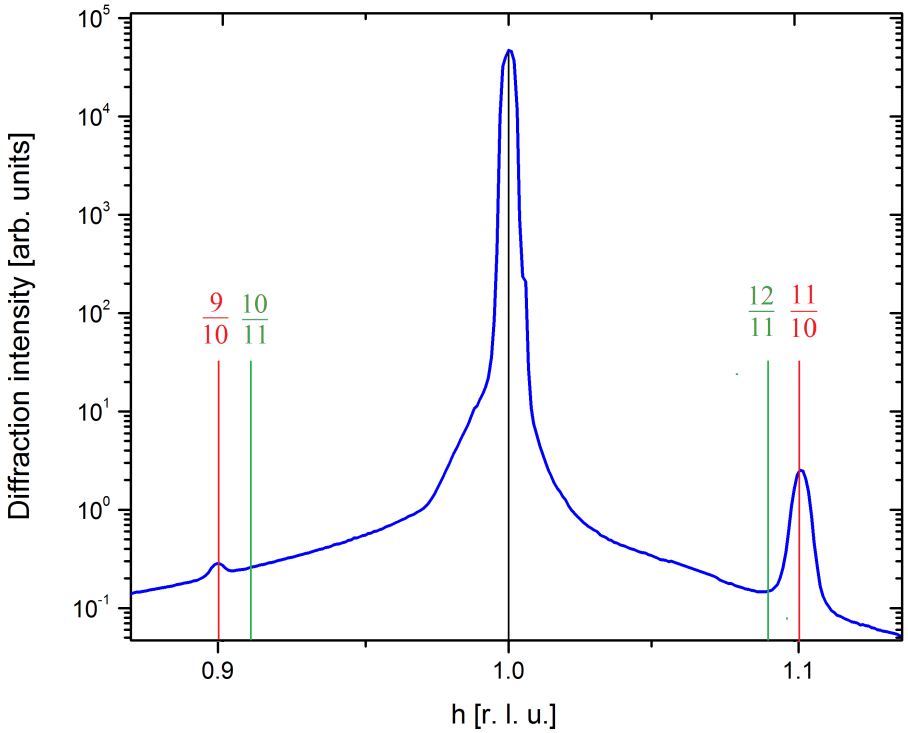

Figure 4.3: In-plane scan along h at $l = 1.2$, $k = 0$. In addition to the Bragg PtRh-peak, the principal h-BN and superstructure peaks are observed. Note that those two peaks are found at 0.900 ± 0.001 and 1.100 ± 0.001 r.l.u., demonstrating conclusively that in fact h-BN/PtRh(111) forms an 11-on-10 structure (red lines). The green lines show where the signal would be seen if the structure were 12-on-11.

the (10)-PtRh Bragg peak, two peaks at the positions (h,k)=(9/10,0) and (h,k)=(11/10,0) are clearly observed. The 11/10 peak corresponds to the Bragg rod of the h-BN lattice, which is thus referred to as the *principal* h-BN signal. This will be seen even if the h-BN does not lock in commensurately to the underlying PtRh. In contrast, the 9/10 peak can only occur if there is a true 11-on-10 superstucture.

Figure 4.4 shows pseudo-Voigt fits to the superstructure data, where the peaks are exactly at the expected positions within the accuracy of our measurements. Both signals have a width of approximately 0.005 r.l.u., indicating from the Scherrer equation that the domains have linear dimensions of at least 200 in-plane unit cells of the underlying substrate (i.e., 54.6 nm) in lateral extent. This accommodates 20×20 superstructure cells and is thus the minimum average lateral dimension in which the superstructure contains no defects.

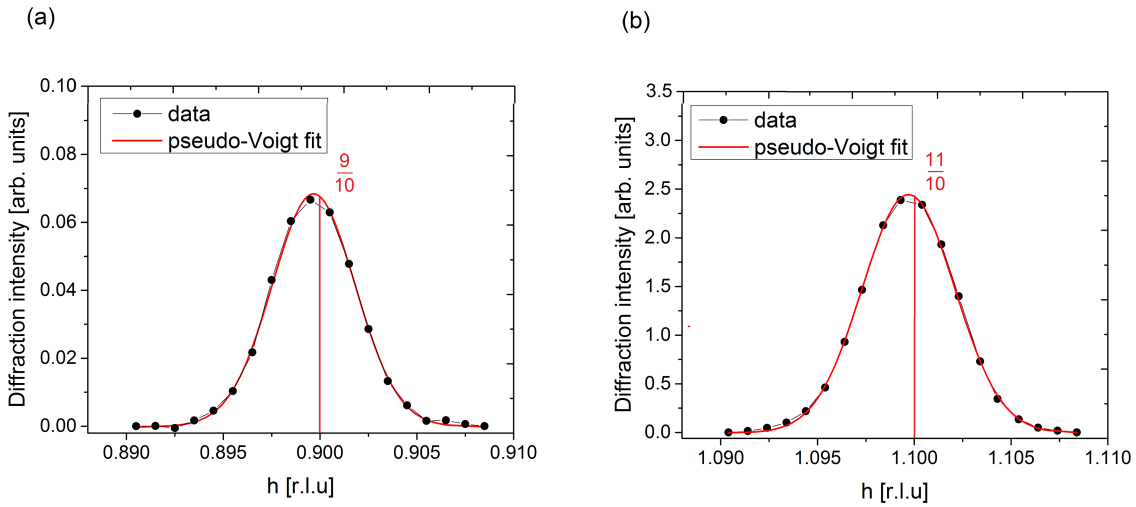

Figure 4.4: The true superstructure peak (a) and the principal h-BN peak (b). The data were fitted using a pseudo-Voigt function.

In Figure 4.3, the positions where 12-on-11 reconstruction signals would lie are also shown, from which it can be seen that this originally proposed superstructure size was incorrect. To conclude, the real reconstruction peak and the principal h-BN peak both unambiguously confirm a commensurate reconstruction with a (11×11) unit cell. The supercell size is found to be 27.29 Å. The SXRD findings thus improve upon previous reports based on STM and LEED studies, because of its unsurpassed resolution.

In addition to the determination of the size of the h-BN superstructure on PtRh 50:50, the influence of the h-BN nanomesh on the near-surface structure of the PtRh(111) was investigated. In Section 4.1, it was stated that the formation of the h-BN nanomesh on PtRh(111) affects the chemical composition down to several atomic layers. Because rhodium ($Z = 45$) has 33 less electrons than platinum ($Z = 78$), any significant change in the composition of the alloy in the near-surface region will be reflected in the electron density profile in the vertical direction. The latter can be probed by SXRD, in particular via the (00l) specular CTR.

With this in mind, CTR data from a bare PtRh(111) substrate and h-BN/PtRh(111) were recorded. The sample thermal cleaning procedure is described in [8]. The recorded data are shown in Figure 4.5. The specular (00l) rod of the bare PtRh(111) substrate exhibits pro-

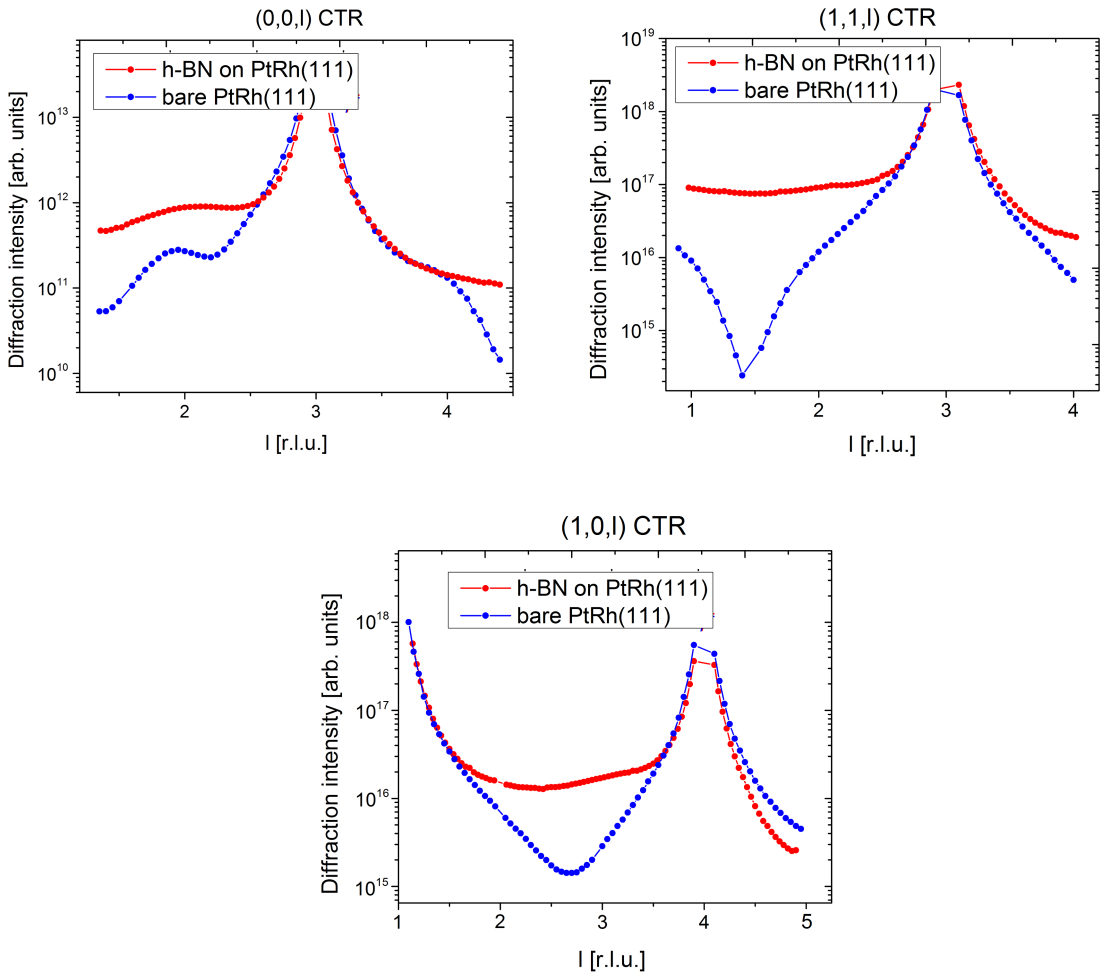

Figure 4.5: Crystal truncation rod data recorded on the bare PtRh(111) and *h*-BN/PtRh(111) samples. The rod intensity variation becomes less pronounced once *h*-BN is deposited, indicating a smoothing of the vertical segregation profile near the surface region.

nounced characteristic oscillations, indicative of significant variations in the vertical electron-density profile, i.e., segregation. The (11l) rod also shows strong interference fringe-like features.

From the periodicity of these oscillatory features, it can be estimated that there is a significant electron-density variation with respect to bulk down to approximately four atomic layers. From the CTR curves, it is seen that *h*-BN "suppresses" the rod intensity variation, that is, the

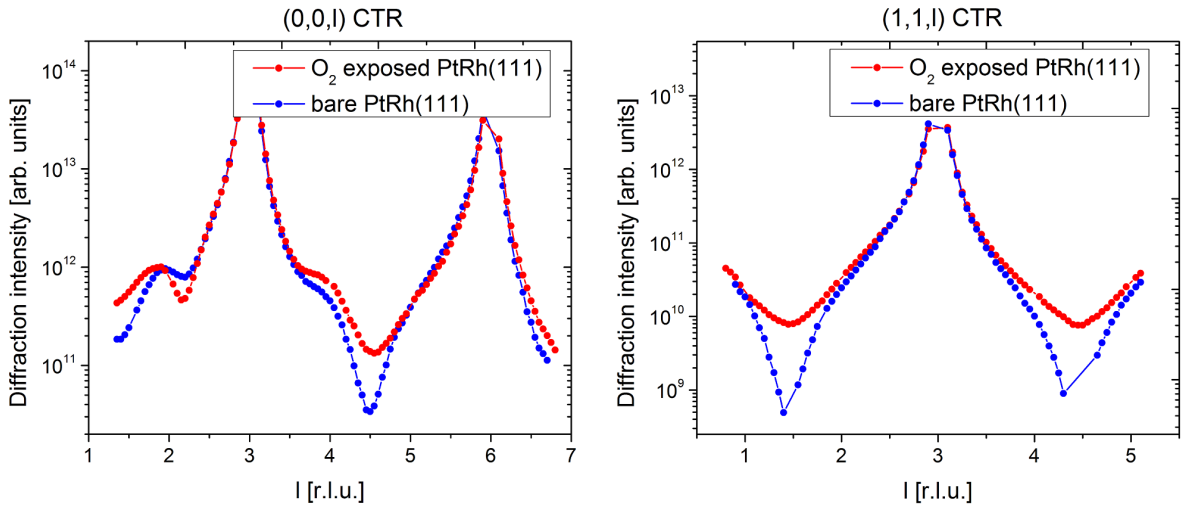

Figure 4.6: Crystal truncation rod data recorded on oxygen-exposed bare PtRh(111) compared to that of the virgin sample.

interference features become less pronounced, which must be produced by a resegregation in the vertical direction towards Pt:Rh ratios closer to the bulk value of 50:50 in the near-surface region.

The temperature regime of the PtRh(111) crystal preparation strongly affects its near-surface Pt-Rh composition. For example, higher temperatures than 1000 K promote platinum atoms to segregate towards the surface compared to rhodium atoms, and as a consequence, the surface composition shifts towards an approximate ratio of 2:1 Pt:Rh [8]. Also, various studies have shown that PtRh alloy surfaces exhibit catalytic activities under oxidising and reducing conditions [10–12]. Exposing the PtRh(111) alloy to oxygen above 1000 K leads to Rh enrichment of the surface [12, 13]. Oxygen is more strongly bonded to Rh than to Pt, and a thermodynamic force drives oxygen-induced Rh segregation [14].

Further SXRD measurements were performed on a bare PtRh(111) substrate after controlled oxygen dosing — the sample was exposed to 18 L oxygen at a temperature of 1073 K. The recorded CTR data are shown in Figure 4.6, from which it can be immediately recognized that oxygen indeed does induce substantial structural changes, evident from the (00l) and (11l) CTRs.

4.3 Semi-quantitative fitting on PtRh(111)

Based on the SXRD measurements discussed in the previous section, the recorded CTR data have been further used to perform semi-quantitative fitting in order to estimate the Pt-Rh composition down to five substrate atomic layers. The complete quantitative structural study is unfeasable task in the scope of this work. The present SXRD dataset is not fully reliable taking into account the quality of the sample due to insufficient surface treatment procedure during the beamline operation. An application of the complementary spectroscopic techniques is essential to assure quality — intrinsic contamination-free surface composition of the sample before proceeding consecutive SXRD measurements.

To model this system the mixed PtRh-alloy fcc(111) slab with 5 atomic layers was build. The model incorporated ten structural parameters, namely, the Pt-Rh atomic site vertical shift from its bulk position and the Rh composition at this site for each layer, respectively. The Rh occupancy (i.e., composition) was allowed to vary so that the total occupancy was kept 1.0. The (00l) and (11l) CTR data were used to fit the model. For the parameters initial guess, the model was first optimized manually, and then the final fitting result was obtained by the program GenX [15]. Consecutive semi-quantitative fitting was performed for a bare PtRh(111), h-BN on PtRh(111) and oxygen exposed PtRh(111) samples.

The determined values of Rh composition are summarized in Figure 4.7. Our findings contradict previous statements — the models indicate that h-BN causes the Rh-concentration to become nearly zero in the topmost layer, while its average composition (solid green line) is close to 50 %. Oxygen exposure in fact slightly reduces the Rh-composition in the topmost layer compared to that found for the bare PtRh(111) but both are close to 1.0. The fitted CTRs are shown in Figure 4.8. Further evaluation and interpretation of the fitting results is not completely reliable. To conclude, it is important to reproduce these measurements in a more controlled manner, possibly in conjunction with complmementary spectroscopic techniques.

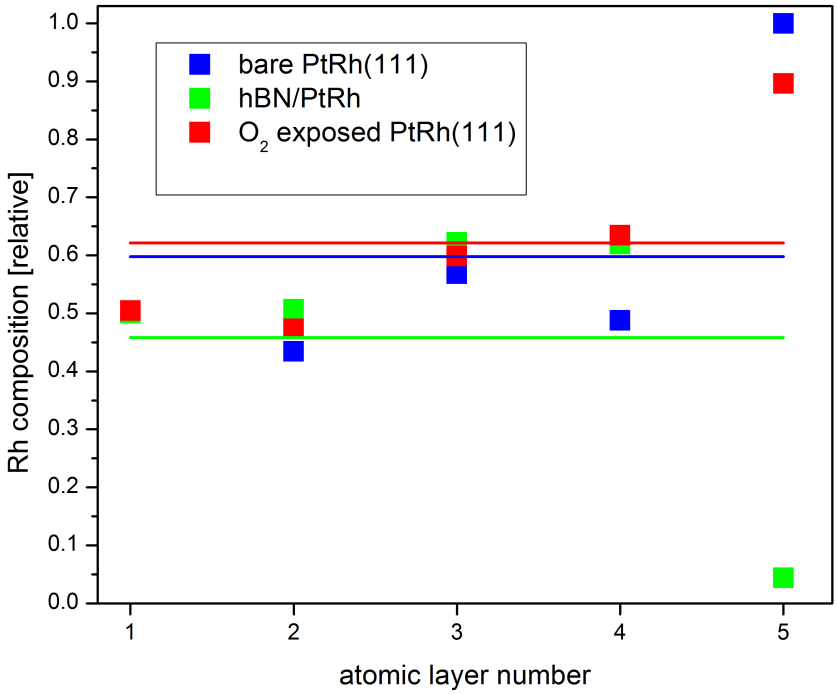

Figure 4.7: Summary of Rh-composition obtained from the fit. The color solid line shows the average Rh composition. The layer number 5 is the top layer.

4.4 Conclusions

In this chapter, results for the investigation of the *h*-BN nanomesh on PtRh(111) using SXRD have been presented. It was shown unambiguously that the reconstruction is in fact 11-on-10, not 12-on-11, which was reported in previous studies [8]. We recorded crystal truncation rods (CTRs) for the bare PtRh(111) and compared these to *h*-BN/PtRh(111). The CTRs recorded on bare PtRh(111) shows significant oscillations, highlighting electron density variation in the surface region. Comparing the CTR data, it is noticed that the *h*-BN nanomesh imposes further compositional changes in PtRh(111), in which the variation from the nominal 50:50 composition in the near-surface region is reduced, exhibited by a reduction in the oscillation amplitudes along the rods. We performed semi-quantitative structure fitting where the Rh-composition profile was obtained, but contradicted previous findings.

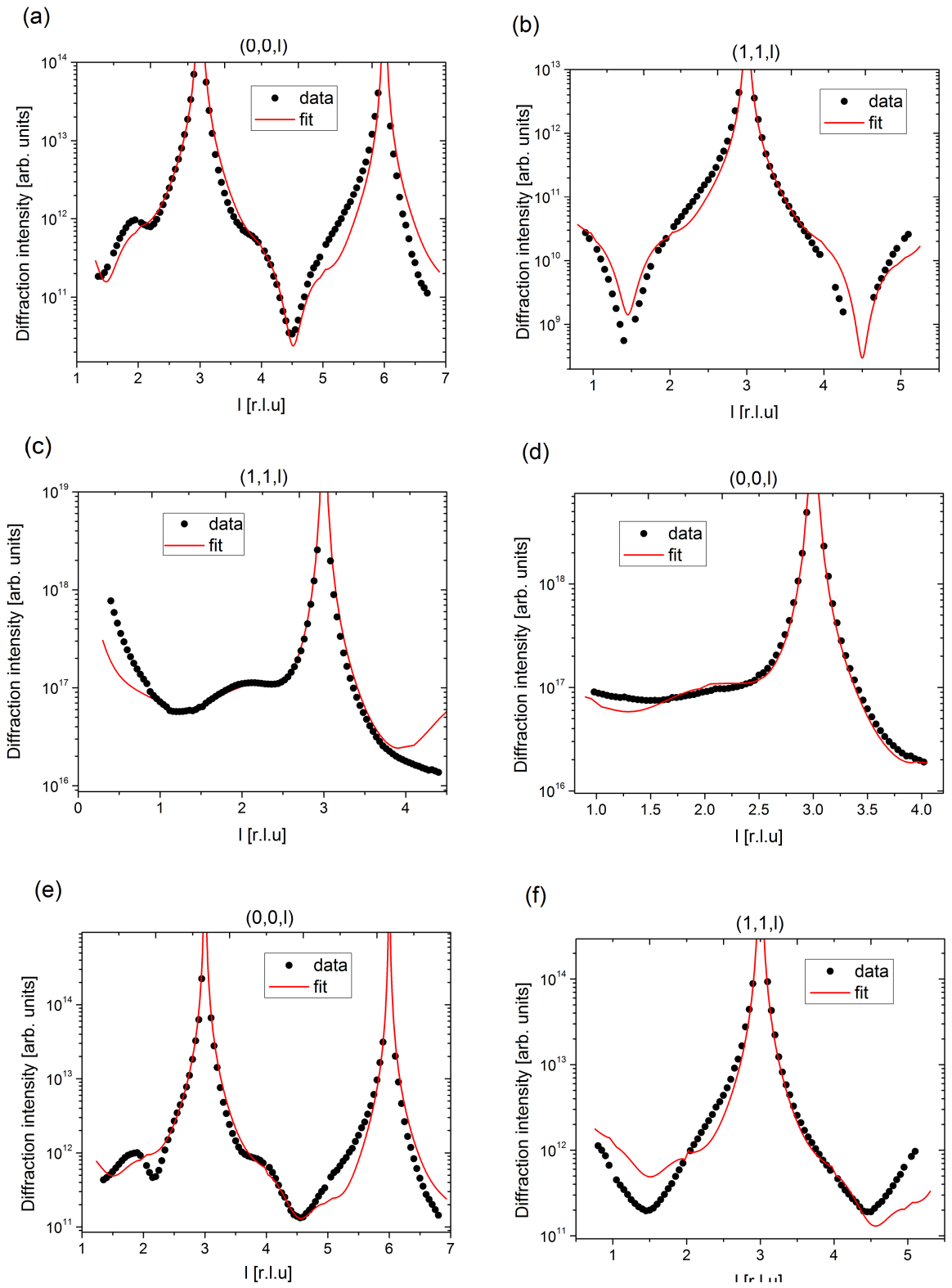

Figure 4.8: Fit of the crystal truncation rods. (a), (b) Bare PtRh(111) sample. (c), (d) *h*-BN on PtRh(111). (e), (f) Oxygen-exposed PtRh(111).

Bibliography

[1] M. Corso, W. Auwärter, M. Muntwiler, A. Tamai, T. Greber, and J. Osterwalder: "Boron nitride nanomesh." *Science* **303**(5655), 217–220 (2004).

[2] S. Berner, M. Corso, R. Widmer, O. Groening, R. Laskowski, P. Blaha, K. Schwarz, A. Goriachko, H. Over, S. Gsell, *et al.*: "Boron nitride nanomesh: Functionality from a corrugated monolayer." *Angewandte Chemie international edition* **46**(27), 5115–5119 (2007).

[3] A. Goriachko, Y. He, M. Knapp, H. Over, M. Corso, T. Brugger, S. Berner, J. Osterwalder, and T. Greber: "Self-assembly of a hexagonal boron nitride nanomesh on Ru (0001)." *Langmuir* **23**(6), 2928–2931 (2007).

[4] M. Morscher, M. Corso, T. Greber, and J. Osterwalder: "Formation of single layer h-BN on Pd (111)." *Surf. Sci.* **600**(16), 3280–3284 (2006).

[5] E. Platzgummer, M. Sporn, R. Koller, S. Forsthuber, M. Schmid, W. Hofer, and P. Varga: "Temperature-dependent segregation on $Pt_{25}Rh_{75}$(111) and (100)." *Surface science* **419**(2), 236–248 (1999).

[6] E. Platzgummer, M. Sporn, R. Koller, M. Schmid, W. Hofer, and P. Varga: "Temperature-dependent segregation and (1×2) missing-row reconstruction of $Pt_{25}Rh_{75}$(110)." *Surface science* **423**(1), 134–143 (1999).

[7] E. L. D. Hebenstreit, W. Hebenstreit, M. Schmid, and P. Varga: "$Pt_{25}Rh_{75}$(111),(110), and (100) studied by scanning tunnelling microscopy with chemical contrast." *Surf. Sci.* **441**(2), 441–453 (1999).

[8] R. Stania: *Lateral Segregation in h-BN/PtRh(111)*. Master's thesis, Universität Zürich, Zurich (2012).

[9] P. R. Willmott, D. Meister, S. J. Leake, M. Lange, A. Bergamaschi, M. Boge, M. Calvi, C. Cancellieri, N. Casati, A. Cervellino, *et al.*: "The Materials Science beamline upgrade at the Swiss Light Source." *J. Synch. Rad.* **20**(5), 667–682 (2013).

[10] T. Wang and L. D. Schmidt: "Surface enrichment of Pt-Rh alloy particles by oxidation-reduction cycling." *Journal of Catalysis* **71**(2), 411–422 (1981).

[11] T. Yamada, H. Hirano, K. Tanaka, J. Siera, and B. E. Nieuwenhuys: "Dynamic behavior of a $Pt_{0.25}Rh_{0.75}$(100) single crystal surface during NO+H_2 reaction." *Surface science* **226**(1), 1–14 (1990).

[12] Y. Matsumoto, Y. Aibara, K. Mukai, K. Moriwaki, Y. Okawa, B. E. Nieuwenhuys, and K. Tanaka:

"STM studies of oxygen-induced reconstruction on a Pt-Rh (100) alloy surface." *Surface science* **377**, 32–37 (1997).

[13] D. D. Beck, C. L. DiMaggio, and G. B. Fisher: "Surface enrichment of $Pt_{10}Rh_{90}(111)$: I. Annealing in vacuum and low pressure environments." *Surface science* **297**(3), 293–302 (1993).

[14] F. Esch, S. Günther, E. Schütz, A. Schaak, I. G. Kevrekidis, M. Marsi, M. Kiskinova, and R. Imbihl: "Chemical waves and adsorbate-induced segregation on a Pt (100) surface microstructured with a thin Rh/Pt film." *Surface science* **443**(3), 245–252 (1999).

[15] M. Bjorck and G. Andersson: "GenX: an extensible X-ray reflectivity refinement program utilizing differential evolution." *J. Appl. Crystallogr.* **40**(6), 1174–1178 (2007).

Chapter 5

Submonolayer Xenon on h-BN on Rh(111)

5.1 Introduction

Crystalline xenon physisorbed on solid surfaces is a frozen rare-gas in which interaction is mediated by weak van der Waals forces [1, 2]. The structure of xenon films physisorbed onto a graphite single crystal has been well studied using various diffraction techniques [3–7]. It was found that Xe atoms preferentially bind at the hollow sites on graphite (0001) surface and forms the $(\sqrt{3} \times \sqrt{3})R30^{\circ}$ commensurate structure.

This chapter addresses SXRD of hexagonal boron nitride (h-BN) nanomesh. A single layer of h-BN grown on Rh(111) forms a superstructure with a 3.2 nm lattice constant [8]. The h-BN nanomesh has a pore diameter of 2 nm and exhibits a long range, periodic modulation of the adsorption potential. Such an energy hypersurface allows trapping of atoms and molecules, and may provide template functionality for self-assembly [8–10].

The Xe adsorbed on h-BN on Rh(111) has been investigated by means of X-ray photoelectron spectroscopy (XPS) [10] and scanning tunnelling microscopy (STM) [11]. The XPS studies revealed that the binding energy for Xe adatoms on h-BN nanomesh surface is site specific. Moreover, it was found that the electrostatic potential gradient has a maximum at the rims of the holes and as consequence Xe-atoms are more strongly bound there. The local difference in the adsorption energy between wires and pores is of the order of 320 meV. The temperature-

dependent Xe-desorption STM studies showed that the Xe-atoms form clusters while desorbing from monolayer coverage [11] (see Figure 5.1). Above 62 K, the multilayer of Xe desorbs and a monolayer remains. At 85.5 K, the Xe monolayer is partially desorbed but Xe-atoms remain only at the rims of the *h*-BN nanomesh, where the adsorption energy is highest [Figure 5.1(a)]. The 12 Xe atoms located at the rim remain highly mobile (STM consequently shows a blurred image) and form a ring that has a mean diameter of 1.5(2) nm. The ring becomes static (the Xe-atoms are immobile) when the sample is cooled down to 5 K [Figure 5.1(b)]. As seen from the image, the Xe-coverage is not homogeneous and the rings are not present in every superstructure pore of *h*-BN. There are also randomly clustered Xe-atoms in some of the pores of the nanomesh.

SXRD can be applied to study real-time Xe-adsorption and desorption on *h*-BN. The results may provide valuable information about the degree of coverage and completeness of the Xe decorated structures. In order to elucidate the structure of the Xe rings on *h*-BN, a full structure fitting would have to be performed. The structural description of Xe on *h*-BN/Rh(111) is very complex. As pointed out before, the *h*-BN overlayer forms a superstructure which has a corrugated surface. The underlying Rh-substrate layers are also influenced by a commensurate *h*-BN overlayer and have a strained corrugated profile.

M. Iannuzzi *et al.* performed DFT calculation of *h*-BN on Rh(111). The DFT structure may serve as an *ansatz* for a starting model, and subsequent parameterization routine [Figure 5.1(c)]. The parameterization itself involves the fitting parameters for the atomic coordinates and varying them in a manner that keeps an intrinsic physical nature inherent in the DFT model. As previous activities have shown, parameterization of such a large superstructure is difficult and not necessarily representative of reality. Describing the structure of the Xe ring is straightforward because there are 12 atoms in a ring state. It means that essentially 32 fitting parameters (i.e., x, y, and z per Xe-atom) are needed in order to allow those 12 atoms to move on the surface. However certain constraints have to be imposed. The mean diameter of the Xe ring can only vary over a limited range and the Xe van der Waals radius must be taken into account. In order to find the true coordinates of the 12 Xe atoms, the full structure of Xe on *h*-BN/Rh(111) has to be fit. Although Xe has a stronger scattering contribution (Z=54) than Rh substrate (Z=45), it is impractical to obtain the true coordinates of the Xe atoms through a complete structure fitting. On the other hand, in the SXRD experiment, instability and high mobility of Xe adatoms may cause partial disorder across the surface. Xe-clusters were observed in local STM images, whereas SXRD will make an averaging over all Xe scat-

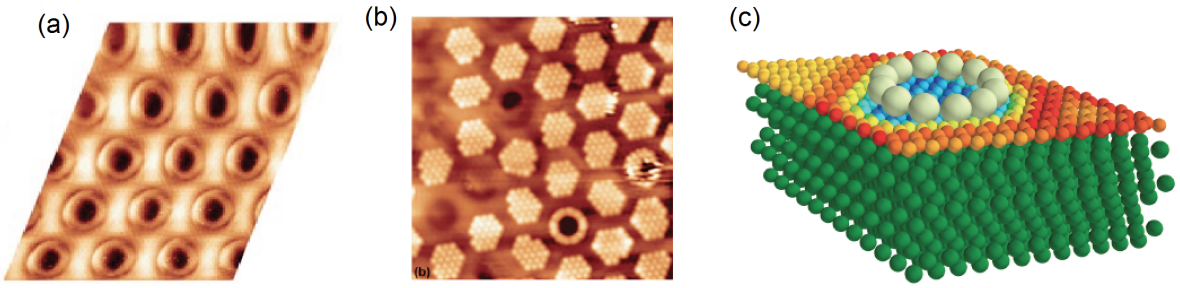

Figure 5.1: (a) Homogenous xenon "rings" on a nanomesh at T=85.5 K. The Xe atoms have high mobility but the highest residence probability at the pore rim (b) Sub-monolayer xenon on a nanomesh at T=5 K. A few static Xe rings in the pores, filled pores, and empty pores are observed. Adapted from [11] with permission from the Royal Society of Chemistry. (c) Visualization of Xe decorated nanomesh based on the DFT optimized structure on h-BN/Rh(111).

terers across the surface. Even at 5 K temperature, where Xe atoms are fairly immobile, the Xe-decorated nanomesh is irregularly covered.

5.2 SXRD study of Xe crystal growth on h-BN/Rh(111)

Despite all the systematic difficulties and potential problems described in the previous section, several SXRD experiments were performed at the MS beamline. The h-BN/Rh(111) samples were prepared in the ESCA lab at the University of Zürich. The samples were then transported to PSI under ambient conditions. The Be-dome-equipped cryostat was used. The sample was annealed to the maximum accessible temperature of 500 K (230 °C) for several hours in order to degas the surface after mounting in the cryochamber. The Xe-dosing system is a Xe filled reservoir (500 mbar) connected to the cryochamber (10^{-9}mbar) via a piezo leak valve for controllable dosing. SXRD measurements were performed using a beam energy of 10 keV (1.2398 Å). A surface coordinate system used was $a = b = a_{\text{bulk}}/\sqrt{2} = 2.689$ Å, and $c = a_{\text{bulk}} \cdot \sqrt{3} = 6.588$ Å. Here $a_{\text{bulk}} = 3.803$ Å is the bulk lattice constant of Rh. The orientation matrix was obtained from Bragg reflections of the Rh(111) substrate. Deposition of Xe films was carried at different temperatures and dosing pressures. The intensity of the $(h, k, l) = (0, 0, 1/4)$ point was monitored as a function of time during the Xe dosing [Figure 5.2 (a)].

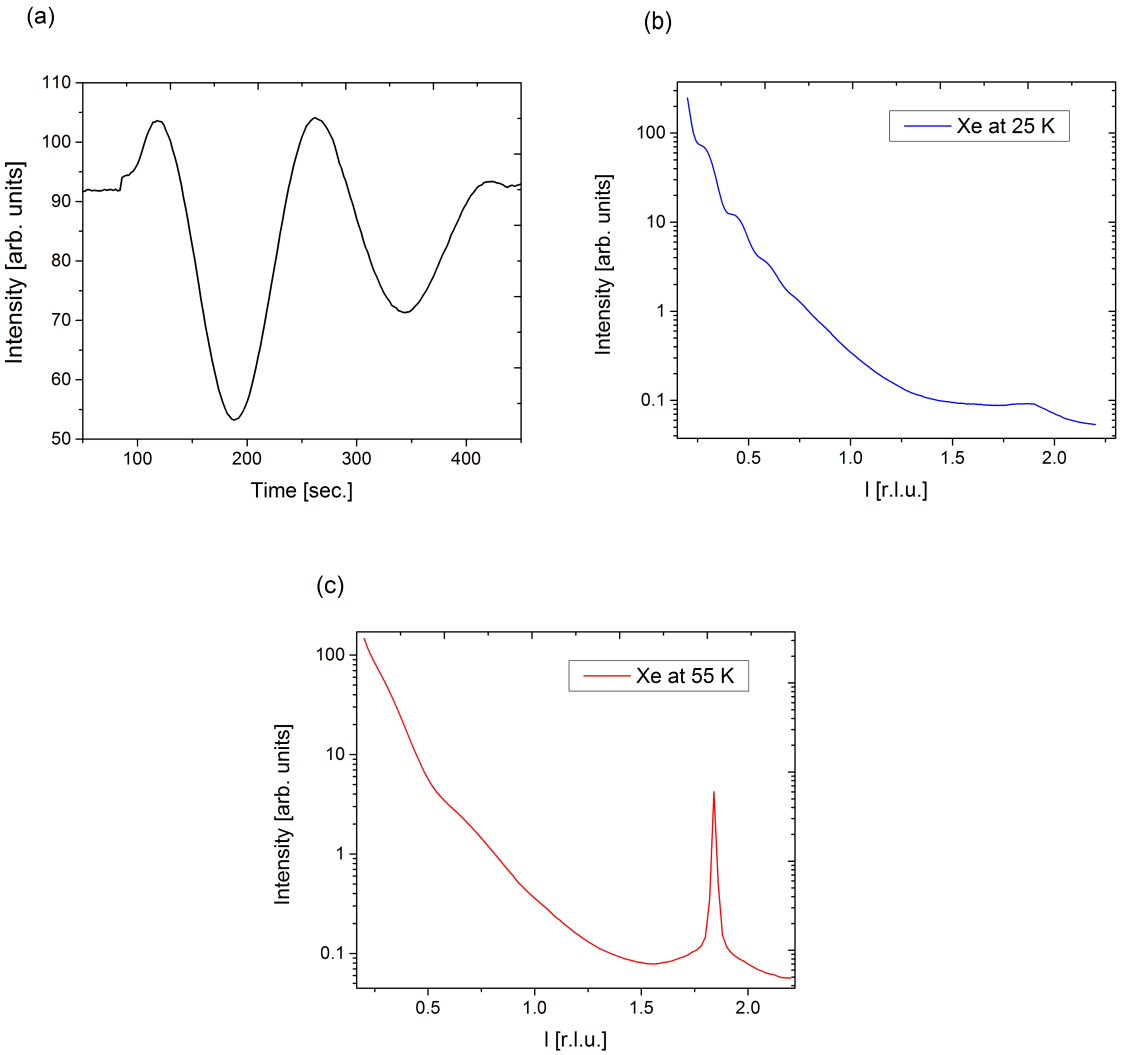

Figure 5.2: (a) Intensity of the $(0, 0, 1/4)$ point at the specular CTR as a function of time during Xe dosing at 2×10^{-6} mbar and at T=25 K. (b) Specular reflectivity scan (blue curve) showing well pronounced oscillations and a weak diffused Xe Bragg peak at l=1.84 r.l.u. The film thickness is estimated to be about 46.7 Å. (c) After warming up the sample to 55 K, the Xe Bragg signal becomes much stronger (red curve) due to an increased crystalline quality. Also the oscillation period is significantly increased indicating a decrease of the Xe layer thickness.

Subsequently, the reflectivity data was recorded and the film thickness determind as follow: $\Delta = \lambda/(2 \sin \theta)$, where λ is the X-ray wavelength and θ is an average oscillation period expressed

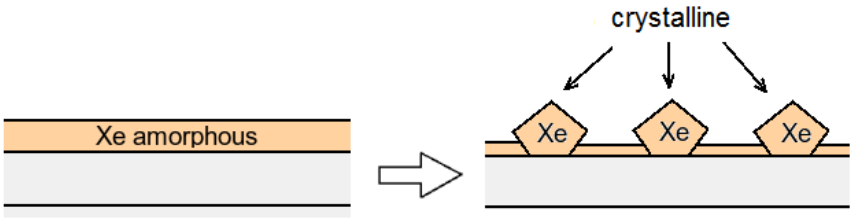

Figure 5.3: High quality xenon crystalline domains are formed after the annealing of the deposited semi-amorphous film.

in radians. The Xe deposition rate was found to be small and is explained as a consequence of a low sticking probability of Xe atoms. We found that Xe forms a hexagonal close-packed structure, the observed Xe Bragg peak position (θ =10.0 °, l=1.84 r.l.u.) corresponds to a d-spacing of 2×3.57 Å and indicates an $ABAB$ layer stacking. Interestingly, the Xe Bragg peak intensity increases significantly when the sample is warmed up to T=55 K and remains after cooling down to 25 K. However the film thickness decreases drastically as indicated in the reflectivity curve in Figure 5.2 [b]. This is explained as consequence of the annealing of the deposited semi-amorphous Xe film, which results high quality crystalline domain produced via *Ostwald ripening* (see Figure 5.3).

After multilayer Xe deposition, in-situ Xe desorption experiments were performed, where the two superstructure rods, (13/12, 0, l) and (11/12, 0, l) were recorded successively as the temperature was gradually increased (see Figure 5.4). As seen from data, there was no observed structural change, which is attributed to an absence of long-range order in the Xe overlayer in sub-monolayer coverage.

In order to elucidate the effect of the Xe ring on SXRD data, we made simulations. The model was based on DFT optimized structure of h-BN on Rh(111) system (see Figure 5.1[c]). The Xe ring was geometrically constructed taking into account known average ring diameter from the STM data and the van der Waal radius of Xe atoms. Figure 5.5 shows simulated (13/12, 0, l) and (11/12, 0, l) rods on bare and Xe decorated h-BN/Rh(111).

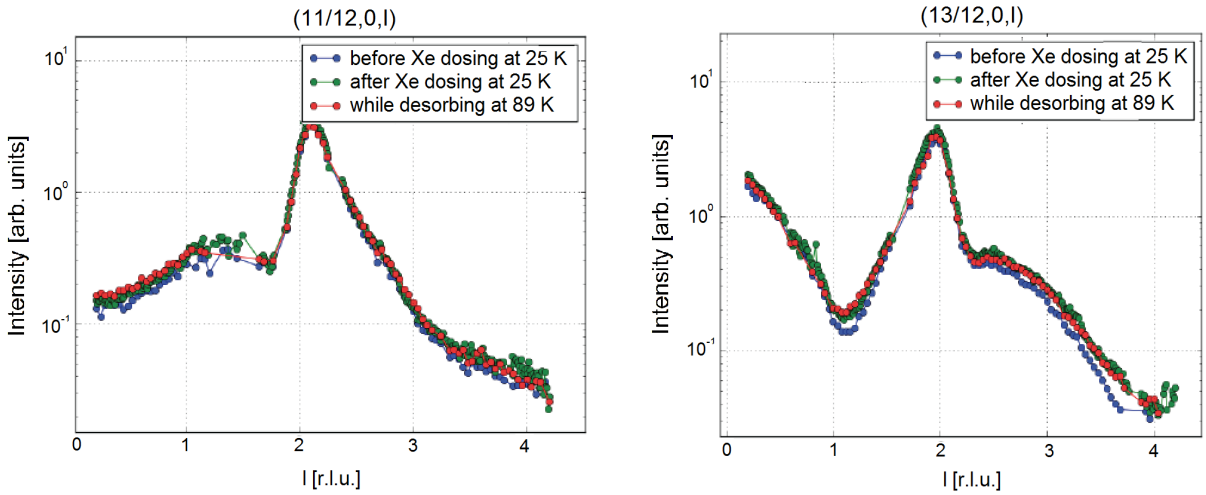

Figure 5.4: Two superstructure rods (13/12, 0, l) and (11/12, 0, l) recorded before Xe dosing and after Xe dosing at different temperatures.

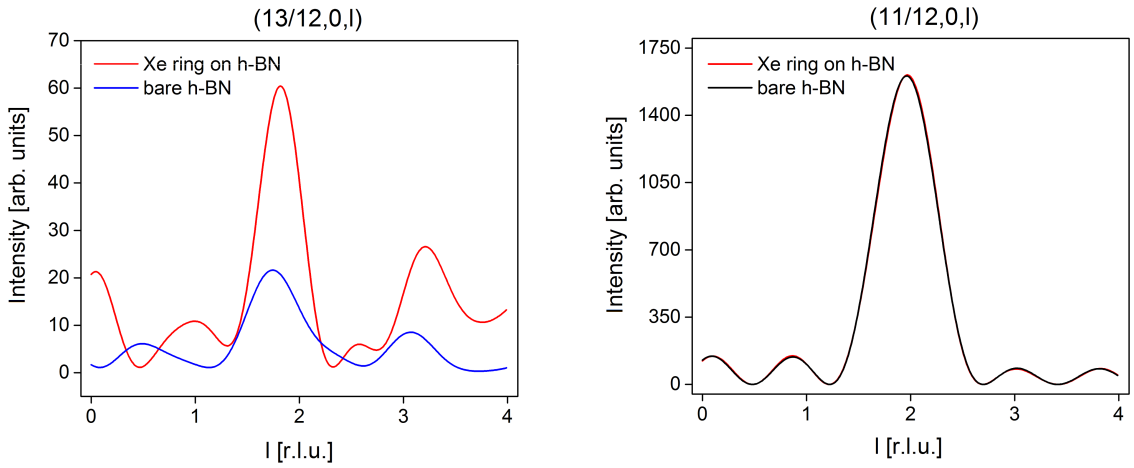

Figure 5.5: Simulated (13/12, 0, l) and (11/12, 0, l) SSRs. The model based on the DFT structure of h-BN on Rh(111). The Xe ring with the diameter of 1.4 nm was placed on h-BN according to the STM data. As seen, the (11/12,0,l) SSR is insensitive to the xenon ring structure.

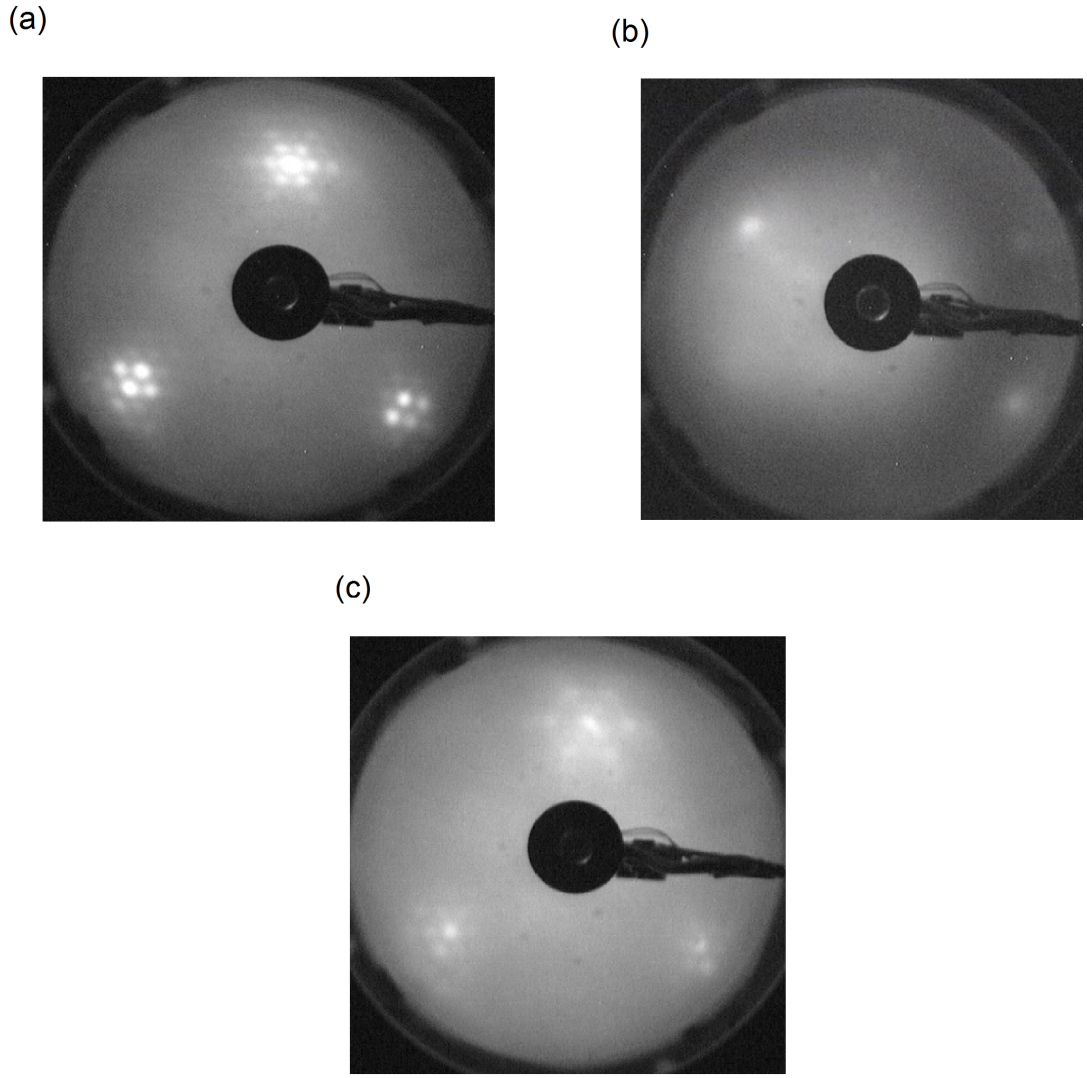

Figure 5.6: LEED image sequence on xenon on h-BN nanomesh. (a) h-BN sample before Xenon deposition. (b) Multilayer xenon on h-BN. The reconstruction spots are no longer visible but there is a signal which corresponds to the $(\sqrt{3} \times \sqrt{3})R30^{\circ}$ structure. (c) h-BN sample after Xenon complete desorption.

5.3 LEED measurements of crystalline Xe on h-BN/Rh(111)

In addition to SXRD measurements, we performed qualitative low-energy electron diffraction (LEED) experiment at the PEARL beamline, SLS. The LEED-images were taken at an energy of 41.1 eV and 10° tilt to observe both (0,0) and (1,1) spots. The LEED-image on clean *h*-BN/Rh(111) shows the Rh Bragg-spot and the superstructure satellite spots around it. After xenon dosing at T=25 K, these spots nearly vanish but a new signal manifesting the $(\sqrt{3} \times \sqrt{3})R30^{\circ}$ structure of xenon is visible. After increasing the temperature above 60 K, there is a sudden change where the Xe spot becomes significantly diffuse because of Xe multilayer desorption. Figure 5.7 shows an illustration of xenon on *h*-BN in which xenon adatoms are situated at the hollow sites on *h*-BN. This configuration corresponds to a $(\sqrt{3} \times \sqrt{3})R30^{\circ}$ structure.

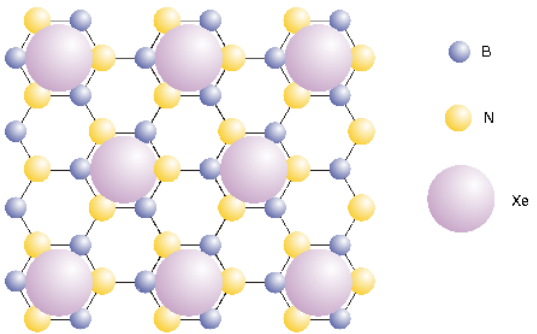

Figure 5.7: An illustration of xenon atoms situated on *h*-BN nanomesh.

5.4 Conclusions

In this project we have demonstrated growth of Xe films on *h*-BN/Rh(111). From the position of the Bragg peak we deduced that the Xe forms a hexagonal close-packed structure with an $ABAB$ layer stacking. From the LEED we also observed the Xe lattice spot after multilayer deposition. In SXRD experiments, two superstructure rods recorded at different temperatures showed no change with Xe-coverage, indicating that the degree of order of the Xe-overlayer was insufficient to be detected by SXRD. Taking into account the instability and high mobility of xenon atoms, and the lack of long-range order in the sub-monolayer regime, we concluded

that this system is not suitable for X-ray diffraction studies, at least, using the presently best available sample-preparation conditions. Also solving the structure of 12 Xe atoms of rings is a formidable problem because of a vast number of atoms constituting the *h*-BN/Rh superstructure.

Bibliography

[1] L. W. Bruch, M. W. Cole, and E. Zaremba: *Physical adsorption: forces and phenomena*, volume 6. Clarendon Press Oxford (1997).

[2] G. Vidali, G. Ihm, H.-Y. Kim, and M. W. Cole: "Potentials of physical adsorption." *Surface Science Reports* **12**(4), 135–181 (1991).

[3] H. Hong and R. J. Birgeneau: "X-ray diffraction study of the structure of xenon multilayers on single crystal graphite." *Zeitschrift für Physik B Condensed Matter* **77**(3), 413–419 (1989).

[4] J. A. Venables and P. S. Schabes-Retchkiman: "Adsorbed solid xenon and krypton on graphite-diffraction studies and model calculations." *Le Journal de Physique Colloques* **38**(C4), C4–105 (1977).

[5] T. Ceva, M. Goldmann, and C. Marti: "X-ray diffraction of krypton and xenon mixtures adsorbed on graphite." *Journal de physique* **47**(9), 1527–1532 (1986).

[6] R. K. Heilmann and R. M. Suter: "In situ specular and diffuse x-ray reflectivity study of growth dynamics in quench-condensed xenon films." *Physical Review B* **59**(4), 3075 (1999).

[7] K. Pussi, J. Smerdon, N. Ferralis, M. Lindroos, R. McGrath, and R. Diehl: "Dynamical low-energy electron diffraction study of graphite (0001)-($\sqrt{3} \times \sqrt{3}$)R30-Xe." *Surface science* **548**(1), 157–162 (2004).

[8] M. Corso, W. Auwärter, M. Muntwiler, A. Tamai, T. Greber, and J. Osterwalder: "Boron nitride nanomesh." *Science* **303**(5655), 217–220 (2004).

[9] S. Berner, M. Corso, R. Widmer, O. Groening, R. Laskowski, P. Blaha, K. Schwarz, A. Goriachko, H. Over, S. Gsell, *et al.*: "Boron nitride nanomesh: Functionality from a corrugated monolayer." *Angewandte Chemie international edition* **46**(27), 5115–5119 (2007).

[10] H. Dil, J. Lobo-Checa, R. Laskowski, P. Blaha, S. Berner, J. Osterwalder, and T. Greber: "Surface trapping of atoms and molecules with dipole rings." *Science* **319**(5871), 1824–1826 (2008).

[11] R. Widmer, D. Passerone, T. Mattle, H. Sachdev, and O. Gröning: "Probing the selectivity of a nanostructured surface by xenon adsorption." *Nanoscale* **2**(4), 502–508 (2010).

Chapter 6

Conclusions

In this thesis, surface X-ray diffraction structural studies of graphene and *h*-BN grown on rhodium and platinum-rhodium alloy have been described. In conjunction with density functional theory calculations (DFT), graphene on ruthenium has been elucidated in detail and the relevant structural parameters have been refined. Using also complementary methods, *h*-BN on PtRh alloy has been studied, in which compositional changes near the surface region were determined.

Graphene on Ru(0001) forms a corrugated superstructure. The reconstruction is found to be surprisingly large: (25×25)C on (23×23)Rh. Investigations are detailed in Chapter 3. SXRD simulations based on the DFT model of graphene on Ru(0001) were performed and compared to the experimental data. The simulated superstructure rods are fairly consistent with experiment, whereby the model has a goodness of fit (R-factor) of 12.6 %, better than that of previous model proposed by Martoccia (R-factor 14.3 %). STM studies on the graphene/Ru(0001) supercell revealed two distinct hill species in the corrugation. The same differently coordinated hills were observed in the DFT optimized model. The physical validity of the DFT model was evaluated using a structural parameterization by fitting the model to the SXRD data. Fitting was performed by the genetic-algorithm optimization program GenX. The best fit obtained has an R-factor of 12.2 %. The graphene peak-to-peak corrugation amplitude is 1.24 Å. The average C-Ru vertical distance is 2.282 Å. A two-dimensional R-factor map is produced in order to understand the sensitivity and robustness of the fitting parameters to the SXRD data. An acceptable range for parameters that are consistent with the SXRD data was estimated by the R-factor confidence interval set to 5 % of its lowest value. Based on the landscape of the R-

factor map, it was concluded that the R-factor of the DFT model lies in the confidence interval. Tests of changes in the R-factor with the parameters acting only on either the graphene layer corrugation or on the ruthenium substrate corrugation demonstrated that the SXRD data is relatively insensitive to the graphene structure, and is dominant by variations in the corrugation of the Ru-substrate.

In Chapter 4, the investigation of the *h*-BN nanomesh on PtRh(111) using SXRD is reported. From high- resolution, in-plane scans, an 11-on-10 reconstruction is determined. The superstructure size was precisely measured and found to be 27.29 Å. It is important to note that previous reports based on STM and LEED studies regarding the reconstruction were not correct. The influence of the *h*-BN nanomesh on the near-surface structure of the PtRh(111) was investigated. Crystal truncation rod (CTR) data from a bare PtRh(111) substrate and *h*-BN/PtRh(111) were recorded and compared. The CTRs of the bare PtRh(111) showed pronounced characteristic oscillations and strong interference fringe-like features, indicative of significant electron-density variation in the out-of-plane direction (i.e., vertical segregation) with respect to bulk down to approximately four atomic layers. On the other hand, the CTR data recorded on *h*-BN/PtRh(111) showed that the rod intensity variation is suppressed and the interference features become less pronounced. The *h*-BN nanomesh imposes a resegregation in the vertical direction towards the nominal PtRh 50:50 composition in the near-suface region. In addition, semi-quantitative structure fitting was performed and the Rh-composition profile was obtained.

Lastly, in Chapter 5, crystalline xenon physisorbed on *h*-BN/Rh(111) was studied using SXRD and LEED. The xenon films were deposited at different temperatures and dosing pressures. The deposition process was monitored by recording the intensity of the $(h, k, l) = (0, 0, 1/4)$ point as a function of time during the Xe dosing. The film thickness was estimated from the reflectivity data. It was found that xenon forms a hexagonal close-packed structure and follows an $ABAB$ layer stacking. A strong enhancement of the Xe Bragg peak was observed when the sample was warmed up to $T = 55$ K. On the other hand, the film thickness determined by the Kissig-fringe periodicity was decreased drastically. The latter was explained as consequence of the annealing of the deposited semi-amorphous xenon film, which results in high-quality crystalline domains produced via Ostwald ripening. In further SXRD experiments after multilayer Xe deposition, in-situ xenon desorption experiments were performed, where the two superstructure rods were recorded successively as the temperature was gradually increased. The recorded data showed no change with Xe-coverage, indicating an absence of long-range

order in the xenon overlayer. From the LEED studies, the $(\sqrt{3} \times \sqrt{3})R30^{o}$ structure of xenon was observed.

Publication List

Peer-reviewed articles

[1] V. V. Talanov, C. D. Barga, W. Lee, I. Kalichava, G. Edward, E. A. Shaner, A. V. Gin, and N. G. Kalugin: "Few-layer graphene characterization by near-field scanning microwave microscopy." *ACS nano* **4**(7), 3831–3838 (2010).

[2] N. G. Kalugin, I. Kalichava, J. Fallt, C. D. Barga, C. Cooper, J. G. Duque, G. Edward, S. K. Doorn, E. A. Shaner, and A. V. Gin: "The characterization of non-planar graphene nanowires with an Ω shape cross-section." *Carbon* **48**(12), 3405–3411 (2010).

[3] S. J. Leake, M. L. Reinle-Schmitt, I. Kalichava, S. A. Pauli, and P. R. Willmott: "Cluster method for analysing surface X-ray diffraction data sets using area detectors." *Journal of Applied Crystallography* **47**(1), 207–214 (2014).

[4] M. Iannuzzi, I. Kalichava, H. Ma, S. J. Leake, H. Zhou, G. Li, Y. Zhang, O. Bunk, H. Gao, J. Hutter, *et al.*: "Moiré beatings in graphene on Ru (0001)." *Phys. Rev. B* **88**(12), 125433 (2013).

[5] P. R. Willmott, D. Meister, S. J. Leake, M. Lange, A. Bergamaschi, M. Boge, M. Calvi, C. Cancellieri, N. Casati, A. Cervellino, *et al.*: "The Materials Science beamline upgrade at the Swiss Light Source." *J. Synch. Rad.* **20**(5), 667–682 (2013).